Gaps and Overlaps in Automated Fiber Placement Composites

Causes, Prediction and Process Design

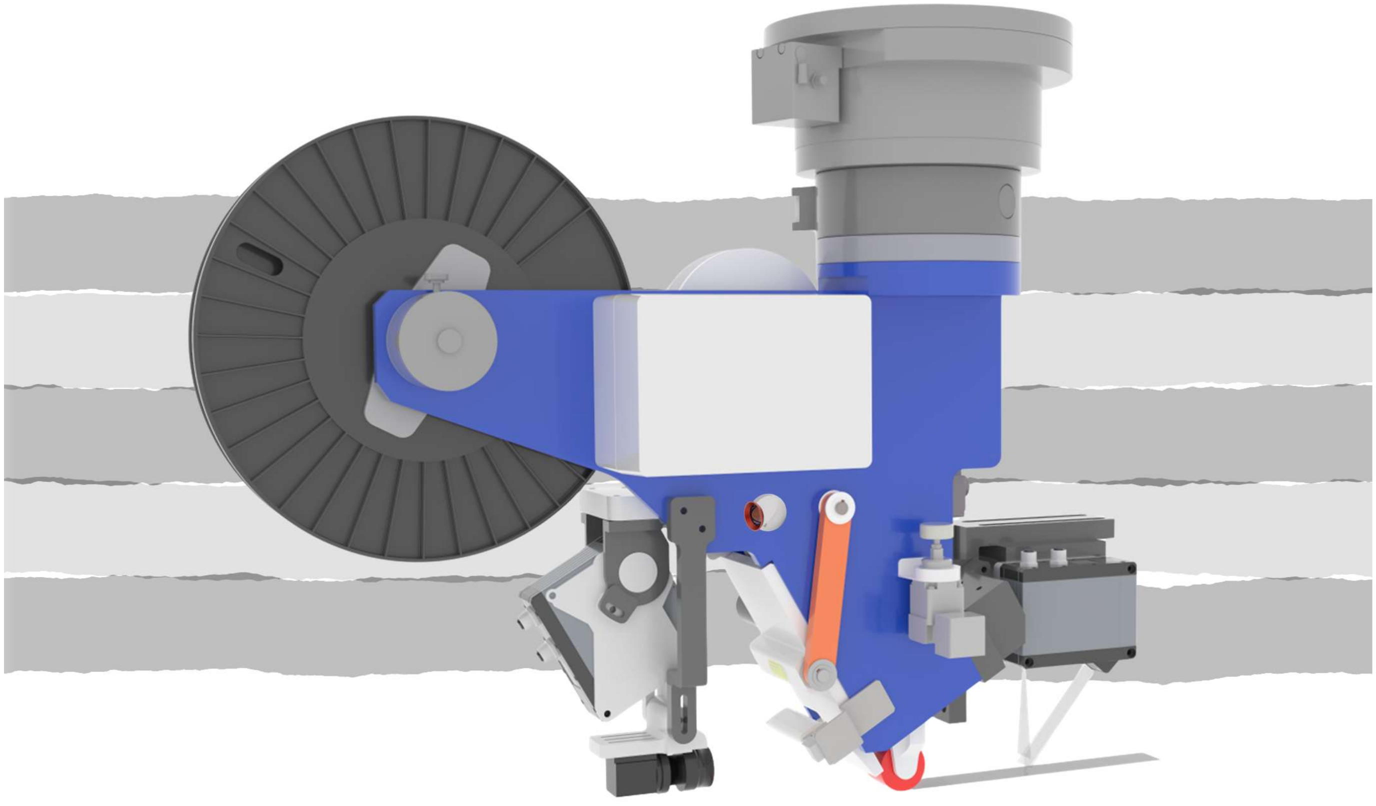

Siddharth Pantoji

Gaps and Overlaps in Automated Fiber Placement Composites

Causes, Prediction and Process Design

Gaps and Overlaps in Automated Fiber Placement Composites

Causes, Prediction and Process Design

Dissertation

for the purpose of obtaining the degree of doctor
at the Delft University of Technology
by the authority of the Rector Magnificus
Prof. dr. ir H. Bijl, Chair of the Board for Doctorates
to be defended publicly on
Thursday, the 11th of June 2026 at 12:30 hours

by

Siddharth Anil PANTOJI

This dissertation has been approved by the promotors.

Composition of the doctoral committee :

Rector Magnificus
Chairperson

Prof. dr. C. Kassapoglou
Delft University of Technology, Promotor

Dr. ir. D.M.J. Peeters
Delft University of Technology, Copromotor

Independent members :

Prof. dr. ir. K.M.B. Jansen
Professor, Delft University of Technology

Prof. dr. R. Harik
Director, Clemson Composites Center
Exxon Mobil Employees Endowed Professor, Clemson University

Prof. dr. R. O'Higgins
Head, School of Engineering
Professor, University of Limerick

Dr. ir. W.J.B. Grouve
Senior Research Associate, Thermoplastic Composites Research Center
Associate Professor, University of Twente

Dr. W. Seneviratne
Director, Advanced Technologies Lab for Aerospace Systems (ATLAS)
National Institute for Aviation Research, Wichita State University

Prof. dr. ir. R. Benedictus
Professor, Delft University of Technology, Reserve member

Keywords : Automated fiber placement, gaps and overlaps, manufacturing process variations, statistical modeling, steering, process design.

Cover : Created by Daniel Atherstone & Siddharth Pantoji.

 | ISBN 978-94-6518-340-4
A digital copy of this dissertation is available at the TU Delft Repository.

Dedicated to

Sant Dnyaneshwar

For envisioning a peaceful
and harmonious world

&

Dr. A. P. J. Abdul Kalam

For giving us the means to self-defense
should peace not hold

Summary

Manufacturing variations in the automated fiber placement (AFP) process are one of the causes of gaps and overlaps. These manufacturing variations can be due to robot inaccuracy, tow lateral movement on the roller, tow width variation or tow compaction. An experimental setup was built to measure and investigate these various sources of manufacturing variations and their relative contributions to gap and overlap defects. This setup consisted of a commercial AFP head instrumented with additional sensors. Among all the measured sources of variations, lateral movement of the tow on the compaction roller was the biggest contributor to gaps and overlaps. The distributions of these sources of variations were fit with probability density functions. Random samples from these fits were used to simulate adjacent tows and predict the occurrence of gap and overlap defects. The distribution of predicted gaps correlated closely with the distribution of experimentally measured gaps. Thus, this approach of using statistical information about the sources of manufacturing variations to predict the frequency and magnitude of defects in a layup was validated.

Gap and overlap defects are formed during automated fiber placement (AFP) layup due to stochastic variations in tow position and geometry from the aforementioned sources. There is utility in predicting the size and frequency of these defects since they affect the manufacturing rate and structural performance. Two methods which reflect the measured process variability were implemented to simulate realistic tow geometry. A Monte Carlo (MC) simulation used independent random sampling from the distributions of the sources of variation. A Markov Chain Monte Carlo (MCMC) simulation used the Random Walk Metropolis algorithm which samples these distributions while considering the neighborhood of past samples thus preserving spatial continuity. Simulated tows were assembled into virtual laminae. Tow-level validation using spatial-frequency Fast Fourier Transform (FFT) analysis demonstrated that the MCMC method reproduces the dominant wavelengths and spectral characteristics of experimentally measured tow waviness, whereas the MC method introduces unrealistic high frequency variations. Lamina-level comparisons showed that while both methods predict similar gap and overlap area percentages, only the MCMC method accurately captures defect length distributions. The proposed framework provides realistic virtual layup geometries suitable for use in the modeling of the mesoscale aspects of AFP layups. The framework is also useful in determining optimal process parameters for manufacturing process design

Position variations are twice as effective as geometry variations in creating gap and overlap defects. Tow lateral movement which is one of the causes of position variation was found to be a major contributor to gap and overlap defects during AFP layup in a straight line. In an experiment, to investigate this phenomenon under steering conditions, tow lateral movement was recorded during curvilinear AFP layup. This layup involved two different tow materials at steering radii varying from 1000 mm to 2000 mm. A shift of the tow in the radially outward direction of the curvilinear path was observed for both materials. The tows were observed to gradually shift to reach and stabilize at a position away from the roller center. The shift of the stabilized position was observed to become higher when the steering radius was reduced gradually from 2000 mm to 1000 mm. The rate of shift and the noise in the tow lateral movement differed for both materials. An analytical model was developed to predict and explain these tow lateral movement behaviors. A sensitivity analysis showed that the steering radius and the tow feed system chute geometry parameters had the most significant effect on the predicted tow shift magnitude while the coefficients of friction and compaction force parameters had the most significant effect on the predicted range of tow lateral movement. Further, the utility of the model predictions in offsetting the planned path to achieve layup trajectories with reduced gap and overlap defects was explained.

Samenvatting

Productievariaties in het geautomatiseerde vezelplaatsingsproces (AFP) zijn een van de oorzaken van openingen en overlappingen. Deze productievariaties kunnen te wijten zijn aan robotonnauwkeurigheid, laterale beweging van de tow op de rol, variatie in de tow-breedte of tow-verdichting. Er is een experimentele opstelling gebouwd om deze verschillende bronnen van productievariaties en hun relatieve bijdragen aan openingen en overlappingen te meten en te onderzoeken. Deze opstelling bestond uit een commerciële AFP-kop die was uitgerust met extra sensoren. Van alle gemeten bronnen van variaties was de laterale beweging van de tow op de verdichtingsrol de grootste bijdrage aan openingen en overlappingen. De verdelingen van deze bronnen van variaties werden aangepast met kansdichtheidsfuncties. Willekeurige steekproeven uit deze aanpassingen werden gebruikt om aangrenzende tows te simuleren en het optreden van openingen en overlappingen te voorspellen. De verdeling van voorspelde openingen correleerde nauw met de verdeling van experimenteel gemeten openingen. Deze aanpak van het gebruik van statistische informatie over de bronnen van productievariaties om de frequentie en omvang van defecten in een layup te voorspellen, werd dus gevalideerd.

Openingen en overlappingen ontstaan tijdens het geautomatiseerde vezelplaatsingsproces (AFP) als gevolg van stochastische variaties in de tow-positie en -geometrie van de bovengenoemde bronnen. Het is nuttig om de grootte en frequentie van deze defecten te voorspellen, aangezien ze de productiesnelheid en structurele prestaties beïnvloeden. Twee methoden die de gemeten procesvariabiliteit weerspiegelen, werden geïmplementeerd om realistische tow-geometrie te simuleren. Een Monte Carlo (MC)-simulatie gebruikte onafhankelijke willekeurige steekproeven uit de verdelingen van de bronnen van variatie. Een Markov Chain Monte Carlo (MCMC)-simulatie gebruikte het Random Walk Metropolis-algoritme, dat deze verdelingen bemonstert, rekening houdend met de omgeving van eerdere steekproeven, waardoor de ruimtelijke continuïteit behouden blijft. Gesimuleerde tows werden samengevoegd tot virtuele laminae. Tow-level validatie met behulp van ruimtelijk-frequentie Fast Fourier Transform (FFT)-analyse toonde aan dat de MCMC-methode de dominante golflengten en spectrale kenmerken van experimenteel gemeten tow-golving reproduceert, terwijl de MC-methode onrealistische hoogfrequente variaties introduceert. Vergelijkingen op lamina-niveau lieten zien dat, hoewel beide methoden vergelijkbare percentages openingen en overlappingen voorspellen, alleen de MCMC-methode de lengteverdelingen van defecten nauwkeurig vastlegt. Het voorgestelde raamwerk biedt realistische virtuele layup-geometrieën die geschikt zijn voor gebruik bij de modellering van de mesoschaalaspecten van AFP-layups. Het raamwerk is ook nuttig bij het bepalen van optimale procesparameters voor het ontwerp van het productieproces.

Positievariaties zijn twee keer zo effectief als geometrie-variaties bij het creëren van openingen en overlappingen. Laterale beweging van de tow, een van de oorzaken van positievariatie, bleek een belangrijke bijdrage te leveren aan openingen en overlappingen tijdens AFP-layup in een rechte lijn. In een experiment om dit fenomeen onder stuurbewegingen te onderzoeken, werd de laterale beweging van de tow geregistreerd tijdens een AFP-layup tijdens een krom-

lijnige layup. Deze layup omvatte twee verschillende tow-materialen bij stuurbewegingsradii variërend van 1000 mm tot 2000 mm. Er werd een verschuiving van de tow in de radiaal buitenwaartse richting van het kromlijnige pad waargenomen voor beide materialen. Er werd waargenomen dat de tows geleidelijk verschoven om een positie weg van het rolcentrum te bereiken en te stabiliseren. Er werd waargenomen dat de verschuiving van de gestabiliseerde positie hoger werd wanneer de stuurbewegingsradius geleidelijk werd verkleind van 2000 mm tot 1000 mm. De snelheid van verschuiving en de ruis in de laterale beweging van de tow verschilden voor beide materialen. Er werd een analytisch model ontwikkeld om deze laterale bewegingsgedragingen van de tow te voorspellen en te verklaren. Een gevoeligheidsanalyse toonde aan dat de stuurbewegingsradius en de geometrie van de tow-toevoersysteemgoot de belangrijkste invloed hadden op de grootte van de tow-verschuiving, terwijl de wrijvingscoëfficiënten en de verdichtingskracht de belangrijkste invloed hadden op het bereik van de laterale beweging van de tow. Verder werd het nut van de modelvoorspellingen bij het compenseren van het geplande pad om layup-trajecten met minder openingen en overlappingen te bereiken, uitgelegd.

Contents

1

Introduction

ॐ अथातो ब्रह्मजिज्ञासा ॥
— ब्रह्मसूत्र 1.1.1

Now begins the inquiry into fundamental principles.
— Brahma Sūtra 1.1.1

In this chapter, composite materials and their role in aerospace structures are introduced. It begins with a brief history of aircraft structures and the motivations for adopting composites. The relevant constituents of composite materials are outlined, followed by an overview of the Automated Fiber Placement (AFP) process. Then, the AFP market and its position within the aerospace manufacturing industry are discussed. Finally, the various aspects of defects in AFP composites are introduced. Note that the research objectives of this thesis are placed separately in the following chapter 2.

1.1. Structures and materials in the aerospace industry

The earliest gliders and aircraft had wooden structures covered with fabric. These were often braced by wire as tensioning elements for trusses. The wooden structures evolved with various types of wood and laminated construction to account for the anisotropy of wooden grains. As aircraft found their application in the military, they were getting designed to be larger, faster, more durable and manufacturable in large numbers. The quality and performance limitations of wood led to the development of metallic aerostructures. Initial designs started using corrugated Duralumin (Al–Cu alloy). This led to designs where the metallic wing skins shared the loads along with the spars and ribs inside the wing. Similarly, the fuselages also were designed such that the frames, stringers and the skins were all 'stressed'. Thus, these stressed-skin semi-monocoque metallic structures became the defining characteristic of aircraft structures as early as the 1930's and continued as the aerospace industry entered the jet age.

Weight savings in structures are strongly pursued by the aerospace industry. Reducing weight of an aircraft leads to fuel savings. Reduced structural weight also means more scope for carrying extra fuel for longer range missions or with heavier payloads. Also, the aircraft can be designed to perform with lower engine thrust, wing area, fuel capacity. The value of weight savings in structures varies in various aerospace applications. These applications are mentioned here in the ascending order of cost savings per kg in their aerostructures - small general aviation aircraft, helicopters, aircraft engines, fighters, commercial aircraft, supersonic airliners, satellites and launch systems [9].

Composite materials were gradually introduced into aerostructures starting in the 1960s. In the initial stages, aerospace companies built demonstration composite parts only to study the feasibility and the advantages of these materials. Later, composite parts which could replace existing metallic parts were flight tested. The industry then started designing and producing aircraft which had some secondary structures made of composites. The industry has since moved to an era where large primary structures are also made from composite materials. The adoption of composites has been led by military aircraft, however, relevant public domain data remains unavailable. Figure 1.1 shows the increasing weight of composites as a percentage of the aircraft weight over the years.

In general, composite materials and manufacturing is more expensive than traditional metallic materials and their manufacturing techniques. While pushing the boundaries of new composites for weight savings, due attention is given to the risks present in maturing these technologies in time for the new platform development schedules. Certification requirements from the regulators are stringent and lead to high certification costs. These costs cover the testing and analysis of the manufacturing methods and the resulting structural parts [10]. Thus, in general, it takes between 1-3 decades for new materials and manufacturing processes to be used on a certified airplane.

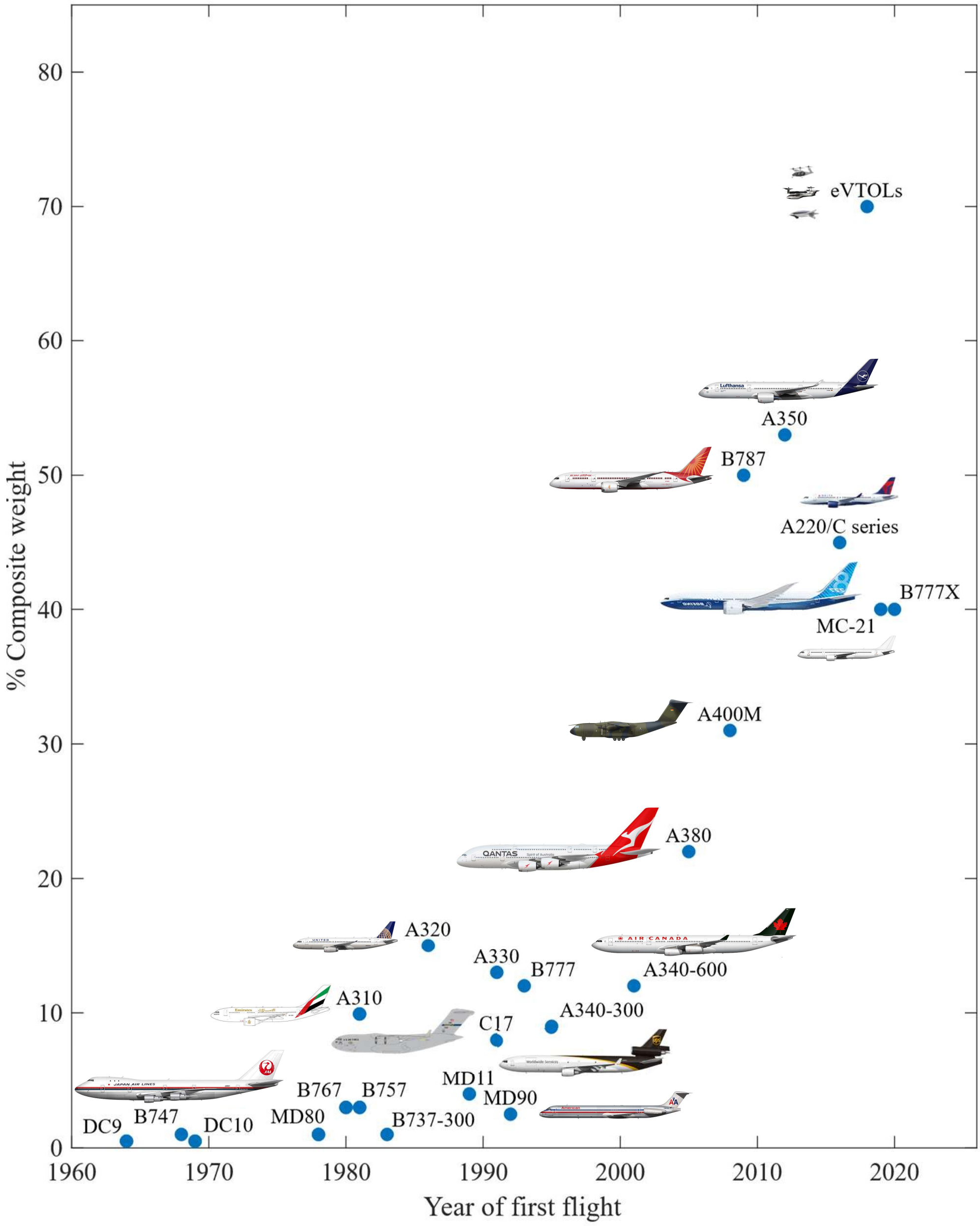

Figure 1.1: The percent weight of composites in aircraft has been rising through the years. The new single aisle aircraft which will fly in the coming decade are also expected to have majorly composite airframes. Note that some data points may be approximate. Copyright remains with the original image sources [1–8]

1.2. Composite materials

Composites material systems are made out of two or more constituents. These constituents are combined on the macroscopic scale such that they maintain their physical, mechanical and thermal properties. In contrast, alloys are made out of different metals but are distinct only at the microscopic scale. However, they are macroscopically homogenous for all purposes like mechanics. Composites are heterogeneous materials since the properties at different material points are different. Since all matter is heterogeneous at the atomic level, defining composite materials requires attention to scales. In composite materials, the reinforcing phase consists of particles and/or fibers. The reinforcing phase imparts stiffness and strength properties to a composite. The reinforcing phase is held and oriented together in a supporting phase called matrix phase. This matrix phase not only binds and protects the reinforcing phase but also transfers load to it. The matrix phase shares the load especially in directions perpendicular to the fibers.

Composites can be fiber reinforced composites (FRC's) or particle reinforced composites (PRC's). PRC's are cheaper, less stiff and weaker than FRC's. FRC's can further be classified into continuous fiber reinforced composites (CFRC's) or discontinuous fiber composites (DFRC's) depending on the length of fibers used. Composites can also be classified on the basis of the kind of matrix – polymer matrix composites (PMC's), metal matrix composites (MMC's), ceramic matrix composites (CMC's) [11].

Commonly used reinforcement fibers include glass, carbon, and aramid fibers, with typical diameters on the order of 5-20 μm. These fibers exhibit exceptional mechanical properties, which enable composites to achieve high specific stiffness and specific strength compared to metals. Table 1.1 compares typical properties of fibers used in composites with those of conventional metallic materials.

Composites enable more efficient structures because of advantageous specific stiffness and specific strength properties. Composites are anisotropic because they are stiffer and stronger in the direction of the fibers within. The microstructure of composites can be tailored by changing fiber and matrix constituents, fiber volume fraction and fiber orientation. Anisotropy in composites can be exploited by suitably aligning the directions of high stiffness and strength with the dominant stress directions, thereby improving structural efficiency.

Material	Density (g/cm^3)	Stiffness (GPa)	Strength (MPa)	CTE ($10^{-6}/°C$)
Steel	7.8	210	340 – 2100	12.8
Aluminum	2.7	70	140 – 620	23.4
E – glass fiber	2.54	77	3500	4.9 – 6
S – glass fiber	2.49	89	4590	2.9
Aramid	1.44	130	3600	– 2 to – 4
IM carbon fiber	1.78	294	5490	-0.6
HM carbon fiber	1.91	588	3820	-1.1

Table 1.1: Material properties comparison [11–16].

1.2.1. Carbon fiber

Continuous carbon fiber is the most used type of reinforcing phase in advanced aerospace composites. Carbon has various different allotropes having distinct properties derived from their molecular structures. One such allotrope is graphite. Graphite has hexagonally arranged carbon rings in a planar formation as seen in figure 1.2. Each carbon atom is covalently bonded to three other carbon atoms including angles of 120°. These strong bonds are within the plane formed by the hexagonal rings which can extend to form large molecules. The carbon atoms have an extra electron which allows for interplanar bonding in addition to the coplanar strong bonds. Thus the graphite layers are bonded through weak van der Waal forces [17].

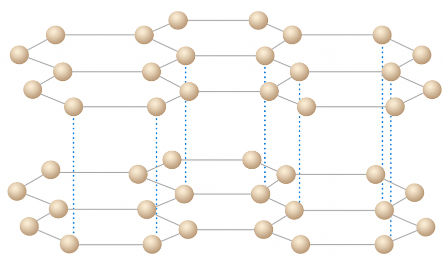

Figure 1.2: Graphite molecular structure schematic. The solid lines depict strong covalent bonds while the dotted lines represent weak van der Waals forces.

A graphite whisker is a single, flaw-free crystal of very high strength. But they cannot be made in commercially significant quantities. However, polycrystalline carbon fiber strands which contain networks of hexagonal networks with layers stacked on each other without crystallographic order can be made in large quantities. Thus, carbon fibers are thin long strands of such polycrystalline carbon material with diameters ranging from 5-10 µm. Carbon fibers are generally defined to have a carbon percentage of 92-100%. If the proportion of carbon in graphitized stage exceeds 99%, it is called a graphite fiber.

The carbon fiber properties vary depending on the fiber structural details and crystal orientations. The ultrahigh modulus (UHM) and high modulus (HM) carbon fibers are highly graphitized leading to high moduli. The UHM carbon fibers have a modulus greater than 500 GPa, while the HM carbon fibers have a modulus greater than 300 GPa. The intermediate modulus (IM) and high tensile strength (HT) carbon fibers have high strength and low modulus. The IM carbon fibers have a modulus of up to 300 GPa.

The strength to modulus ratio of these fibers signifies the strain to failure i.e. how much the fiber can stretch before it breaks. High strain to failure carbon fiber would imply that the fiber can take more strain. It would thus be suitable for applications where impact, vibration or fatigue are the major drivers. Lower strain to failure carbon fiber would correspond to a stiff fiber which breaks suddenly. These would be more suitable for applications needing high dimensional stability. UHM carbon fiber has a strength to modulus ratio of less than 0.5%. HM fiber has a strength to modulus ratio of less than 1%. IM carbon fiber has a strength to modulus ratio greater than 1%. While HT carbon fiber has a strength to modulus ratio of less than 1.5-2%.

The fibers used for manufacturing of composites start their life as untwisted set of fibers called 'tows' or 'rovings' wound on rolls. They are called 'yarns' if the tows have been twisted and wound. These fiber rolls can be used to weave the loosely held strands into cloth or fabrics. They can also be simply chopped up to use the fiber bundles as it is or binded by agents to form non-woven mats. Some fiber tows are available in 'tape' form of material which has fibers pre-impregnated with matrix material and are hence called prepregs. In this thesis, the words tow and tape have been used interchangeably.

All these aforementioned forms of fiber are used in a variety of composite manufacturing processes which can be classified on the basis of the following primary approaches.

1. Component geometry is filled with architectured fiber mass and later infused with matrix polymer to fill to near net shape
2. Fiber and matrix polymer are combined into preform which is developed into component geometry. Some methods of composite manufacturing are manual or automated layup followed by in-autoclave processes, spray-up (eg fiber glass – resin mixture sprayed on boat molds by pressurized nozzle), filament winding (mostly for cylindrical parts like rocket motors and pressure vessels), continuous pultrusion, transfer molding, injection molding, compression molding etc.

Composite manufacturing processes use fibers of different lengths. For example, filament winding process uses a continuous wetted tow wrapped around a cylinder for the manufacturing of pressure vessels. Layup for in-autoclave curing of laminates consists of unidirectional prepreg which can have a few meters of fiber length depending on the part size and practicality of handling big prepreg cut-outs. These would be considered as continuous fiber systems. As opposed to these in-autoclave processes, molding processes use short fibers with length ranging from a few hundred micron to a few centimeters. These would be considered discontinuous fiber systems. We can see that continuous fiber systems are used in manufacturing processes which take from a few hours to a few days. These processes are usually used in the aerospace industry where quality is important and cost, cycle speed is secondary. In contrast, discontinuous fiber systems are used in manufacturing processes employed in mass production environments such as the automotive industry. Thus, discontinuous fiber systems are easier to process whereas continuous fiber systems have lower processability due to more complex manufacturing steps. Also, performance is highest in continuous fiber systems and drops as fiber lengths become smaller.

1.2.2. Thermoplastics & thermosets

This section has been used to generally introduce polymer matrices. Section 1.3.2 will discuss the use of these in tows for the AFP process. Of interest in this review, composite materials will now refer to polymer matrix fiber reinforced composites. PMC's can also be classified based on the type of polymer – thermoplastics or thermosets, used as a matrix. Thermoplastic polymers consist of loosely coiled, string like long chains formed from covalently bonded monomers. These are illustrated in the schematic of figure 1.3 (left). The polymeric chains are linked by weak van der Waals forces. They do not need refrigeration and thus are easier to store. Thermoplastics are more viscous and therefore more difficult to flow and process. These polymers transform to solids by melt solidification. Examples of thermoplastics commonly used in aerospace composites include the family of Polyaryletherketones (PAEK) which include Polyetheretherketone (PEEK), Polyetherketoneketone (PEKK), Low melt Polyaryletherketone

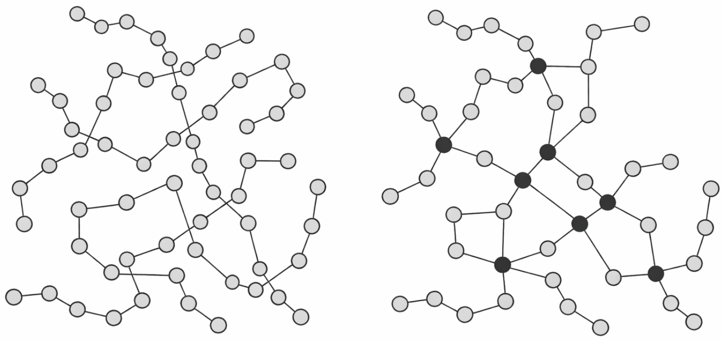

Figure 1.3: Schematic illustration of the loosely coiled long-chain molecular structure of thermoplastic polymers (left) and the cross-linked three-dimensional network structure of cured thermoset polymers (right).

(LM-PAEK™) as well as other high performance polymers such as Polyphenylene Sulfide (PPS), Polyetherimide (PEI) etc.

Thermosets are branched chain polymers linked by strong covalent bonds. They form a three dimensional network structure by polymerization. This networked structure is illustrated in the schematic of figure 1.3 (right). They are relatively hard and brittle. Once cured they cannot be remolded and hence are harder to recycle. The raw materials need storage under refrigeration to stop curing reaction and increase shelf life. Thermosets when heated are less viscous and therefore have better flow properties leading to easier processibility. These polymers transform to solids by chemical reaction. Examples of aerospace-grade thermosets include Epoxy (EP), Bismaleimides (BMI), Cyanate Esters (CE), Phenolic Resins (PF), and Polyimides. Thermosets have been used in the aerospace industry for a longer time than thermoplastics and therefore are more entrenched in the market.

1.3. Automated Fiber Placement

AFP is an additive manufacturing process for composite parts. It involves using robots to lay down a strip of composite material on a tool by making passes across it. These strips of fiber tows are laid next to each other to form a lamina. Many such laminae laid on top of each other result in a composite laminate. The AFP head is an end effector attached to an industrial robot. This head has compaction roller which rolls in contact with the tool or the substrate while applying pressure. As it rolls, a system of wheels, pulleys and chutes makes the composite tow available to the compaction roller. Tape and tow are used interchangeably to describe a composite material strip. The AFP head also has a heating system which helps with the bonding of the composite tow to the tool or the substrate. The AFP head also has a cutter which can cut the composite strip at the end of a pass. Figure 1.4 shows a schematic of the AFP process.

AFP machines can lay multiple composite strips at a time. These strips laid together in one pass are called a course. AFP machines typically have 1, 4, 8, 12, 16 tows in one course. It is important to know that during the layup all the tows can be pulled in by the roller at different rates. This enables the AFP machine to laydown tow with differing payout. This allows the

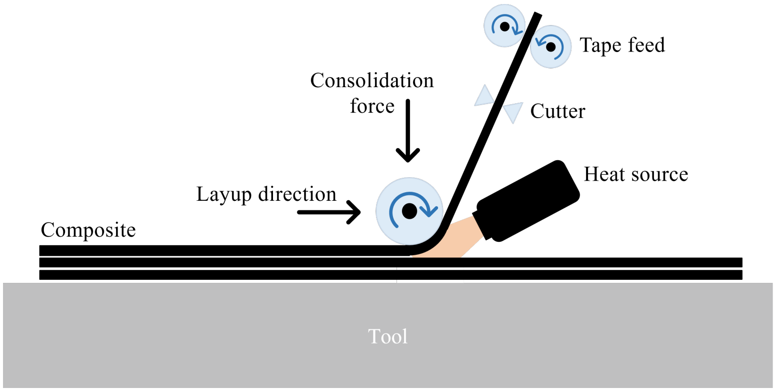

Figure 1.4: Schematic of the AFP process

AFP machine to lay on complex shapes. Another factor which affects the complexity of layup is the width on the tape. Narrower tape can conform to the tool shapes more easily than wider tapes. AFP machine typically use 1/8, 1/4, 1/2, 1 inch wide tows.

The Automated Tape Laying (ATL) process is similar to the AFP process but it uses wider tapes which are typically 3, 6, 12 inches in width. These can conform to lower curvatures and are therefore used for flat and slightly curved parts. ATL has higher deposition rates compared to AFP, but AFP can conform to more contoured surfaces. It should be noted that there is no hard scientific threshold to distinguish between AFP and ATL.

1.3.1. AFP machine types

There are two main types of robotic systems used in AFP cells - gantry systems and articulated robots. These robotic systems give the AFP head multiple degrees of freedom in moving around a tool. Gantry systems consist of a column and beam structure with linear axes. The overhead AFP head in gantry systems can access large workspaces depending on the length of the travel rails. This is advantageous for the layup of large parts. The AFP head has additional rotational degrees of freedom which allow for complex trajectories. The AFP head is designed to be compact. The AFP head dimensions and its kinematics together decide the abilities of the robotic cell to achieve layup on complex curved tools. Gantry systems can also allow for changing between AFP and ATL heads. Some gantry robots have only one linear axis on the floor. These can be paired with a tool on a rotating axis for creating parts with cylindrical layups. An additional advantage of such a system is the access of the tool from the other side. This can be utilized for operating robots which clean tools or inspect the layup. Figure 1.5 illustrates several commonly used configurations of AFP robotic systems.

AFP is getting democratized from being a specialist process requiring massive acquisition costs for the robotic cell and associated equipment to a more widely adopted and comparatively less expensive process which can use the more widely available multi-purpose articulated robots. These versatile robots are cheaper. Compared to gantry systems, they have relatively smaller workspaces but are able to layup more complex composite parts. They can also be combined with a horizontal or vertical rotating axis for cylindrical parts.

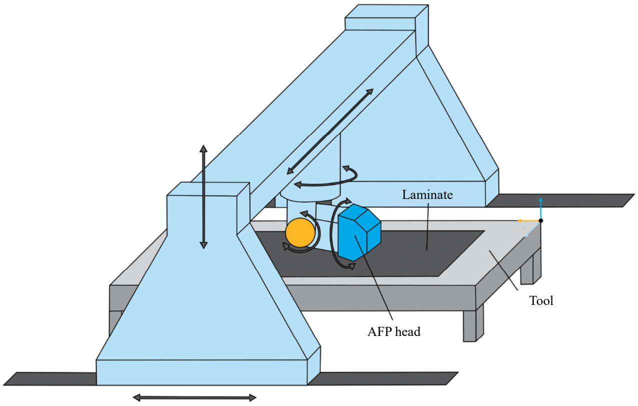

(a) Vertical gantry AFP machine.

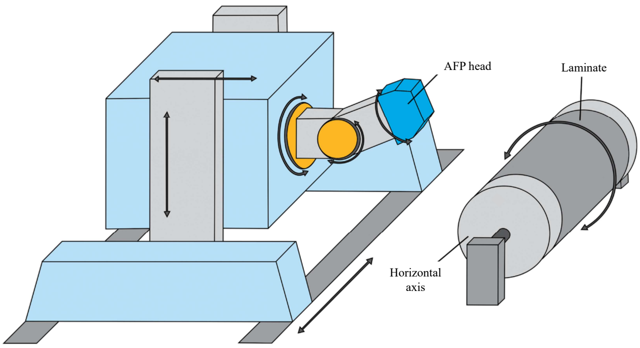

(b) Horizontal gantry AFP machine with a horizontal rotational axis.

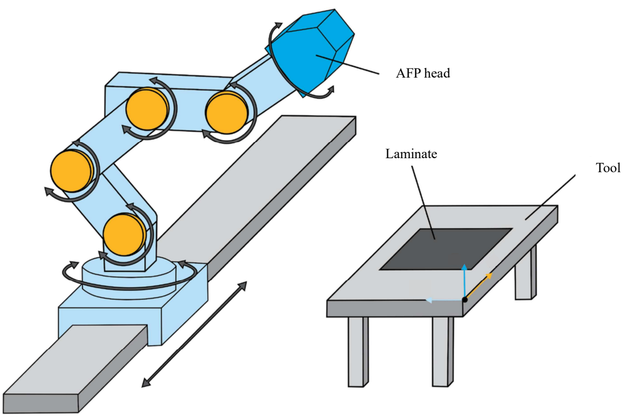

(c) Articulated AFP machine.

Figure 1.5: Examples of AFP machine architectures. Image source [18].

The tow supply systems also differ between various models of AFP machines. Some use spools mounted on the AFP head. This setup leads to a shorter and simpler delivery mechanism. But it also means that the size of the AFP head is bigger leading to less access in curved concave tools. Some AFP systems incorporate the capability to programmatically exchange AFP heads when material spools are depleted. In such production cells, dedicated AFP head load–unload or parking jigs are provided. An AFP head preloaded with new material spools can be staged in the jig and swapped with the active head to have minimal interruption of the layup.

An alternative is to have the spools located in a creel house. These supply material to the AFP head via a system of pulleys, chutes and guides. This makes the path of the materials from the spools to the compaction roller longer and complicated leading to possible issues with maintenance and cleaning. The refrigeration in the creel box is needed for thermoset material spools, whereas thermoplastics can simply be stored at room temperature with no special requirements for temperature or moisture control.

1.3.2. Tow materials and processing routes

The AFP layup process has a few different 'flavours' depending on which kind of tow materials are selected. This selection also decides the configuration of the AFP heater, feed system and the manufacturing steps after the AFP layup. The three major kinds of composite tow material which can be laid by AFP are thermoset prepreg tow, thermoplastic prepreg tow and dry fiber tow. Figure 1.6 shows the manufacturing steps possible with these major kinds of AFP tow materials. Various niche materials such as CMCs, hybrid tows are also used for specialist applications. Their post-processing involving infiltration and very high temperature fall outside the scope of this discussion.

Currently, all certified and flying AFP parts are manufactured using thermoset prepreg tow. This is also due to the long history of thermoset prepregs in composite manufacturing compared to other matrix materials. The heater on the AFP machine needs enough heat flux supplied to the tow that it simply bonds the material to the substrate by way of its tackiness. However, this is followed by an autoclave process. The laid part along with its tool is moved into an autoclave where it is subjected to an appropriate temperature and pressure cycle. The elevated temperatures in the autoclave cure the thermoset matrix materials while they are consolidating under pressure. This autoclave processing is expensive and energy intensive. Large AFP parts require giant autoclaves. Each manufacturing site usually has only one or a few autoclaves. Since it takes a few hours for each loading, curing and unloading cycle, it is considered to be a major bottleneck.

Removing the autoclave bottleneck would mean for large savings and higher production rates. Hence alternative manufacturing steps are being explored. These include using out-of-autoclave thermoset matrix chemistries. For thermoplastic materials, the consolidation may be done with the help of heated tools and alternative pressurizing techniques using special bagging setups or topside tooling blocks. However, the holy grail of AFP manufacturing is in-situ consolidated (ISC) manufacturing. Figure 1.6 shows how it requires no additional steps. It involves AFP layup of thermoplastic tows with a heater with much higher power ratings. The thermoplastic tow is heated to its processing temperature above its melting temperature such that it fuses with the substrate. This bonding by way of intermolecular diffusion or autohesion is from entanglement of the polymer chains at the tow-substrate interface. Currently, a significant reduction of layup speeds is required to achieve a reasonable quality of interlaminar bonding. This is a different mechanism than the chemical crosslinking in a cure reaction of the thermoset.

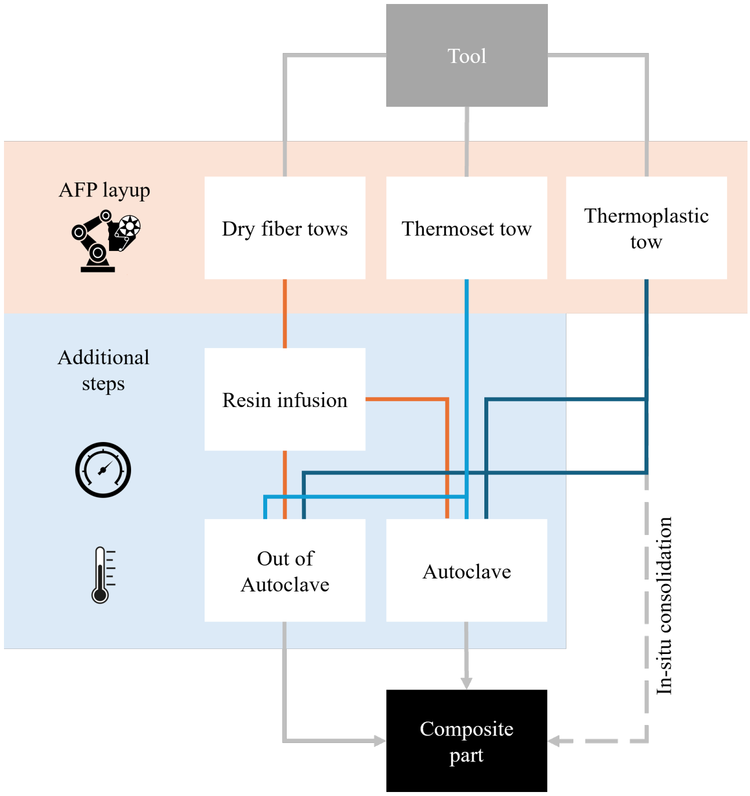

Figure 1.6: AFP routes.

Thus ISC-TP AFP manufacturing can potentially not require additional consolidation steps involving high temperatures and pressures. GKN Fokker has manufactured thermoplastic AFP control surfaces for the yet to be certified Joby S4 without an autoclave [19]. Their method of pressure application for consolidation is not known. Instead of pure ISC-TP AFP with no post processing step, some research is also being carried out on steps which are not as expensive as the autoclave. One example of such a technique is vacuum-bag-only (VBO) consolidation. However, such manufacturing techniques have not yet been applied to primary structures.

Dry-fiber is an alternative AFP tow material which consists of fiber held weakly by binders. It is cheaper than prepreg tows. Because there is no matrix material, it also drapes over tool complexities more easily. It doesn't require refrigeration like thermoset prepregs. Because of high out-life, it can be laid up over longer times. The heater can be lower powered since it just needs to bond using the tackiness of the binder. However, it needs infusion of the resin after layup. This infusion is typically with thermoset resins on lower viscosity. The wings of the Airbus A220 and the Irkut MC-21 are made by vacuum infusion of resin into a dry-fiber layup [20]. While the MC-21's wings are ATL made, they have not yet been certified yet. But they do use out-of-autoclave (OOA) processing [21]. The A220's wings use hand layup of dry-fiber with some future plans of automation.

1.3.3. Heating methods

Section 1.3.2 mentioned the necessity of heating various tow materials depending on their matrix to ensure appropriate bonding between the laid tow and the substrate. Various heater technologies like hot gas torches (HGTs), infrared (IR) heaters, lasers, and pulsed light heaters are used to achieve the required heat flux. The ability to change heating power and to direct the heat only in areas as required is crucial to have appropriate temperatures in various process conditions.

HGTs involve the oldest heating technology. It involves heating nitrogen gas and delivering it to the nip point by a nozzle. Temperature control is achieved by changing the flow rate. It is inexpensive but harder to control.

IR heaters transfer heat by radiation. IR lamps are mounted with reflectors to direct the heat towards the nip point. Power supply to them is controlled for achieving variable heat flux depending on the layup speeds. But IR heaters exhibit some time delay since they are dependent on filament heating and cooling. They are inefficient and have wide heat dispersion.

Laser heating devices are robust and exhibit precise and fast heat control. They are able to achieve the higher temperatures required for thermoplastic matrices. Their wavelengths are designed to appropriately heat the matrix and fibers without burning the matrix. Laser heaters achieve high, uniform and focused heat flux leading to good quality bonding. However, laser systems have requirements for Class IV laser enclosures and laser safe windows in addition to the standard robot cell safety measures. Also, some fibers and matrices may be transparent to their wavelengths, preventing heating.

Pulsed light heating systems are the most recent advancement. Their main advantage is having a more broadband emitter which doesn't require the laser enclosures and associated safety management, allowing operators to interact more closely with the equipment. However, these operators require appropriately dark personal protective equipment (PPE) glasses for eye protection from the bright light while functioning in the manufacturing environment. Other advantages include its broadband frequency range which heats a wide variety of fibers and matrices along with its heating precision and scalable widths. However, the layup speed often needs to be reduced to ensure good bonding. Also, the heating effects from the light which has escaped from the sides of the directing crystal is an issue due to deconsolidation damage of the adjacent tows, aging of AFP head components and energy loss.

Table 1.2 summarizes these sources based on the material systems they can be used for along with the achievable temperatures and temperature control.

Heating system	Material	Controllability	Temperature
HGT	Thermoset/thermoplastic	Low	Medium
IR	Thermoset	Medium	Low
Laser	Thermoset/thermoplastic	High	High
Pulsed light	Thermoset/thermoplastic	Medium/high	Medium/high

Table 1.2: Summary of various AFP heating systems [18].

1.3.4. Layup speed, tension & compaction

As higher production rates with no compromise in quality are the goal of any aerostructure manufacturing operation, higher layup speeds of more than 1.25 m/s are desired in AFP layups. However, layup speeds are often reduced in the complex areas of the tool to meet quality requirements. Lower layup speeds allow for a longer time of elevated temperature and pressure conditions on the tow. This leads to better tow-substrate bonding. At the start of the course, lower speeds are used to ensure that the tows stick to the substrate. The speeds can increase once the tow is stuck and the process has stabilized. This is also applicable to the first ply which is harder to stick to the tool than further plies to a tow substrate. Steering conditions may also require lower speeds to ensure defect free layup. The layup speed is often used to inform the heater power, since slower speeds would mean for higher time under the heater.

Tension is created in the tow as it is being pulled by the compaction roller from a spool which has brakes. These brakes can be of magnetic, pneumatic or frictional types. More advanced payoff systems have a servo creel which can control tension more precisely than purely mechanical systems. This tension is necessary to keep the tow taut and avoid defects. Higher tension which overcomes the tow adherence will lead to tow slips. Tow splices can detach due to high tension and lead to a missing tow defect. It can also lead to tow bridging in concave areas of the tool.

The compaction force is non-linearly dependent on the strain of the flexible roller. The TCP (Tool Center Point) on the roller surface is programmed at a deliberate depth inside the tool leading to the roller strain. This compaction helps achieve better bonding or consolidation during layup of both thermosets and thermoplastic tow materials. Compaction roller materials are chosen for good conformance to the tool surface complexities along with its durability to prolonged heating conditions. With the advent of thermoplastic matrices requiring higher process temperatures, the rollers now feature active cooling.

1.3.5. Manufacturing process planning

In the industry, the manufacturing process plan is ideally taken into account in the design phase of a composite part. This concurrent approach ensures that the decision making and engineering compromise related to the composite design, the chosen composite material and other manufacturing resources are matched to achieve a successful process plan. The objective is to manufacture parts which match as closely as possible, the composite design which was created to meet structural performance needs. The manufactured part needs to be able to be checked for quality and conformance. The manufacturing process plan creation will affect the labor and material costs during serial production. It will affect the ship-set production speed and thus have significant economic impact. The steps in process planning are complex and iterative. They require the manufacturer's knowledge base, the planner's expertise and computer-aided manufacturing (CAM) software tools to achieve an optimized process. The steps have been outlined below. The reader is referred to the cited source by Harik et al. for a more detailed review [18].

Boundary definition

The composite layup is typically larger than the final composite part. This is usually because lower quality edges of the layup have to be cut and discarded. Thus tools are made to be larger than the layup to account for the runway phases of the layup and spaces to bond consumables like vacuum bags. Boundaries are defined to identify the areas where material will be laid up. This is useful for collision analysis of the robotic movements during layup. Areas are also defined within the edges of a layup to identify ply boundary areas. These often change through the thickness of the part to have gradual ply drops.

Toolpath creation

The layup of material on a tool needs to match closely with the designed fiber orientations without exceeding the maximum allowable number and magnitude of gaps and overlaps. When the tow is laid on a complex surface, a reference curve is created which is then shifted to create toolpath for laying adjacent tows or courses. The reference curves can have constant angle (also called rosettes) or constant curvature (also called natural or geodesic). Constant angle strategies give control over the fiber angle over the tool while constant curvature strategy loses the control over fiber angle to avoid steering conditions.

Starting point

The starting point along with the fiber angle decides the initiation of the toolpath creation for the first course and in effect of the multiple adjacent passes which will cover the layup boundary area. The starting point is dependent on the tool geometry, roller and course widths. They are typically selected by trial and error with the aim of not having unnecessary defects in the layup. Unavoidable defects are kept further away from structurally critical areas of the layup.

Tow width selection

The tow size is selected based on the complexity of the part. Smaller widths allow for better conformance and coverage of the tool as compared to wider tows. The tow widths of supplied material needs to be verified to match the selected values in toolpath creation algorithms. 12.7 mm (1/2 inch), 6.35 mm (1/4 inch), 3.175 mm (1/8 inch) wide tows are most common. Courses have a higher number of tows as tow widths get smaller to keep deposition rates high. More number of tows and their lower width tows lead to increasing complexity of the creel and the tow delivery system and can lead to reliability and maintenance issues.

Steering constraints

Steering or laying up tows in curvilinear directions can be structurally advantageous. However, steering often leads to in-plane and out-of-plane defects especially for tighter steering radii. The minimum allowable steering radius constraint is dependent on the tow material properties and the tow widths. Layup toolpaths are created with constraints on the steering values especially for complex curvatures. For tighter steering conditions and wider courses, steering conditions may differ along the course. Thus, these steering constraints are calculated not just at the course centerline but also at the tow centerlines.

Programmed tow/course shifts

AFP toolpath programming applications allow for the adjacent tow/course offset to be varied to aim for the desired gap and overlap magnitudes. Programmed shift values or interband offset values are typically selected to minimize gaps and overlaps. Figure 1.7 illustrates adjacent courses which have been shifted by a certain amount.

Stagger shifts

To avoid having gaps and overlaps to align closely and stack up in adjacent laminae with the same orientation, the tow/course start points are staggered in directions perpendicular to the layup direction. Figure 1.8 illustrates the cross-sections of staggered tows.

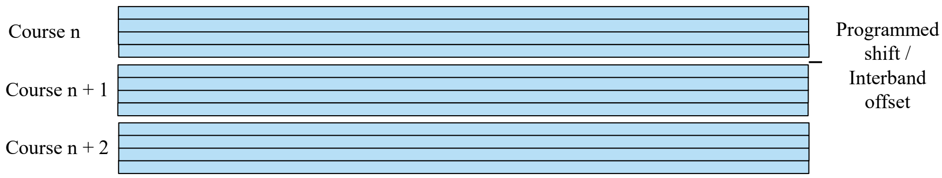

Figure 1.7: Schematic showing the programmed shift between 4-tow courses [18].

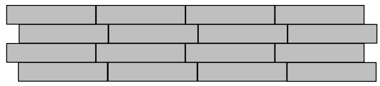

Figure 1.8: Schematic showing staggered tow cross-sections [18].

Boundary coverage & dog ears

Most AFP machines can cut tows only in the direction perpendicular to its length. When laying up tows which end up at an angle to the layup boundary, triangular shaped excesses or deficiencies will form. These are adjusted according to the size of the the layup edges which will be discarded. AFP machines also have a minimum cut length for a laid tow. Because of this shortcoming, corners have 'dog ears/bird's beaks' which are excess tow lengths beyond the part boundaries. Figure 1.9 illustrates tows which have been laid to have excesses beyond the boundary. It also shows dog ears/bird's beaks.

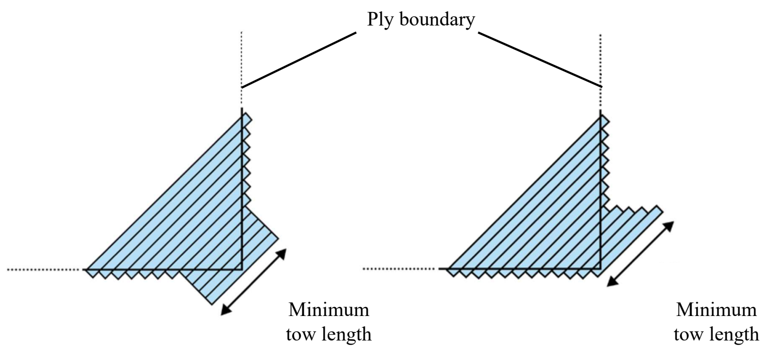

Figure 1.9: Effects of the minimum tow length. Image source [18].

Robot motions and kinematics

Robot travel time can be reduced if the robot does not have to return to the starting side of the layup after every pass. The layup can be made bidirectional such that the AFP head rotates 180 degrees. This decision is made depending on the layup length and the time required to rotate the head. Depending on the tool, tool jigs and mandrel supports, robotic travel motion can be further optimized to increase deposition rates. The machines can also be programmed to have differing speeds and accelerations for the approach, layup, cutoff stops. These speeds and accelerations can be tuned appropriately for various areas of the layup. Since robots have numerous degrees of freedom, the same toolpath motion can have different solutions using the various robotic axes and joints. Kinematic tuning can help with robot make and model specific optimization for longer times between robot actuator joint calibrations and maintenance.

1.4. AFP/ATL market overview and prospects

While the preceding sections have covered the technical aspects of AFP and ATL processes, it is also important to place these technologies in an industrial context. Their adoption across aerospace programs is governed not only by technical capability but also by production economics, certification status, and supply-chain considerations. This section provides an overview of the current AFP/ATL market and discusses their role and prospects within the aerospace industry.

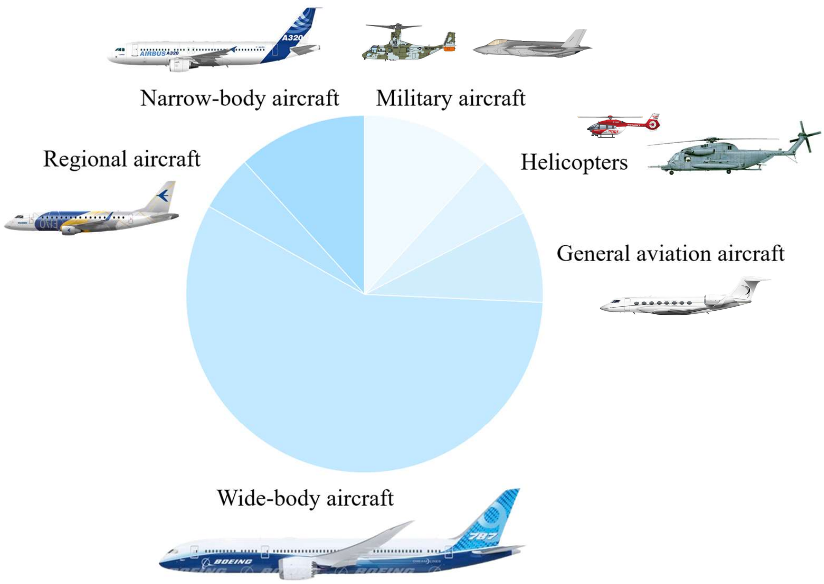

Figure 1.10: Market division of AFP/ATL made composite parts [22]. Copyright remains with the original image sources [23–28].

AFP and ATL are often clubbed together in market analyses due to their similarities. Figure 1.10 shows the market division of AFP/ATL made composite parts in the period 2019-2024. One can notice that wide-body aircraft parts make up for the biggest share of the market. AFP/ATL made composite parts are used in most aerospace structures programs in smaller aircraft and rotorcraft as well. There also exists a market for AFP/ATL parts in the space launcher and missile businesses. However, data for these was not available. The AFP market is bigger at $2 billion USD compared to $0.45 billion USD for the ATL market (2018 data). The AFP market is also growing faster at 8% compound annual growth rate (CAGR) compared to 7.2% CAGR for ATL (2018 data). Looking at the growth of composite weight percentage in aircraft through the years as seen in figure 1.1, the prospects of AFP composites in the aerospace industry are positive.

The AFP composites industry consists of a few different groups - AFP machine manufacturers, aerostructures manufacturers, composite material manufacturers and CAM software companies. The machine manufacturers build AFP robots while aerostructures manufacturers will use them in manufacturing cells to make parts. They need to have significant capital investment capabilities to buy and install AFP systems. Material manufacturers are those that manufacture the tow materials, slit them to various widths and spool the tapes. Various CAM software are available to program these machines to lay down material.

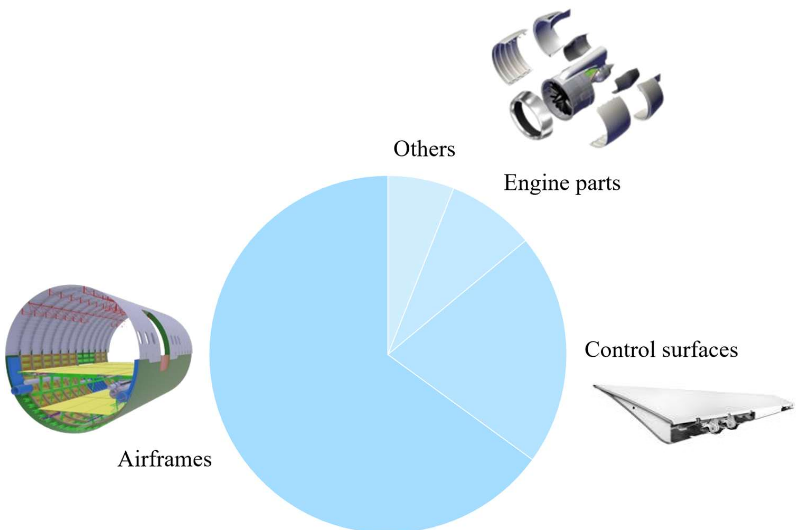

Figure 1.11: Market division of AFP/ATL made composite parts by application in aircraft [22]. Copyright remains with the original image sources [29–31].

Figure 1.11 shows the market division of AFP/ATL made composite part types in the period 2019-2024. AFP is used to make a variety of large composite parts which include fuselage barrels, wing skins, tailplanes, control surfaces, engine shrouds and blades, rocket cylindrical sections, fuel pressure vessels etc.

Figure 1.12 shows some pictures of industrial AFP setups from around the world. It is common for AFP parts required for an aircraft to be made at several different locations and shipped multiple times for integrations with other subsystems before it reaches the aircraft manufacturers final assembly line. For example, the Airbus A350s lower wing skin is manufactured in Illescas, Spain and its upper wing skin is manufactured in Stade, Germany. These are shipped to Broughten, UK and then to Bremen, Germany for further assembly. The A350s rear fuselage barrels are manufactured in Illescas, Spain and its center fuselage sections are manufactured in

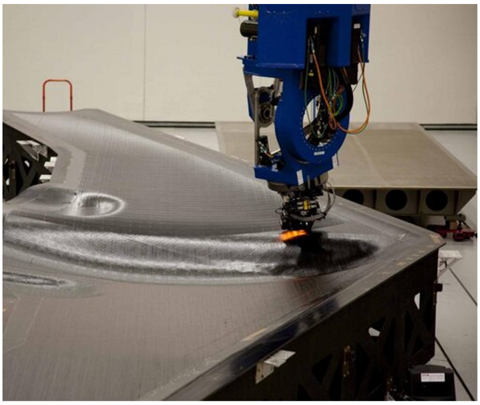

(a) AFP layup of the bottom skin of Lockheed Martin's flying wing aircraft in Palmdale, California [32].

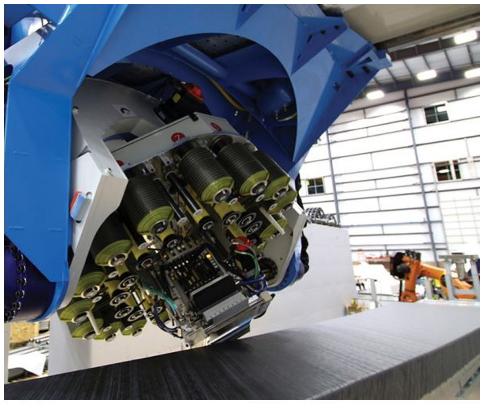

(b) ElectroImpact AFP machine laying up the wing spar of the Boeing B777X in Everett, Washington. [33].

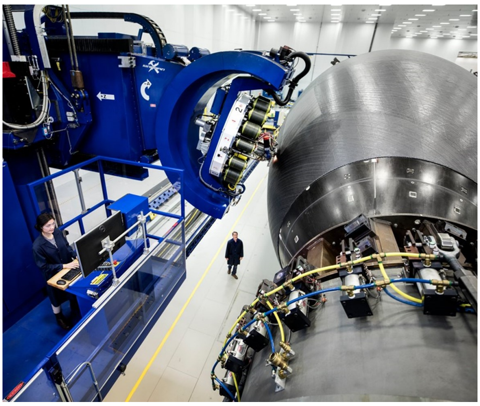

(c) ElectroImpact AFP machine laying up the front fuselage section of the Boeing B787 in Wichita, Kansas [34].

(d) MTorres ATL machine laying up of the bottom wing cover of the Airbus A350 in Illescas, Spain [35].

Figure 1.12: Industrial AFP/ATL composite manufacturing setups.

Kinston, North Carolina. These get further assembled and integrated with other subsystems in St. Nazaire, France and Hamburg, Germany. All of these then reach Toulouse, France for final assembly. Similarly, the Boeing B787's final assembly is carried out in Charleston, South Carolina. However, the B787's wings and forward fuselage barrel are manufactured in Nagoya, Japan. The forward fuselage section along with the nose are manufactured in Wichita, Kansas. The center fuselage section is manufactured in Grottaglie, Italy. The aft fuselage section is manufactured in South Carolina itself. The AFP parts are thus part of a supply chain which involves aerospace OEMs and manufacturers over multiple continents. Thus, expertise and exchange of knowledge is needed across many manufacturing locations. New aircraft manufacturing programs often face teething quality and assembly issues in part due to this global supply chain.

1.5. Defects in AFP composites

The AFP manufacturing process results in numerous different types of defects in the composite layup. These defects are a major drawback of the process because they deteriorate mechanical performance of the finished composite laminate. They also slow down the manufacturing process because the layup needs inspection.

Various kinds of defects which can occur during an AFP layup are listed in table 1.3 [36]. Note that some of these defects are hard to identify. They do not have definitions to geometrically distinguish between them. Gaps and overlaps are the most numerous of all defects. These are covered more extensively in the chapter 2.

Defect type	Description
Gaps	Unintended spacing between the edges of adjacent tows within a ply.
Overlaps	Crossover of the edges of adjacent tows within a ply.
Wrinkles	Out-of-plane undulations of a tow, typically occurring during steering.
Boundary coverage	Incomplete or excessive material coverage at ply edges.
Folds	Localized transverse folding of a tow onto itself resulting in doubled thickness.
Wandering tows	Lateral deviation of a tow from its intended placement path near course ends.
Missing tows	Complete absence of a tow in a region of layup.
Position error	Misplacement of a tow relative to its programmed course location.
Puckers	Localized lifting or arching of a tow from the substrate surface.
Bridging	Lack of tow conformity to a concave surface.
Angle deviations	Mismatch between the intended design angle and the as-manufactured angle.
Twists	Axial rotation of a tow about its longitudinal axis.
Loose tows	Tows that are not fully constrained or compacted during placement.
Splices	Joining of two tow segments within a spool.
Foreign objects	Unintended inclusions of debris within the laminate during layup.

Table 1.3: Summary of common Automated Fiber Placement (AFP) defects [36].

1.5.1. Defect monitoring

During certification of AFP parts, the manufacturer must prove that their manufacturing process has adequate safeguards against defects. Defects need to be detected and removed in cases where they exceed the allowable magnitude. Most of the industry uses manual visual inspection which is time intensive and requires expertise and experience. The defects are hard to visually identify due to the low contrast between the laid tow and the substrate. Rapid and reliable inspection techniques would increase the productivity of the AFP cell. The quality control of the AFP layup can be done visually or is aided by automated inspection methods which use profilometry, thermal imaging etc.

Profilometry involves using sensors to measure the surface profile of the material laid down to reconstruct their geometric details. Laser line scanners (LLS) which use triangulation of reflected laser light are most common. As the LLS traverses the layup, a line of laser light is shone on the tow and substrate. This light reflects off the tow and is detected as a frame by an imaging sensor. These sensors have high frame rates and good resolution. The quality of the data may be negatively affected by shiny surfaces and features. Matte textured composite tow without the shiny carbon fibers on the surface are easiest to reliably detect. For other cases, filtering of the data is necessary to prevent anomalies in the data. Thermal imaging techniques which take advantage of the temperature differences between the laid tow and the substrate are not affected by texture and reflectivity issues. Inspection can be made ply by ply after each layup. But this requires that the AFP layup has stopped. Inspection sensors can be mounted on the AFP head to record data as the layup is ongoing thus reducing the inspection time. Sometimes, separate robots with the inspection sensors operate in tandem within the same robotic cell as the AFP robot. Various algorithms from the fields of computer vision and machine learning (ML) are also being developed to detect a defect in the recorded inspection data.

1.5.2. Defect repair

When a defect is found, a skilled technician manually repairs it with pointy needle shaped tools. The technician is provided guidance by a laser projection system which identifies the location of the defect. For thermoset materials, defects are easier to repair when the repair starts closer to the time of defect formation. As time passes adherence becomes stronger and peeling the defective tow can cause more damage. Reheating can be used to make the peeling easier. The angle of peeling and the angle of the fibers in the substrate can affect the outcome of the peeling. Splicing of tows needs to be done with care of not cutting the underlying tows. Sometimes defective tows can be replaced by rerunning the AFP machine to dispense only the required tow. In some situations it might be easier to manually replace the defective tow. For gap and overlap defects in steered areas of the layup, the defect repair should be done by means of reprogramming rather than rework [37, 38]. For thermoplastic materials, defect repair without damaging the underlying layers is a challenge.

2

State of the art

न हि ज्ञानेन सदृशं पवित्रमिह विद्यते

— भगवद्गीता 4.38

Nothing purifies understanding as knowledge does.

— Bhagavad Gītā 4.38

In this chapter, the current state of the art on topics associated with gaps and overlaps in Automated Fiber Placement (AFP) composites is reviewed. The discussion begins with how these defects affect manufacturing productivity. This is followed by their classification based on causal factors. Existing work which motivates the need to predict gap and overlap formation in AFP laminates for process and structural modeling is reviewed. The relevant research addressing the manufacturing defects associated with variable stiffness laminates (VSLs) is then summarized. The chapter concludes by outlining the research objectives of this thesis in light of the identified gaps in current knowledge.

2.1. Effects of gap and overlap defects on productivity

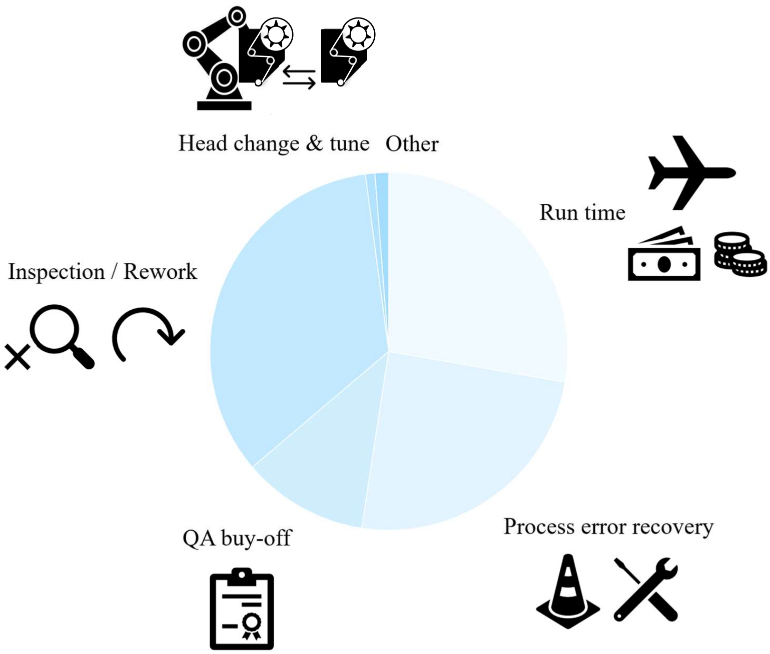

Figure 2.1: AFP celltime distribution from a double aisle aircraft manufacturing operation [39].

The percentage weight of composites in large aircraft has been rising as manufacturers pursue lighter airframes to increase efficiency [40, 41]. All the latest generations of large airliners have composite parts manufactured using Automated Fibre Placement (AFP) [42–44]. The new single aisle aircraft models expected to fly in the coming decade will also have large composite parts produced by AFP [45, 46]. AFP is a suitable, commonly used process for large composite part production and is expected to continue to be so. Huge backlogs in airliner orders translate to a need for faster manufacturing of these AFP composites. eVTOL aircraft are also being designed with lighter composite airframes to increase range. The proposed large fleets of electric vertical take-off and landing (eVTOL) aircraft will necessitate higher production rates, which may be enabled by AFP [47, 48]. The runtime fraction of an AFP cell should therefore be maximized to ensure high production rates.

Figure 2.1 shows the AFP celltime distribution for a double aisle aircraft manufacturing operation. The utilization time fractions show that inspection and rework take up ∼32% of the time [39]. This wastage of cell time is strongly linked to various types of AFP defects. Gaps and overlaps are the most common of all these AFP defects. For example, they were found to be more than 57% of all the defects for a representative helicopter part [49]. For typical aerospace AFP composites, there is an allowable magnitude of gaps and overlaps. During the layup, every ply is inspected for defects. If a gap/overlap defect bigger than the allowable is found, it is reworked manually. This reduces the run time of the AFP cell.

For thermoset AFP composites, gap defects occurring during the layup are filled up to varying extents by percolation and squeeze flow due to lower matrix viscosity and the time and pressure seen in typical autoclave cycles [50]. It is an industry norm to lay thermoset tow material with a deliberate gap [51]. This is to avoid overlaps and the associated mechanical knockdowns due to waviness of the layup in the vicinity of the overlap. These deliberate gaps lead to non-uniform fiber volume fractions. Cured laminates have shown a drop of 20-30% in fiber volume fraction in the regions of gap defects [52, 53].

For thermoplastic AFP composites which are to be consolidated in situ, the gaps and overlaps occurring during layup would remain as-is. Thus, gap and overlap defects would result in voids and fiber waviness [54]. These voids and fiber waviness result in deteriorated structural performance. The void percentage seen in in-situ consolidated (ISC) thermoplastic parts would therefore be a hurdle to certification if not below the conventional 1% mark.

Manufacturing process variations is one of the causes of scatter in the mechanical properties of aerospace composites. This scatter leads to a selection of more conservative values of allowables [10]. Thus, these manufacturing variations are linked to the overdesign of aerostructures leading to significant weight and economic impact [55].

2.2. Causes of gaps and overlaps

An ideal mesostructure for any performance-oriented AFP composite would have the tow laid such that the part has spatially uniform fiber volume fraction and desired fiber orientation. This would result in better mechanical performance and less part-to-part variation. This would require that the tow is laid beside each other and on top of other layers in an orderly and intimate fashion as seen in figure 2.2a. This means that the tow edges are in abutting contact with the edges of the adjoining tow. Gaps are produced when the edges of adjacent tows do not touch each other whereas overlaps are produced when the edges cross over. This is illustrated in the schematics of as seen in figure 2.2b and as seen in figure 2.2c.

2.2.1. The two major categories of gaps and overlaps

Gaps and overlaps can be classified according to their causes. Some gaps and overlaps occur due to an inherent limitation in tow path generation for parts that have tows laid in non-geodesic paths. This occurs in flat parts manufactured by fiber steering or in doubly curved parts due to their geometry. Tow paths are often generated by parallelly shifting a reference tow path. Depending on the amount of shift, the part has either gaps, overlaps or a combination of both at locations which can be predicted when the layup is designed before manufacturing starts.

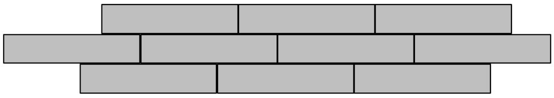

(a) Ideal

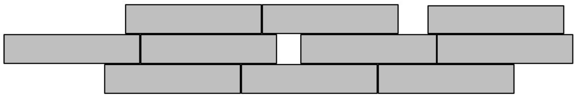

(b) Gaps

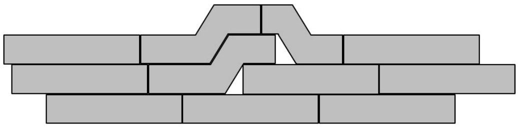

(c) Overlaps

Figure 2.2: AFP layup cross section schematic. Ideal AFP composite mesostructure with abutting tows (a), gaps (b) and overlaps (c).

This is illustrated in the schematics of figure 2.3. Other gaps and overlaps occur due to manufacturing process variations. This class of gaps and overlaps are defects that occur due to incorrect relative placement of the edges of adjacent tows. This placement can have 2 reasons: one, variation in positioning of the tow and, two, variation in geometry of the tow. This is illustrated in the schematics of figure 2.4 where the blue colored rectangle denotes the section of a tow being laid on the substrate. Figure 2.4a shows the ideal tow placement where the tow being laid is in intimate contact with the adjacent tow. Figure 2.4b shows the laid tow which has correct geometry but is in the incorrect position. Figure 2.4c shows the tow that has the correct position but has incorrect geometry.

Unlike gaps and overlaps occurring due to the shift of reference paths, the gaps and overlaps occurring due to manufacturing variations cannot be predicted before manufacturing. This means that it is not possible to know the frequency and magnitudes of defects that will occur in an AFP composite beforehand.

2.2.2. Gaps and overlaps due to manufacturing process variations

Figure 2.5 shows the further breakdown of these manufacturing process variations into possible sources. Tow position variation could occur due to robot end effector inaccuracy and lateral movement of the tow on the roller. Tow geometry variations could occur due to tow width and thickness variation of the incoming tow or due to tow deformation while being compacted by the roller. The following paragraphs introduce the four major sources of manufacturing variations seen in AFP manufacturing.

Robot inaccuracy

AFP robots are programmed to lay down tows on a tool using computer-aided manufacturing (CAM) systems. The toolpath defined in the CAM systems is converted into a trajectory of

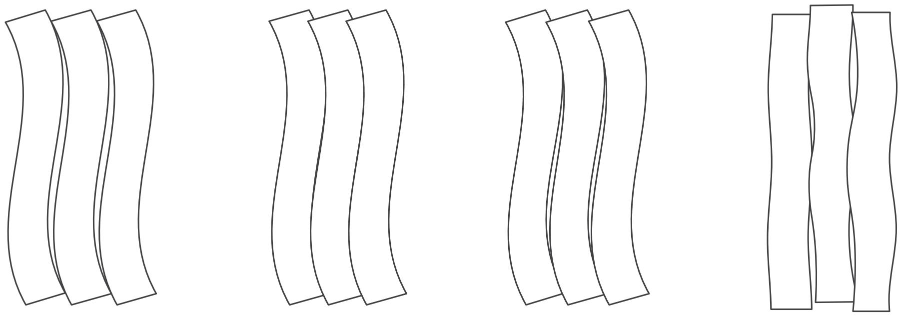

(a) **(b)** **(c)** **(d)**

Figure 2.3: AFP layup top view schematic. Gaps and overlaps caused by shifting of the tow path are illustrated in subfigures (a)–(c): (a) gaps only, (b) overlaps only, and (c) both gaps and overlaps. Subfigure (d) shows gaps and overlaps arising from manufacturing process variations.

(a) Correct position and geometry

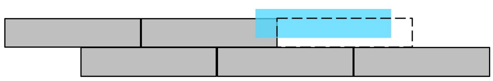

(b) Position variation

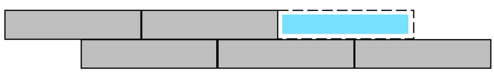

(c) Geometry variation

Figure 2.4: AFP layup cross section schematic – ideal tow placement (a), tow placement with position variation (b), tow placement with geometry variation (c).

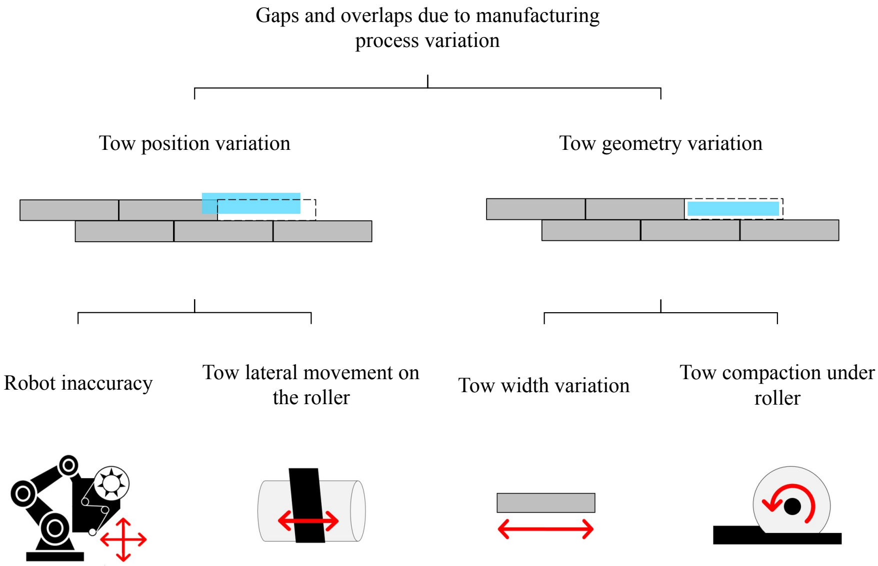

Figure 2.5: Breakdown of the AFP manufacturing process variations which cause gap and overlap defects.

the AFP head by the robot controller. The motion planning involves discretizing the defined toolpath into numerous linear segments, circular arcs or splines [56].

However, there is a difference in the planned toolpath and the achieved trajectory due to geometric, dynamic, thermal and system factors. Geometric factors include the inaccuracy of manufacturing of the manipulator parts and deflections due to loads like the AFP head weight and process forces. Therefore, the kinematic equations which relate the robot's joint space and cartesian space, do not do so perfectly. Such errors are expected to be higher in large envelope robotic cells, for example, those that make double aisle aircraft components. Dynamic factors like inertial loading and structural resonance can be significant for path-based control [57]. In many robotic applications, the end points of the motion need to be accurate. But for AFP systems, the path of the robot during laydown matters. Dynamic factors for an AFP head include the changing weight of the creels as the material is expended and reloaded. Another factor is inertial loading. Faster layup speeds are achieved by higher accelerations and decelerations in various phases of the layup cycle. However, this also reduces path accuracy.

Lateral movement of the tow on the roller

The tow feeding system of an AFP head moves a tow from the spool to the compaction roller using a system of pulleys and chutes. During the start of each course, the tow is extended below the roller before it approaches the tool and presses against it. During this time, the tow may move sideways due to self-weight and residual stresses. The tow is under tension as it goes under the compaction roller during layup. This tow tension acts against the lateral movement of the tow. Steering can also move the tow sideways on the roller due to lateral tractions on the tow [58].

Tow width variation

AFP systems lay unidirectional tow material which is manufactured by slitting wider prepregs. However, the widths and thicknesses of slit tow can vary from the specified dimensions. As the adjacent tow is laid by the AFP head, less than specified width will cause a gap defect while more than specified width will cause an overlap defect. A tow twist will also lead to width variation causing gap defects.

Tow compaction

During the layup, a heat source raises the temperature of the tow while the compaction roller applies pressure. The heat flux and compaction force values depend on the tow material. For thermoset tows, the temperature should turn the tow tacky enough for it to stick to the substrate. For thermoplastic tows being laid with in situ consolidation, the temperature and pressure should be enough to ensure good ply to ply adhesion and to remove air. These process conditions cause the tow to reduce thickness and increase width. This deformation during layup is seen in higher magnitudes for thermoplastic tows as compared to thermoset tows [59, 60].

In past work on these topics, various sensing techniques like laser line profilometry, optical coherence tomography (OCT) based profilometry, thermography and eddy current testing have been used on AFP heads to detect defects by sensing the tow while it is being laid. Thermography and eddy current techniques are better in detecting visually undetectable defects like loss of inter-ply adhesion. However, profilometry is most common due to its high profile rates and ability to robustly detect defects which change surface topography [61–64].

Various experimental setups which looked at the tow before and after compaction were built previously for objectives such as inline control of compaction force to affect width of the laid tow [65], online measurements of dry-fiber tow width variations to determine gap and overlap locations in the layup [66] demonstrating capability of inline control of process variables like compaction force, heating power and layup velocity [67]. Ghayoor et al. did full field DIC measurements of the compacted tow to understand deformations during AFP manufacturing [68]. Experiments by Uhart et al. show that even relatively small tool misalignments can lead to large changes in compaction forces. They developed an AFP head with hybrid position-force control to reduce the variation in compaction force in order to reduce gap and overlap defects while maintaining higher speeds [69]. Gonzalez Ojeda et al. looked at unwanted forces on the AFP head during layup on tools with complex corners and angles which in turn affects the accuracy of the layup process. They implemented a dynamic tool center point which updates according to a reduced order model of roller deformation behavior [70].

Accuracy of AFP robots has been measured and improved by using various techniques. Jeffries et al. have enhanced the accuracy of off-the-shelf manipulators by a secondary feedback loop using optical encoders [71]. Laser trackers have been used by various groups for reasons such as increasing the accuracy of large envelope AFP robots by optimizing the kinematic parameters per position and orientation along individual axes [72], plotting the repeatability at different speeds to find trade-offs in precision for increased production speeds [73], identifying and modeling geometric errors to upgrade kinematic models on gantry AFP machines [74], improving tooltip position accuracy by implementing a kinematic model calibrated to reduce variations due to deformation of the manipulator joints [75].

2.3. The need for prediction of gaps and overlaps

Gap and overlap defects are an inevitable reality of the AFP manufacturing process. Section 2.2.1 distinguished between gaps and overlaps occurring due to the shift of reference paths and the gaps and overlaps occurring due to manufacturing variations. The gaps and overlaps of the prior kind can be predicted before manufacturing unlike the gaps and overlaps of the latter kind which cannot be predicted before manufacturing. This means that it is not possible to know the frequency and magnitudes of defects that will occur in an AFP composite beforehand. If a predictive framework were available that could relate AFP process parameters to statistically representative defect populations prior to physical layup, it could enable more informed process design decisions. Such a capability would allow trade-off studies between the structural knockdowns due to gaps and the manufacturing costs due to overlaps. It would thus reduce reliance on costly prototype iterations.

Furthermore, statistically informed defect predictions could provide valuable input for certification activities, where understanding defect scatter, accumulation, and worst-case stacking scenarios is critical. By reducing uncertainty in defect populations, such methods could help mitigate excessive conservatism in process design and allowable development.

AFP manufacturing can involve layups with thermoset prepreg tow, thermoplastic tow or dry fiber tow, all of which lead to gap and/or overlap defects. These defects are expected to change shape during the later steps of manufacturing. They negatively affect structural performance depending on their severity and location. Thus, knowing the layup geometry along with information about the size and frequency of gaps and overlaps is of interest for manufacturing process simulations and structural modeling of AFP composites.

A layup with thermoset prepreg tow will spend time in an autoclave under increased temperature and pressure conditions causing the gaps to fill up. This happens because of the flow of the matrix due to its reduced viscosity or because of squeeze flow due to pressure on the tow. Kermani et al. proposed a model to predict ply thickness evolution of AFP layups with gaps while accounting for the squeeze flow of prepreg tow and its bending deformation in autoclave conditions [76]. Simacek et al. extended this model by accounting for matrix percolation effects [77]. Belnoue et al. and Jamora et al. implemented a coupled multi-physics finite element framework to simulate compaction behavior in layups with gap and overlap defects [50, 78].

AFP layup with thermoplastic tow could have follow-on steps designed to avoid use of an autoclave. Niens et al. developed models to predict the in-plane permeability of thermoplastic preforms and the air evacuation time for vaccuum bag only (VBO) processing of AFP preforms. These preforms were modeled to have a distribution of dimensions obtained from optical microscopy [79]. Khaleghi et al. measured void content in laminates made with multiple values of programmed shift using micro-CT scans [80].

Thus, all these investigations related to shape, size and property changes of the gap and overlap defect area in an AFP layup in processing conditions start with geometrical descriptions of the layup. If these process simulations are to be successfully applied to industrial AFP parts it would be necessary to have the accurate geometry descriptions of the AFP layup.

Fayazbaksh et al. created a defective layer method where the properties of finite elements are degraded in proportion of the defect area included in them [81]. Maraouene et al. also went for the flexible and efficient approach of assigning the 2D elements in the gap and overlap region with appropriate sectional properties having a matrix layer or an extra composite layer respectively [82]. Both these studies required the shape and location of the gaps and overlaps in a layup. Sawicki et al. modeled the waviness in the vicinity of gap and overlap defects of a composite coupon in a finite element model by matching the geometry to the visual observations of micrographs [83]. Del Rossi et al. implemented a half-gap and half overlap layup geometry as a trapezoid in their finite element model [49, 84]. Diemar et al. segmented X-ray micro-CT scan data to inform the cross section geometry and material properties of their AFP coupon model [85]. Li et al. implemented a 3D meshing tool which generates ply-by-ply models with gaps and overlaps of specified magnitude and location while capturing the ply thickness variations and ply waviness [86]. Chen et al. carried out a consolidation simulation of an AFP layup with gaps and used it to inform the geometry of a structural model [87]. Thus, modeling the structural effects of gap and overlaps in AFP composites requires information about the size and frequencies of the occurrence of these defects.

Various process and structural modeling efforts can benefit from accurate geometric layup information. AFP layups have gap and overlap defects due to manufacturing process variations which cannot be predicted before the layup. To the best of the author's knowledge, previous AFP tow models only use deterministic geometry. The objective was to use statistical information about the sources of manufacturing process variations which cause these defects to predict the tow geometry along with the resulting gaps and overlaps. This could lead to a virtual AFP layup geometry representation which is defect equivalent to real AFP layups at the mesoscale level.

2.4. Steering in AFP layups

To the authors' knowledge, currently, the aerospace industry only lays down tows in a straight or geodesic path. The AFP process has expanded the design space of composite laminates by enabling the layup of tows in curvilinear paths. This enables further tailoring of the laminate's properties for the design of composite parts which operate under non-uniform stress states. It has been shown that such variable stiffness laminates (VSLs) can improve stiffness, strength and dynamic performance. Some of these studies also consider geometries with cutouts [88].

These theoretical advantages of VSL designs can be applied to commercially important AFP shapes like flat/slightly curved plates, cylinders, cones etc. Some examples of AFP manufactured VSL parts which would involve steering conditions include wing covers (with and without access holes) and aircraft fuselage sections with window holes. The aerospace industry does not actively use steering in the manufacturing of certified AFP composites. Though the intent is to avoid steering conditions as much as possible, some layup paths do result in steering conditions due to the curvature of tools.

Research on VSLs seems to be shifting focus from theoretical structural performance improvement efforts to the practical manufacturing hurdles to be overcome to reliably produce defect-free structures [89]. The manufacture of VSLs brings to fore various technical complications which need to be overcome to advance the use of VSLs in the industry. Some groups have performed studies about the practical aspects of manufacturing VSLs. These studies involve analytical modeling or finite element analysis along with experimental efforts.

Beakou et al., Matveev et al., Belhaj et al., Bakhshi et al. and Wehbe et al. analytically modeled local parts of the tow after it has been laid up on a tool. The tow was modeled as a buckled plate with three simply supported edges and one free edge. These models minimized strain energy in the tow stuck to a foundation. The tow is acted on by in-plane compressive loads originating from the strain due to steering. The analytical work resulted in convenient closed-form solutions but also required significant assumptions. All these models aim at developing an understanding of the combination of material and process parameters which lead to the formation of wrinkling defects. They also calculated the critical steering radius for wrinkling defects. For layups with steering radii less than the critical steering radius, the models also predicted wrinkling frequency and amplitude along with time dependencies [90–95].

Bakhshi et al. did layups at various steering radii and process parameters. They modeled the deposition process using finite elements to predict the trends and frequency of wrinkles and blisters [96]. Rajan et al. performed a finite element analysis of the tow under the compaction roller in steering conditions and found mode II and mode III tractions at the tow-substrate interface under the compaction roller. The tow-roller shear force also acts in the radial direction [58]. These forces have a radial component which may cause the tow to move on the roller in the radially outward direction. Wang et al. created a finite elements model framework for the deposition process which can account for viscoelastic and temperature-dependent behaviour of the tow. They achieved qualitative and quantitative predictions of out-of-plane defect formation and deposition quality [97]. The focus of all of these aforementioned analytical modeling or finite element modeling studies has been on formation of wrinkling defects.

Wehbe et al. worked on in-plane defects such as tow waviness, bunching and gaps. They classed these in-plane defect types together and used statistical correlation to find that steering radius is the most significant process parameter causing this class of in-plane defects [98]. Legenstien et al. and Füssel et al. studied the strain behavior of highly aligned discontinuous fiber thermoplastic tow during stretch-steering and also recorded the presence of a drift/inaccuracy requiring a tool center point (TCP) offset [99, 100]. The stretch-steering AFP process and the discontinuous fiber material varies significantly from the conventional AFP layup process and tow materials. Raps et al. worked on the critical arc length after which wrinkles appear during steering with in-situ consolidated thermoplastic AFP [101].

In summary, all the aforementioned studies created important new insights. However, the phenomenon and mechanism of tow lateral movement at the compaction roller during steering layup of continuous fiber material had not been measured and studied. This tow lateral movement phenomenon leads to gap and overlap defects in VSLs.

2.5. Research objectives

Relative significance of the sources of manufacturing process variations

To the authors' knowledge, the sources of variations - robot inaccuracy, lateral movement of the tow on the roller, tow width, tow width after compaction - have not been measured simultaneously. There are existing setups which detect defects, however the individual contributions of these sources as well as the interactions of these variations to gaps and overlaps are not known. Moreover, tow lateral movement has never been measured.

The four aforementioned manufacturing variations occur concurrently and together determine the tow position and geometry deviations away from specified values. In turn, these tow positions and geometries determine the gaps and overlaps that occur in an AFP composite.

The objective was to investigate the relative significance of these sources of manufacturing variations by building an experimental framework to measure them simultaneously. Once these individual contributions were known, we evaluated if it was possible to fit these distributions from a number of runs and then use them to predict the defects that would occur in the layup. This evaluation was done by comparing the predicted gaps with the experimentally measured gaps.

Predictions of gaps and overlaps

AFP manufacturing can involve layups with thermoset prepreg tow, thermoplastic tow or dry fiber tow, all of which lead to gap and/or overlap defects. These defects affect various consolidation related phenomena during the manufacturing. Thus, any investigation related to shape, size and property changes of the gap and overlap defect area in an AFP layup in processing conditions start with geometrical descriptions of the layup. Gap and overlap defects also negatively affect structural performance of the manufactured laminate depending on their severity and location. Structural simulations aimed at assessing strength, stiffness, and damage initiation therefore depend on representative geometric descriptions of defect populations within the laminate.

Thus, knowledge of the initial layup geometry, together with statistical information on the size and frequency of gap and overlap defects, is of interest for both manufacturing process simulations and structural modeling of AFP composites. AFP layups have gap and overlap defects due to manufacturing process variations which cannot be predicted before the layup.

To the best of the author's knowledge, previous AFP tow models only use deterministic geometry. The objective of this work was to use statistical information about the sources of manufacturing process variations to predict tow geometry and the resulting gap and overlap defects. This approach enables the generation of virtual AFP layup geometries that are defect-equivalent to real AFP laminates at the mesoscale level.

Tow lateral movement

The tow lateral movement which contributes to the formation of gaps and overlaps during manufacturing of composite parts has not been investigated under steering conditions. Past work regarding the mechanics of the tow in AFP layups suggests that this tow lateral movement phenomenon may worsen under steering conditions. Lateral movement of the tow at the compaction roller is a source of manufacturing process variation which causes incorrect tow position. This would increase the magnitude of gaps and overlaps in VSLs. Studying the mechanism of formation of these gaps and overlaps during steering might lead to strategies to reduce them. The objective was to measure tow lateral movement under various steering conditions and to predict it.

3

Relative significance of the various sources of manufacturing variations in AFP composites

निमित्तमन्तरेण न किञ्चिद् भवति

— न्याय-वैशेषिक कार्यकारणभावः

Without a cause, nothing comes to be.

— Nyāya-Vaiśeṣika principle of causation

This chapter is based on the following publications:

- *Measuring sources of manufacturing process variations in Automated Fiber Placement composites*. Paper presented at the 23rd International Conference on Composite Materials (ICCM 2023), Belfast, United Kingdom.
- *Predicting gaps and overlaps in automated fiber placement composites by measuring sources of manufacturing process variations*. Composites Part B: Engineering, 2025; Vol. 291.

Chapter 2 introduced a breakdown of the sources of manufacturing process variations which cause gap and overlap defects. Figure 2.5 shows that the manufacturing process variations can occur due to position variation or geometry variations. The position variations can be due to robot inaccuracy or tow lateral movement at the compaction roller. The geometry variations can occur due to width variation in the tow material or the width variation due to deformation under the roller. The four aforementioned manufacturing variations occur concurrently and together determine the tow position and geometry deviations away from specified values. In turn, these tow positions and geometries determine the gaps and overlaps that occur in an AFP composite.

All these variations have not been measured simultaneously. Only when measuring simultaneously, can the relative significance be uncovered. Moreover, tow lateral movement at the compaction roller has never been measured. The objective was to investigate the relative significance of these sources of manufacturing variations by building an experimental framework to measure them simultaneously.

3.1. Experiment for measuring sources of manufacturing process variations

An experiment was designed to simultaneously measure the various sources of gap and overlap causing manufacturing variations during an AFP layup. These experiments were performed using an AFP machine at the robotic cell located at the TU Delft field lab – SAM XL (Smart Advanced Manufacturing XL).

3.1.1. Experimental setup overview

The measurement system consists of various sensors mounted on an AFP head as illustrated in figure 3.1. This system consists of an AFP-XS head made by ADD Composites as the end effector on a KUKA KR 210 R2700 robot manipulator linked to a KUKA controller. AFP-XS has a silicone compaction roller with a width of 31 mm and a diameter of 40 mm. The roller has a Shore hardness of 45A. It has an infrared heater which increases the tack of the thermoset tow during layup. It can lay down a single tow with widths of 6.35 mm (¼”), 12.7 mm (½”) or 25.4 mm (1”) [102]. The various widths are accommodated by way of custom chute walls which are screwed on with appropriate spacing. The AFP head is specified to have a maximum layup speed of 1 m/s, a minimum cut length of 85 mm and a maximum compaction force of 700 N.

The various sensors which make up the measuring system include a laser tracker - Leica AT960 MR, a camera - Ximea xiC USB 3.1 Gen1 MC050MG-SY-UB and two laser line scanners (LLS’s) – (A) MicroEpilon 3060-25 & (B) MicroEpilon 3010-25. These are annotated in figure 3.1.

The laser tracker measures the position of the AFP head. The camera views the tow position as it goes under the compaction roller. LLS A measures the profile of the tow in the feed system before it reaches the compaction roller. LLS B measures the width of the tow after it has been laid. The data streams from the laser tracker and the camera give an insight into the tow position variation while the data streams from the two laser line scanners (LLS A & LLS B) give an insight into tow geometry variation. For the LLS data, the focus will be on changes in width since these result in defects.

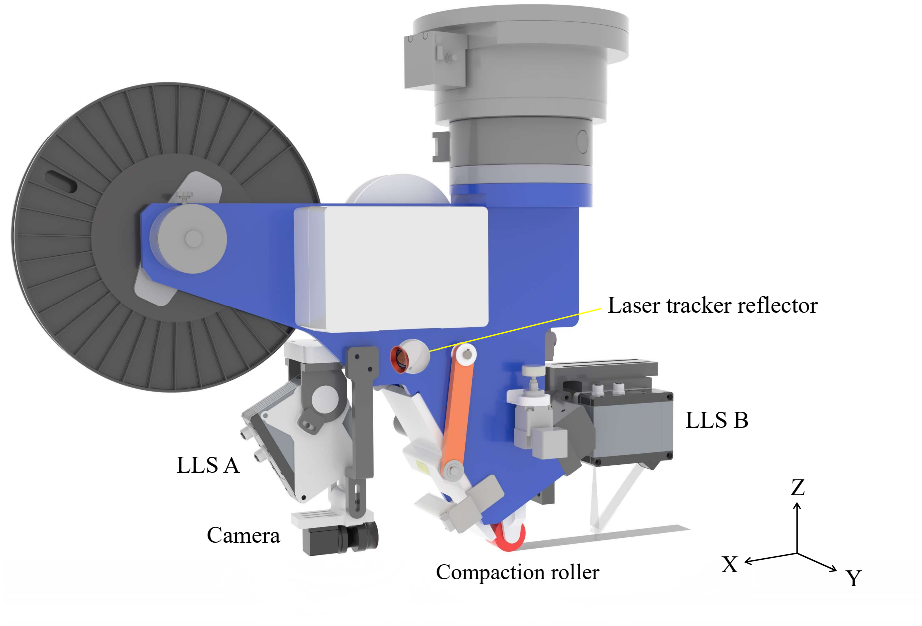

Figure 3.1: CAD model showing various sensors setup on the AFP head. Layup is in the positive X direction.

Mounts for the camera and laser line scanner sensors required for this experiment were custom-designed and manufactured with PLA filament using fused filament fabrication. The mount geometry was designed to rigidly hold the sensors while allowing them to be moved and set in relation to the tow they are observing. Data from the camera and LLSs is acquired via a high-speed USB cable and ethernet cables routed from the manipulator arm.

3.1.2. Layup procedure

The experiment involved laying down 6.35 mm wide unidirectional thermoset composite tow on a flat plate tool while recording tow position and tow geometry using the above-mentioned sensors. The aerospace grade prepreg tow was made from standard modulus carbon fiber with an epoxy matrix. The tool was a 1.5 m by 1 m rectangular steel plate which was clamp mounted on a measurement table. Note that it was not an aerospace grade flat tool. The 300 W IR heater was used at 80% power during layup.

31 straight lines of tow were laid. Each run was 1 m long. The maximum speed was set at 200 mm/s. The robot accelerated after the starting runway phase and decelerated for the stop at tow cutoff. It accelerated again at the end of the layup. Figure 3.2 shows the program details of the layup along with the velocity profile. The tow tension was set at 6.7 N using a magnetic brake. The straight-line layups were programmed in the X-axis direction such that the Y coordinate will remain constant for each of them. The 31 tows had Y coordinates of 125 mm up to 500 mm with increments of 12.5 mm. To ensure compaction, the Z coordinates for the layup were set at -4 mm such that the tool center point (TCP) moves below the table surface which is at Z = 0. The compaction force was measured to be 377 N.

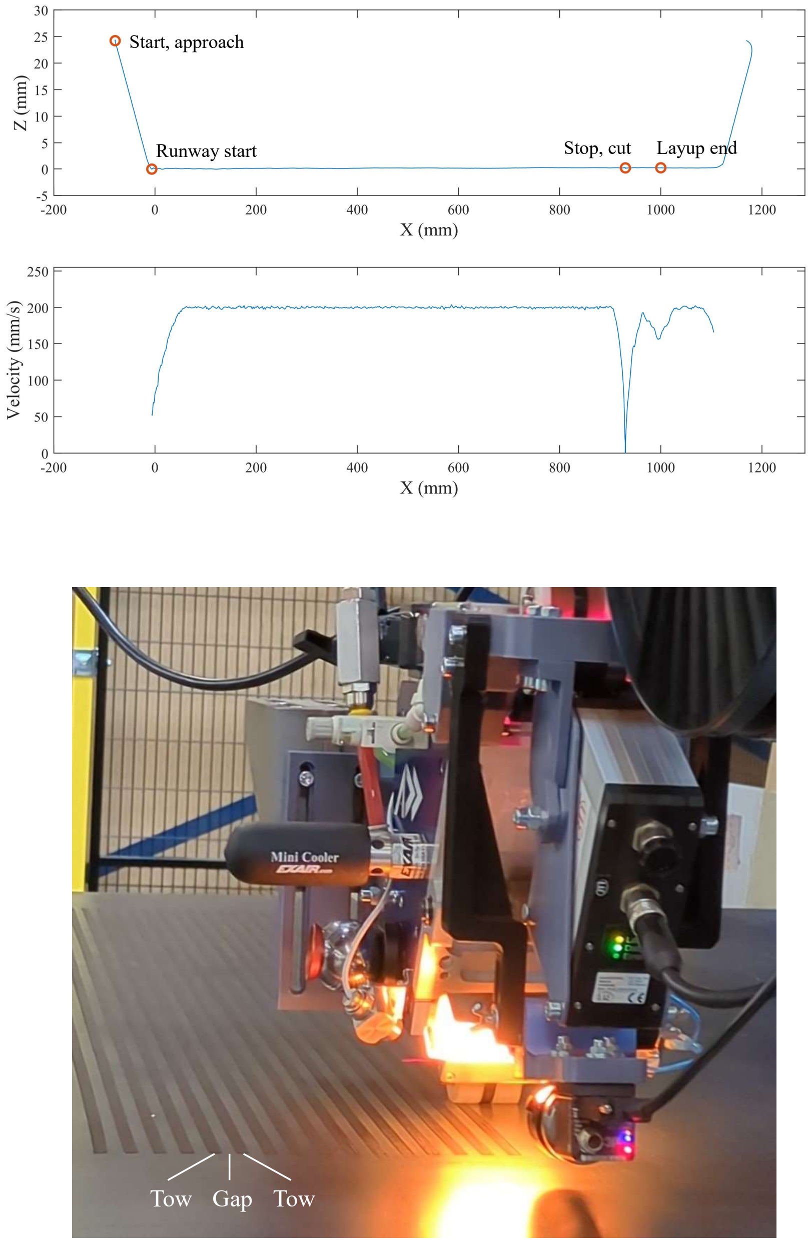

Figure 3.2: AFP layup. Program details (top). Layup velocity profile (middle). Tow no 17 being laid (bottom)

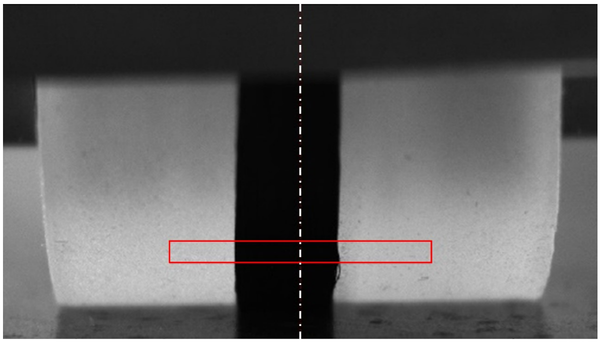

Figure 3.3: Example frame recorded by the camera. A measurement window is annotated in red while the roller center is annotated with a white dash-dotted line.

3.1.3. Data acquisition and analysis

The retroreflector required for the laser tracker measurements was magnetically attached to a mount/seat which was adhesively stuck to the frame of the AFP head. The laser tracker is a portable coordinate measuring machine (CMM) that uses a reflecting laser beam to measure the target's location and movement. The target is a retroreflector sphere with mirrors. The tracker model used for this experiment uses the Absolute Interferometer (AIFM) method [103].

The Leica Tracker Pilot application was used to operate and record the position from the laser tracker every 10 ms. Each position data point was accompanied by a timestamp. The laser tracker has a typical accuracy of ±7 µm in distance measurement [104]. The AFP head positions recorded by the laser tracker were that of the achieved trajectory.

The difference of the achieved trajectory from the programmed path, in the Y direction, is calculated for each recorded set of position coordinates. For example, run 3 had a programmed Y coordinate of 150 during the layup. A recorded Y coordinate of 149.028 mm would mean a deviation of 0.972 mm for that data point. As seen in figure 3.2, the retroreflector was eventually placed as close as possible to the TCP to minimize any effect of the possible tilting of the end effector on these deviation measurements.

The 5-megapixel monochrome optical camera was suitable because it is compact and lightweight. It has a 2464 $\times$ 2056 pixel CMOS sensor. The camera is specified to have an ambient operating temperature of operation from 0 °C to 50 °C. It allows for a smaller region of interest to be specified from within the full 2464 $\times$ 2056 frame thus allowing for faster frame rates. The camera was paired with a lens that provides manual control on the focal length [105].

The Ximea CamTool application was used to control and operate the camera. To maximize the frame rate, the camera data was acquired by operating it in a 'free-run' acquisition mode. The metadata from the application was used to get the timestamp for each frame.

The exposure time of the camera was set at 1 ms such that it captures an image that shows the black tow against the white roller with sufficient contrast for a certain heater power setting. This is because the heater power also corresponded with the illumination of the tow and compaction roller. Higher exposure times not only reduced the frame rate but were seen to increase bright spots of reflections of small surface features of the roller thus negatively affecting image processing required to detect the tow. The mean frame rate was 62.5 Hz. Camera resolution in detecting the edge position of a tow was ~ 16 µm.

The tow position on the compaction roller was measured using image processing on each recorded frame. For each frame I_i, the full image is cropped to obtain the measurement window defined by its top-left corner (x_0, y_0) and dimensions (w, h). This is done to reduce computational expense. Figure 3.3 shows an example frame with the measurement window of size 600 pixels by 50 pixels. The center of the roller is annotated with a white dash-dotted line.

$$I_i^{\text{cropped}} = I_i(x_0 : x_0 + w,\ y_0 : y_0 + h) \tag{3.1}$$

Figure 3.4 shows an example cropped frame. The cropped image has the region of the frame where the image is the sharpest.

Figure 3.4: Example cropped frame of width w and height h showing the tow with respect to the roller center line.

Each frame is cropped to the window size and the average intensity of each column of pixels is calculated.

$$\mu_i(x) = \frac{1}{h}\sum_{y=1}^{h} I_i^{\text{crop}}(x, y) \tag{3.2}$$

Since every pixel holds an 8 bit value which signifies grayscale between 0 (black) to 255 (white), $\mu_i(x)$ is a 1D intensity profile such that

$$\mu_i(x) \in [0, 255]$$

The black tow has a much lower intensity than the white roller. Thus, the edge of the tow with respect to the dash-dotted center line is calculated by detecting this change in average intensity. To detect the left and right edges of the tow, a change-point detection algorithm is applied to the intensity profile $\mu_i(x)$. This identifies two positions where the signal exhibits the most significant statistical shifts.

$$[x_L, x_R] = \text{ChangePoints}(\mu_i(x),\ N) \tag{3.3}$$

where x_L and x_R denote the pixel locations of the left and right tow edges, respectively. N is the number of needed change points. Since two edges were needed, $N = 2$. These values in pixels is converted to a metric measurement by using a pixel-to-mm length conversion scale. This scale is obtained from a reference image which has a checkerboard scale whose dimensions are accurately known from its micrograph.

The pixel-to-mm scale calibration was carefully planned and executed in the following steps :

1. The camera frame and lens focus was adjusted to get a sharp view of the region of the tow in the measurement window (annotated in red) seen in figure 3.3. The selected lens is manufactured for applications in 2D/3D metrology and robotics vision.

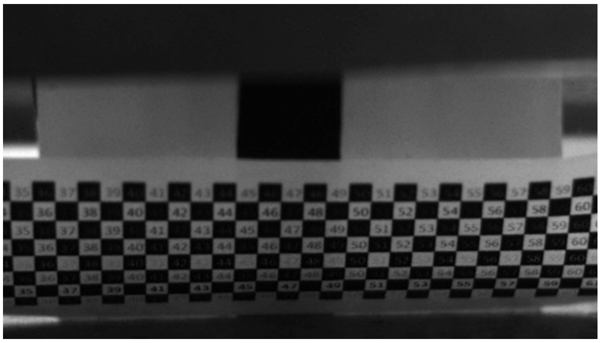

Figure 3.5: Example frame showing checkerboard scale.

2. The checkerboard scale was curved to match the curvature of the compaction roller and placed on it in different positions to capture several reference images. Figure 3.5 shows an example of an image with the checkerboard.
3. The calibration process used four reference images which were captured before the experiment and four which were captured after the experiment. This was to ensure that there was no change in the calibration value during the experiment due to camera mount movement due to the robot's motion.
4. The checkerboard scale is marked with numbers to make it easy to identify corners of particular squares. The distance between the corners of particular squares is compared between the micrograph and the reference images.
5. The earlier step was done eight times, once each for each of the eight reference images. Each reference image had different areas of the checkerboard in the measurement window. The average of these eight values was used for tow lateral movement calculations.

The LLSs are 2D profile sensors that were suitable because of their high profile resolution, high profile rate and proven past use in measuring composite tow dimensions [67, 106]. These scanners reflect a line of laser light off the composite tow and use triangulation to measure the profile of the tow. The profile of the tow is output as Y, Z coordinates for each measuring point where Z is the measured height at position Y along the laser line. The width of the tow is along the Y axis, the thickness is along the Z axis while the length of the tow/layup direction is along the X axis. This coordinate system is illustrated in figure 3.6. Both the LLSs have 2048 measurement points per profile. The measurement range for the sensors forms a symmetrical trapezoid with an average width of 25 mm in the tow width direction and a height of 15 mm in the tow thickness direction. Both sensors allow regions of interest to be defined to measure within fields smaller than the maximum available range to increase the profile rate [107].

The LLSs were operated using a Python API script. The profiles were recorded during the layup such that it would not be affected by the subsequent roller passes. The exposure time of both the LLSs was set at 4 ms such that it reliably captures the tow profile in the minimum possible time. The mean profile rate was 83 Hz. The LLSs have a Y direction resolution of 12.2 µm and a Z direction resolution of 1.5 µm.

Figure 3.6 shows example profiles from LLS A and LLS B. The tow edges are determined by detecting the sudden change in Z value. The difference between the Y coordinate of the two

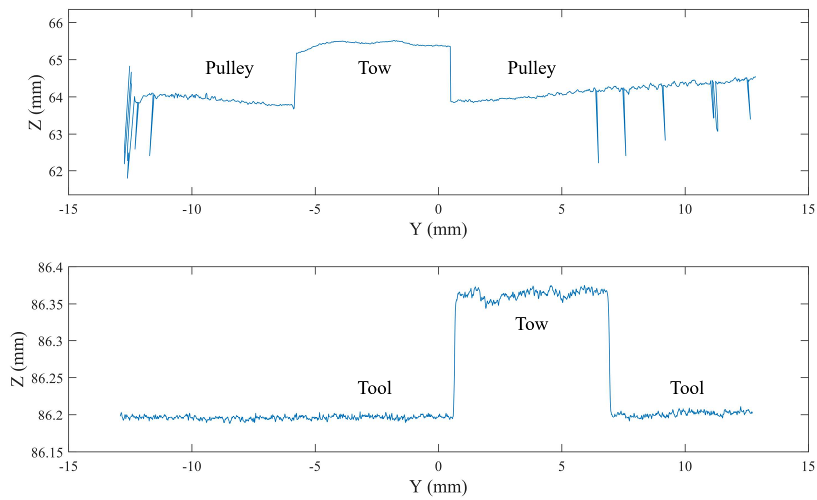

Figure 3.6: Example profiles measured by LLS A (top) and LLS B (bottom).

edges is used to calculate width from each such recorded profile. In case of LLS A the tow may not be flat since it is rolling between the spool and the pulley. A high-order polynomial fit is applied to the detected edge region to approximate the curved tow shape. The arc length of this fitted curve is used to compute a corrected width. The exposure settings are selected to best view the tow. This means that objects like the feed system or the table in the view of the LLS can be overexposed. Some simple threshold filters are used to remove the anomalous points from each profile. In rare instances, loose fibers were observed at the edges of the tow. The tow algorithms recognized the loose fiber as the edge of the tow. However, since this occurrence was rare, it had negligible impact on the broader dataset.

3.2. Experimental results

Figure 3.7 shows the distributions for the four measured variations - robot inaccuracy, tow lateral movement on the roller, tow width before compaction and tow width after compaction. The mean and standard deviation are marked in red at the bottom of each distribution. The distributions were obtained from measurements made during the layup of 31 tows where each tow was one meter long. As shown in figure 2.5, robot inaccuracy and lateral movement of the tow on the roller are causes of position variation while changes in tow width before and after compaction are causes of geometry variation.

While the data presented here is for the previously stated AFP head-material combination, the experimental methodology can be applied to various industrial AFP implementations to provide meaningful insight into the variation characteristics particular to that composites production setup.

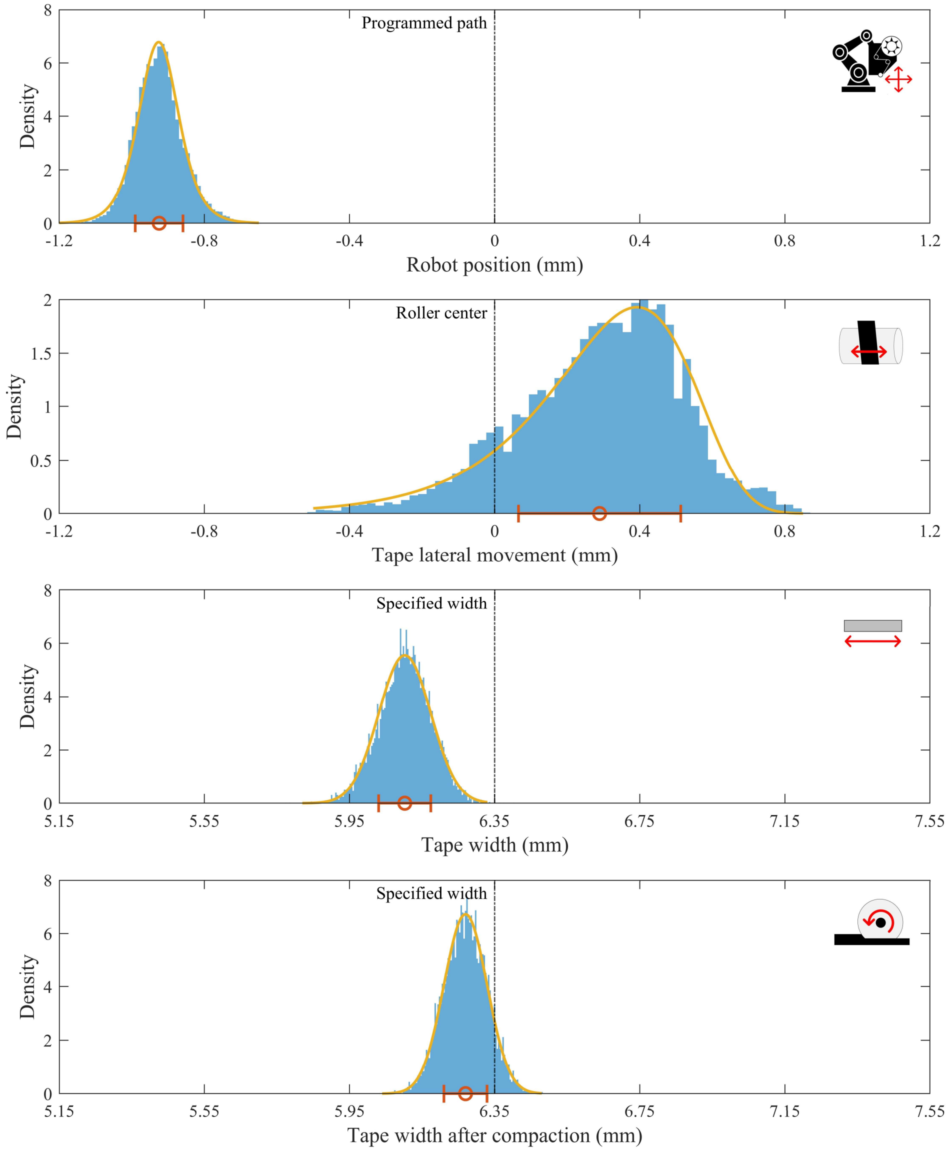

Figure 3.7: A, B, C, D (top to bottom). Measured manufacturing variations that cause gaps and overlaps. Note that the X axis is equally scaled. Means and $\pm 1\sigma$ values are annotated in red. Distribution fits are annotated in yellow.

	Robot inaccuracy	Tow lateral movement	Tow width variation	Tow width variation after compaction
Distribution fit	Logistic	Extreme Value	Normal	Normal
Range (mm)	0.54	1.4	0.63	0.48
Range as % of specified width	8.5%	22.1%	9.9%	7.5%
Mean (mm)	-0.93	0.29	6.10	6.27
Standard deviation (mm)	0.07	0.22	0.07	0.06

Table 3.1: Summary of measured manufacturing variations which cause gaps and overlaps.

3.2.1. Robot Inaccuracy

Figure 3.7 (A) shows the distribution derived from position measurements of the AFP head from the laser tracker. The data from all tows was shifted to have the programmed path centered at 0 mm. Robot position variations have been calculated in the Y direction i.e. the tow width direction. These variations would therefore be an indicator of how the achieved trajectory differed from the programmed path.

The distribution has a mean value of -0.93 mm. The mean is not close to 0 mm, which implies that the position variations are not centered on the programmed path. This implies that the achieved trajectory got pushed to one side of the tool. This could be because of the undulation on the table surface or related to the pose of the robot when it is laying tow on the tool. The range of deviation was 0.54 mm which is 8.5% of the specified 6.35 mm tow width. Figure 3.7 (A) shows that a Logistic distribution can be used to statistically model the variation in the AFP head positions. The chosen distribution is for this particular AFP setup and program.

The Logistic distribution captured the high central peak better than a Normal distribution. This better fit was confirmed with a comparison of log-likelihood values. If the robot inaccuracy was resulting due to the accumulation of several small random effects related to the robot control and hardware, it would have resulted in a normal distribution by virtue of the Central Limit Theorem (CLT). Thus, this departure from the expected Normal behavior could be due to the presence of systematic effects in addition to the random factors.

The spread of the distribution may increase for robot manipulators with bigger work volumes, heavier AFP heads, faster layup speeds, higher accelerations and decelerations in programmed paths etc. The spread of the distribution will decrease for AFP setups which have increased path accuracy of robots due to various strategies such as additional feedback loops, improved kinematic models or robot cell specific compensation [71, 72]. Various brands of manipulators have different actuator and joint designs. This is expected to affect the distributions along with their wear and maintenance conditions.

3.2.2. Lateral movement of the tow at the roller 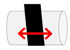

Figure 3.7 (B) shows the distribution derived from the tow position measurements made from camera frames. The center of the tow is tracked while the tow is on the compaction roller. These position measurements were made with respect to the roller center line as shown in figure 3.3. This roller center position is also annotated in figure 3.7 (B). The distribution is an indicator of how the tow moves laterally about its expected center position on the compaction roller.

The distribution has a mean of 0.29 mm which implies that the overall tow movement is shifted from the center of the roller. The range of deviation was 1.4 mm which is 22.1% of the specified 6.35 mm tow width. Figure 3.7 (B) shows that an Extreme Value distribution can be used to statistically model the variation in tow positions on the roller.

Of the four distributions for various sources of the variations, this distribution had the least samples. This is due to the frame rate limitations of the camera. It was observed that the tow was moving laterally on the pulleys in the feed system as well. It then passes through a rectangular metallic chute. This chute has a width clearance which reduces from 0.5 mm to 0 mm where the tow has minimal clearance to move. The tow then reaches the roller where it moves laterally as seen in the distribution plot.

During past experiments of the authors which used a pristine compaction roller, the distribution of tow lateral movement was centered almost exactly at the roller center line [108]. However, the present experiment used a compaction roller which was worn from earlier use. The wear and tear may have been asymmetrical due to the steering conditions during this earlier use. This wear could have been characterized by profilometry. However, at the time of the data analysis, the roller had been used for other experiments, thus preventing a post facto investigation into the appreciable wear profile and the possible non-uniform wear state during the experiment. A study which quantifies the roller wear state and isolates its effect on tow lateral movement is therefore recommended as future work. Such a study would be relevant to typical industry conditions of these rollers.

The spread of this distribution is expected to be narrower for tackier materials and for higher tow tension arising from the spool brake. This is because the tractions in the width direction which cause lateral movements will be opposed by friction forces and a component of the tow tension. The aforementioned experiment captured the tow lateral movement only for the first lamina being laid on the tool. Future work could look at the relationship of the tow lateral movement phenomenon to the substrates frictional properties for the subsequent laminae.

3.2.3. Tow width variation 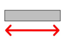

Figure 3.7 (C) shows the distribution derived from geometry measurements of the tow made with a laser line scanner. LLS A recorded profiles of the tow in the tow feed system before it enters the chute leading to the compaction roller. The tow width variation has been recorded by calculating the length of the top edge in each profile. The distribution is an indicator of how the width of the tow varies for the given batch of the unidirectional tow material.

The distribution has a mean of 6.10 mm and a standard deviation of 0.07. The mean value is less than the specified tow width of 6.35 mm. The range of deviation was 0.63 mm which is

9.9% of the specified 6.35 mm tow width. Figure 3.7 (C) shows that a Normal distribution can be used to statistically model the width of the tow.

The data indicates that the tow slitting process is quite well controlled for the used brand and specification of unidirectional tow. However, improvements can be made in the process to get the mean width to match the specified value and to reduce the overall spread. The tow raw material width is much less controlled for some other AFP materials like dry fiber tows used for resin infusion processes and for some newer material systems used for manufacturing ceramic matrix composites [66, 109].

Some tow materials are specified to have unilateral tolerance only on the lower side of the specified width. For example, $6.35^{+0.0}_{-0.25}$ mm. Preventing overlaps in the layup is usually more important than preventing gaps. This is because overlaps will lead to waviness which is a worse outcome compared to gaps.

3.2.4. Tow compaction 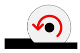

Figure 3.7 (D) also shows the distribution derived from geometry measurements of the tow made with a laser line scanner. LLS B recorded profiles of the tow after it was laid on the tool. The tow width variation after compaction has been recorded by calculating the edge-to-edge distance in each measured profile.

The distribution is an indicator of how the width of the tow varies after it has been compacted by the compaction roller. The distribution has a mean of 6.27 mm and a standard deviation of 0.06. The range of deviation was 0.48 mm which is 7.5% of the specified 6.35 mm tow width. Figure 3.7 (D) shows that a Normal distribution can be used to statistically model the width of the tow after compaction.

Of the four measured sources of manufacturing variations, this source had the narrowest spread. For the thermoset material that was used in this experiment, the spread was slightly smaller than the spread for tow width before compaction.

One can expect the average width increase to be much higher for thermoplastic tow materials. This is due to the squeeze flow of the tow under the roller in presence of the higher process temperatures and compaction pressures chosen to pursue a higher bond quality [65]. However, as the tow experiences elevated temperatures after the final sections of the feed system even before it reaches the nip point, the tow spreading already starts before the tow reaches the compaction roller [60]. The thickness of the layup also affects tow width change due to the changes in substrate compliance and thermal dissipation conditions [110]. The tow width increase due to squeeze flow is the highest for the first lamina on the rigid tool since all the deformation is absorbed by the laid tow. As the layup thickness increases, its compliance leads to lower squeeze flow of the laid tape. However, the process also runs hotter due to the lower conductivity of the thicker substrate. This leads to lower viscosity and higher squeeze flow and therefore competes with the earlier effect.

3.3. Utility for online correction

Table 3.1 showed that tow lateral movement was found to be the biggest contributor to gaps and overlaps. The following result proposes the utility of using the tow lateral movement data

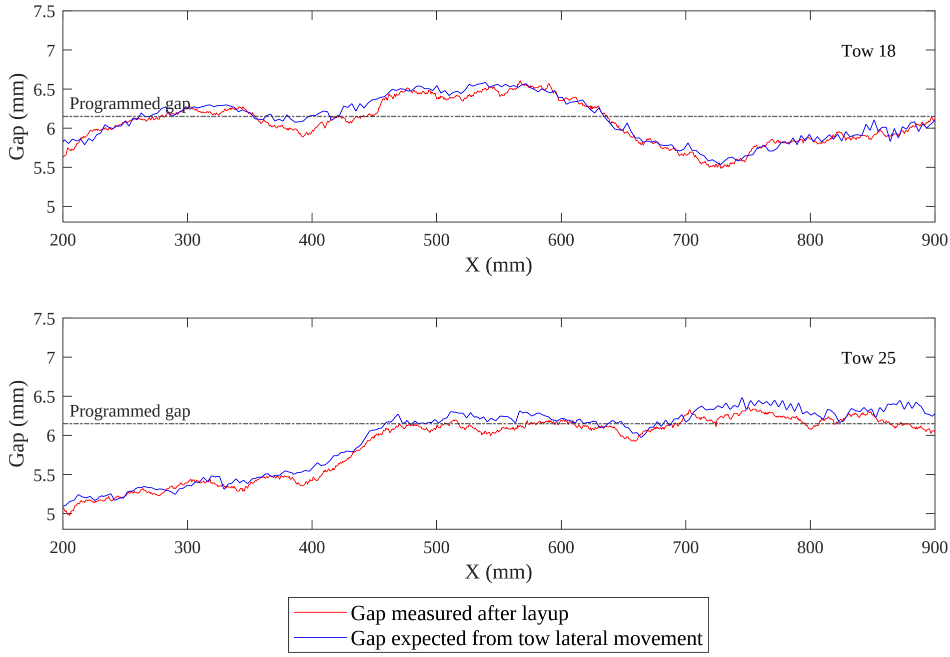

Figure 3.8: An individual tow level comparison of the measured gaps with the gaps expected from the tow lateral movement. This example data is from tow 18 (and its adjacent tow 19) and tow 25 (and its adjacent tow 26) respectively.

from the camera as feedback to the robot controller which can use it to compensate its path. This could lead to reductions in gap and overlap defects.

Figure 3.8 (top) shows the measured gap between tow 18 and tow 19, in red. These measurements were made by traversing an LLS over the laid tow. The gap can be seen deviating from the programmed gap of 6.15 mm. These deviations would lead to a higher number of defects. However, if the AFP robot detects these impending defects during layup, it can correct its position to compensate against them. Similar online corrections have been used to compensate against robot path inaccuracy and tow material width [65, 71].

The tow lateral movement data along with the mean tow width were recorded during the layup of tow 18 and tow 19 and were used in determining the edges of the tow, thus leading to the expected gap along the layup. This expected gap is shown in blue in figure 3.8 (top). The shown data has been appropriately shifted in the layup direction to align them. This was to correct the lag in the measured gap as compared to the tow lateral movement recorded on the compaction roller.

It can be seen from the figure 3.8 that for the chosen example runs, the gap expected from the camera data agrees closely with the measured gap data. A future AFP system could implement a feedback loop that uses this tow position information from the camera. The position detection and compensation calculation are not computationally expensive. Thus, future work can investigate if this approach could be used for online correction.

4

Prediction of gap and overlap defects in AFP laminates

अधिष्ठानं तथा कर्ता
करणं च पृथग्विधम् ।
विविधाश्च पृथक्चेष्टा
दैवं चैवात्र पञ्चमम् ॥
— भगवद्गीता १८.१४

The system context and the acting agent,
together with instruments of differing kinds;
the distinct and varied operations performed,
and, as a fifth factor, the unseen governing influence.
— Bhagavad Gītā 18.14

This chapter is based on the following publications :

- *Improving AFP process design using Markov Chain Monte Carlo simulations of laid tows.* Presented at the 7th International Symposium on Automated Composites Manufacturing (ACM7, 2026), Delft, The Netherlands.
- *Generating realistic estimates of AFP tow geometry for gap and overlap predictions.* Composites Part A: Applied Science and Manufacturing, 2026; In press.

The individual contributions of the sources of manufacturing variations in AFP layups were measured in the chapter 3. In this chapter, the objective was to evaluate if it was possible to use this statistical information about the manufacturing variations to predict the defects that would occur in the layups. This evaluation was done by comparing the predicted gaps with the experimentally measured gaps.

The gap and overlap predictions in this chapter have been implemented and presented at two levels. The aggregated statistical predictions describe the probabilities of the occurrence of defects on a lamina level. This is followed by tow-resolved predictions which are able to capture mesoscale features such as the tow waviness and gap lengths. This leads to a virtual AFP layup geometry representation which is defect equivalent to real AFP layups at the mesoscale level. Finally, the utility of these predictions for improving AFP processes are discussed.

4.1. Aggregate lamina-level predictions

Figure 3.7 shows the distributions for the four measured variations and the probability density functions which were fit to these four distributions. The distributions were obtained from measurements made during the layup of 31 tows. However, there may be thousands of such tows in an entire layup of a laminate. This section focuses on the hypothesis that the distribution fits from these few tows can be used to estimate the occurrence of gaps and overlaps in the entire layup, at least as long as the geometry of the tool and the layup path do not vary widely from those present when the data from these few tows were obtained. During a layup, gap and overlap defects in a certain lamina are expected to interact with similar defects in other adjacent laminae. These interactions will be neglected.

To predict gaps between two adjacent tows, many instances of the profile of these two tows were simulated. Each of these Monte Carlo (MC) tow simulations were done by randomly sampling from each of the four distribution fits. The algorithm to simulate a tow section was as follows:

1. A position value is sampled from the Logistic distribution in figure 3.7 (A). This position value P_r describes the position of the AFP head/robot.

$$P_r \sim \text{Logistic}\,(\mu, s) \tag{4.1}$$

2. This was followed by the sampling of another position value from the Extreme Value distribution seen in figure 3.7 (B). This position value P_t describes the position of the tow on the roller.

$$P_t \sim \text{ExtremeValue}\,(\mu, \beta) \tag{4.2}$$

3. These two positions were added to get resultant tow position value. We now know the tow center position P_c for this simulation. The implied assumption of the independence of these positions variations arising from this additive treatment is discussed in later paragraphs with help of the results.]

$$P_c = P_r + P_t \tag{4.3}$$

4. This is followed by a tow width value sample W_a from the Normal distribution in figure 3.7 (C).

$$W_a \sim \text{Normal}(\mu, \sigma) \tag{4.4}$$

Half of this tow width value is added and subtracted from the resultant position value to get the left edge $T_{L,a}$ and the right edge $T_{R,a}$ of the tow section.

$$T_{L,a} = P_c - \frac{1}{2}W_a, \qquad T_{R,a} = P_c + \frac{1}{2}W_a \tag{4.5}$$

5. This was followed by sampling of a value of the width after compaction from the Normal distribution seen in figure 3.7 (D). It was made sure that this sample had a value greater than the value of the initial width sampled earlier. If not, resampling was done until this condition is satisfied. This condition ensured that the tow section after compaction is always wider than the tow section before compaction. Moreover, the larger width after compaction now corresponds to the larger width before compaction, and vice versa.

$$W_b \sim \text{Normal}(\mu, \sigma \mid W_b \geq W_a) \tag{4.6}$$

6. The difference between the tow width after compaction and before compaction was used to pad the simulated tow width. Thus, the left edge $T_{L,b}$ and the right edge $T_{R,b}$ of the tow section after compaction is determined.

$$\Delta W = W_b - W_a \tag{4.7}$$

$$T_{L,b} = T_{L,a} - \frac{1}{2}\Delta W, \qquad T_{R,b} = T_{R,a} + \frac{1}{2}\Delta W \tag{4.8}$$

Figure 4.1 illustrates the steps in this algorithm by using a schematic. This schematic depicts two tow sections simulated using a certain programmed shift distance. This results in a simulated gap between the two tow sections.

Thus, one tow was simulated by using information from two position related samples and two geometry related samples. The adjacent tow was also simulated using the same algorithm starting with the programmed shift of 12.5 mm for adjacent tows. Now that two adjacent tows had been simulated, the gap in this simulated instance can be determined. These simulated gaps form the yellow colored distribution seen in figure 4.2. This is the prediction about the occurrence of gaps of various magnitudes.

The gaps in the layup done during the experiment were measured by traversing an LLS over the entire 1m length of each pair of adjacently laid tow. There were 30 gaps in between 31 adjacent tows. The measured gaps form the blue distribution in figure 4.2.

The LLS made 46384 observations during these scans. Hence the two adjacent tows were also simulated an equal number of times. It can be observed from figure 4.2 that the location of the distribution from predicted gaps aligns well with the distribution of the measured gaps. This is also seen in the comparison of mean values in table 4.1. This table also gives a comparison of the spread of the two distributions using standard deviation, 90th and 99th percentile values of defect magnitude. The closeness of values describing both the location and the spread validate this prediction technique.

However, it can be observed that the density peak of the experimentally measured gap distribution is higher than that of the predicted distribution within a 0.42 mm band around the

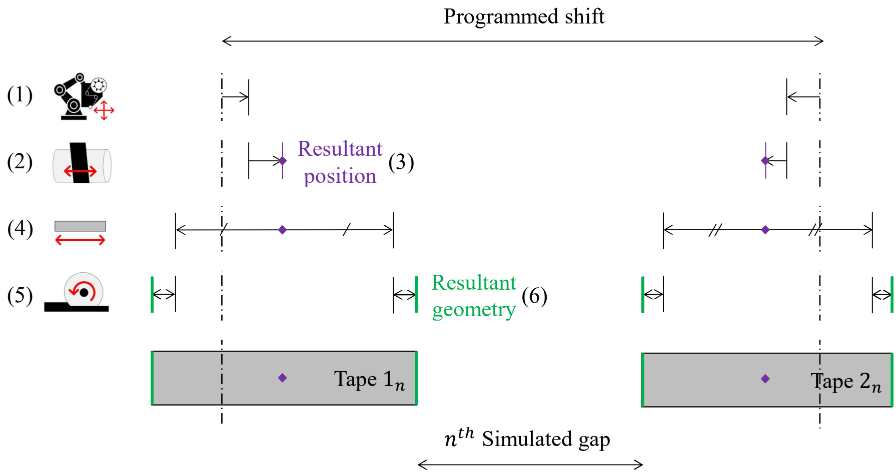

Figure 4.1: Schematic depicting the steps to simulate a tow section per the algorithm described in this section. The dot-dashed lines represent the programmed tow-to-tow distance. Each double arrow line depicts a value drawn from a distribution fit. Two simulated adjacent tows and the resulting simulated gap is shown.

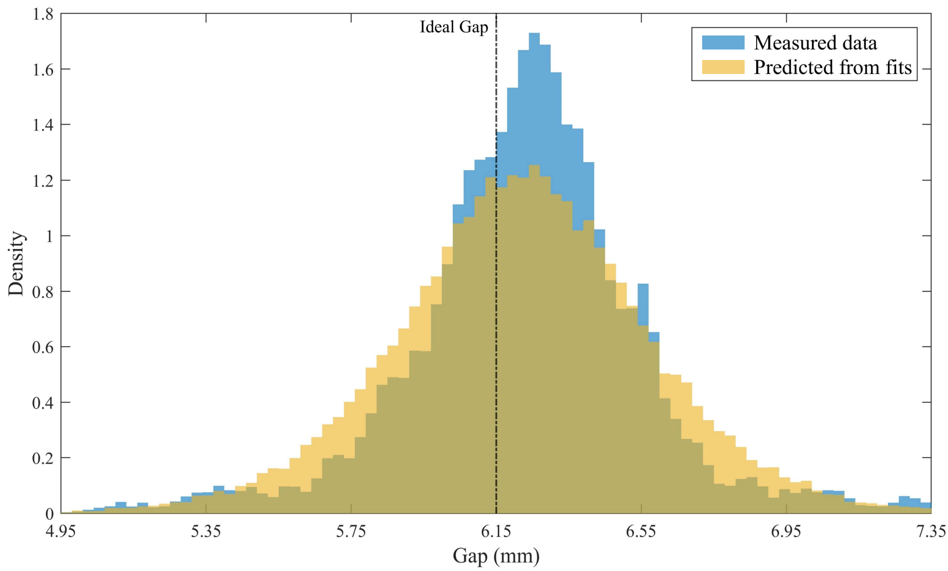

Figure 4.2: Distribution of experimentally measured gaps overlayed with the distribution of predicted gaps.

	Measured gaps	Predicted gaps	Percent difference
Mean (mm)	6.24	6.23	0.16
Standard deviation (mm)	0.33	0.36	9.09
90th percentile (mm)	6.59	6.67	1.21
99th percentile (mm)	7.21	7.13	1.11

Table 4.1: Comparison of measured gaps and predicted gaps.

programmed shift value. Correspondingly, the model underpredicts the number of gap occurrences within a band approximately 0.54 mm wide on either side of the distribution peak. This discrepancy may be attributed to possible cross-correlations between the four sources of manufacturing variation, which are treated as statistically independent in the present simulation framework. For example, when a robot path deviation takes place, it may not move the tow with it. Thus the tow lateral movement will be recorded in addition to the robot inaccuracy, even when the tow is being appropriately laid. The simulation methods ignore these potential interactions and assumes the four sources are independent.

Additionally, it is challenging to check for cross-correlations in the obtained experimental data. The datastreams from the four sensors needed synchronization in time and in tow length due to the different locations of the measurement points of the sensors in reference to the tool center point (TCP). Furthermore, unrecorded experimental events like a removed twisted tow and tow jams make it difficult to confidently synchronise their interactions. With due regard to these limitations, no cross-correlations could be detected. However, digitalization efforts are ongoing to improve the quality of the acquired data. Since the experimental data consisted of 30 gaps between 31 tows, the gaps on either side of one tow will have some correlation as well. This correlation is not captured in the simulations depicted in the figure 4.1 but will be captured in the tow resolved techniques shown in section 4.2

Since the simulations are informed by data obtained from a single trial experiment, this approach may nevertheless be feasible for reducing the experimental effort required to determine allowable defect magnitudes and frequencies.

Similar simulations can be carried out for various values of the programmed gap between those adjacent tows. The probability of a gap or overlap can be computed as the area under the predicted probability density function on the corresponding side of the relevant threshold. Figure 4.3 shows the predictions for the probability of gap and overlap defects occurring for various values of programmed gaps. It is thus possible to balance the competing effects of programmed gap values and take informed decisions regarding them.

Figure 4.4 gives an example of how the probability of defects can be related to the contribution of the various sources of variations. Each of the thinner blue curves shows the trends in probability of a gap greater than 0.5 mm, if variations from one of the four sources are eliminated one at a time in the simulations. This elimination in the simulation was done by simply setting nil or nominal values of the eliminated variation while retaining all other variations as-is. This approach can help in the prioritizing of various process improvement efforts aimed at lowering the variations.

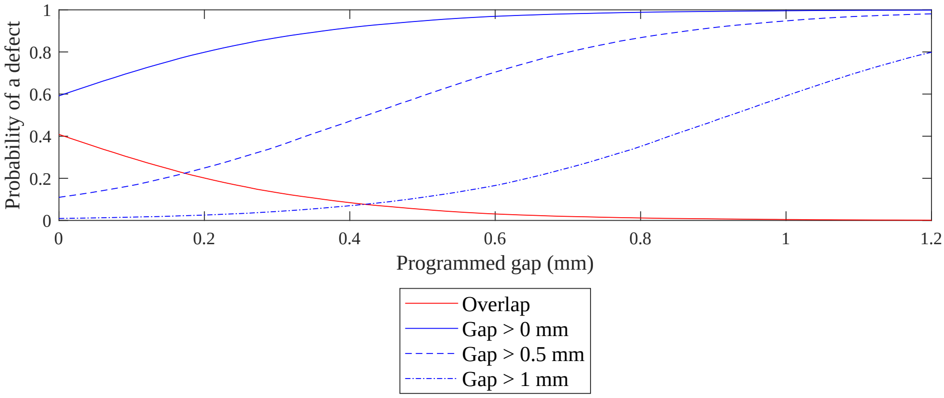

Figure 4.3: Probability predictions of defects for various values of programmed gap between adjacent tows.

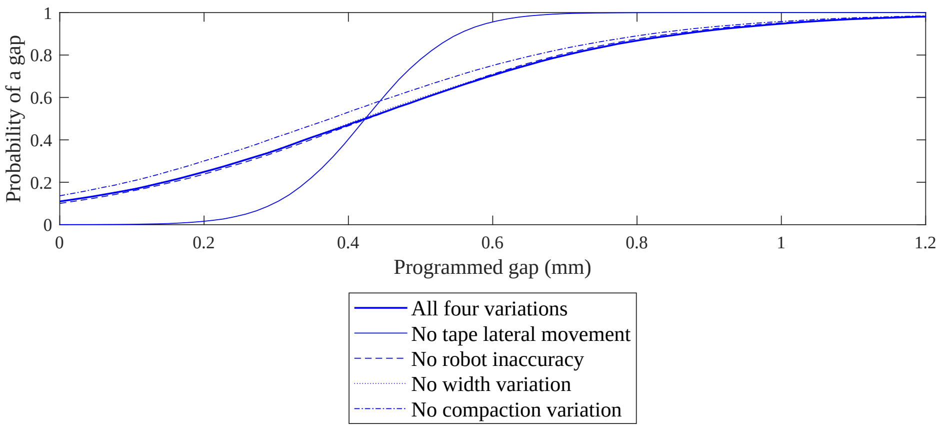

Figure 4.4: Probability predictions of a gap (greater than 0.5 mm) when variations from each of the four sources of variations are eliminated one at a time.

Note that the probabilities mentioned earlier are that of finding a defect at a certain location of a layup. To convert these probabilities to a representative example defect maps in a virtual layup, the next section describes dependent sampling methods along with a scheme which considers the distance between two instances of the sectional simulation in the layup direction.

4.2. Tow-resolved mesoscale level defect predictions

A representation of a tow can be created by assembling various sectional profiles of the tow to form a geometry which represents the entire length of the tow. A tow representation with sectional profiles can be seen in the schematic of figure 4.5. The interpolation between any two consecutive tow profiles will be linear in this thesis. This interpolation is a reasonable

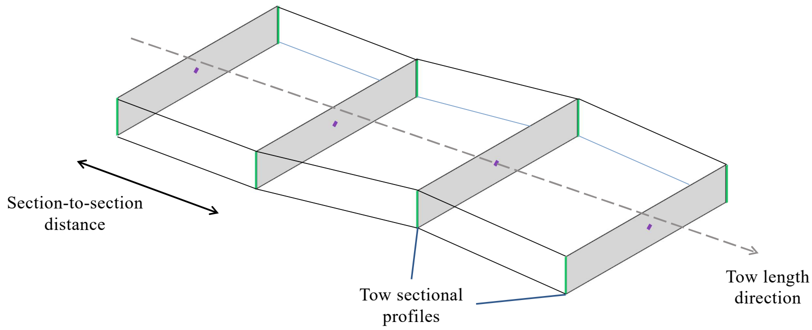

Figure 4.5: Schematic showing the assembly of a representative tow from individual sectional profiles.

assumption if the consecutive profiles are close to each other in the tow length directions. Both the experimental and simulated tows representations in this study have been created with the lengthwise separation between profiles being less than 3 mm. This study focuses on the profile geometry in the width direction since those lead to the formation of gap and overlap defects.

The profile of the tow can be created from information about the tow position and the tow geometry. The tow position determines the tow center line. The tow geometry determines the edges of the tow relative to the tow center. In this section, the profile of the tow is simulated by sampling values related to the tow position and the tow geometry. This is followed by an assembly/stitching of the tow profiles in the tow length directions to create the simulated tow as shown in figure 4.5.

This section will compare two methods of creating synthetic tows. The first method uses Monte Carlo simulations based on random sampling which was described in section 4.2. To overcome the shortcomings of this method, the second method uses Markov Chain Monte Carlo simulations with a sampling scheme based on the Random Walk Metropolis algorithm.

4.2.1. Tow simulation based on random sampling

Monte Carlo (MC) simulations of the tow section were used to create a synthetic tow. The algorithm to simulate a tow section followed the steps as described in section 4.1. The only difference was the use of improved distribution fits in the statistical characterization of the four measured sources of variation - robot inaccuracy, tow lateral movement on the roller, tow width before compaction and tow width after compaction. These improved fits were obtained by evaluating the mean squared error for a broader class of candidate distributions and selecting the distributions that best matched the experimental data.

Figure 4.6 shows these experimentally measured variations in blue color. Robot inaccuracy and tow width before compaction have been fit with Logistic distributions while tow width after compaction has been fit with a Normal distribution. Tow lateral movement on the roller was fit with a Skew Normal distribution. Figure 4.6 also shows these fits in yellow. The parameters to these distribution fits are listed in table 4.2.

All the sampling steps in this algorithm were randomly implemented. The simulated tow was

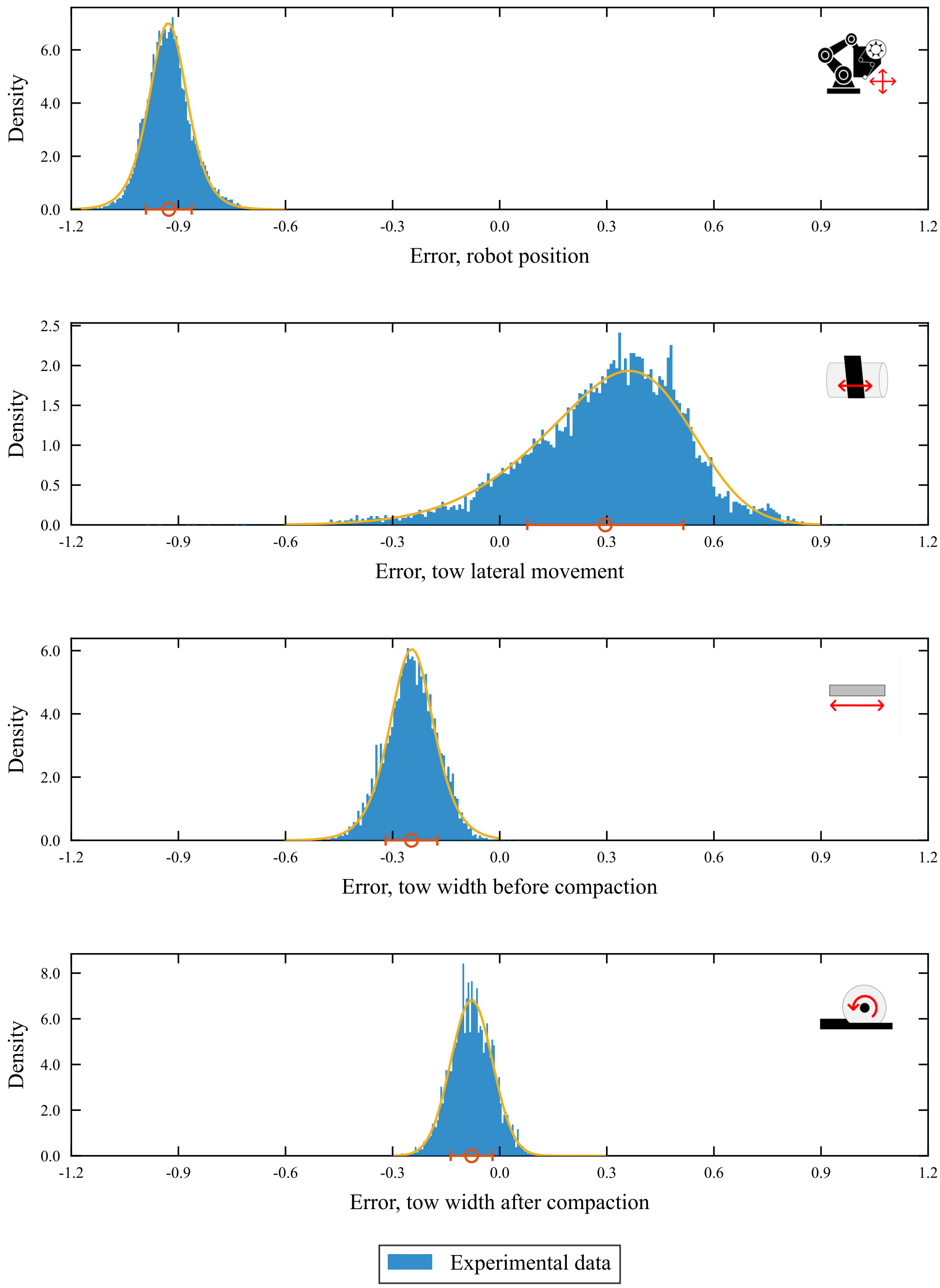

Figure 4.6: A, B, C, D (top to bottom). Measured manufacturing variations are shown in blue. Means and $\pm 1\sigma$ values are annotated in red. Distribution fits are annotated in yellow.

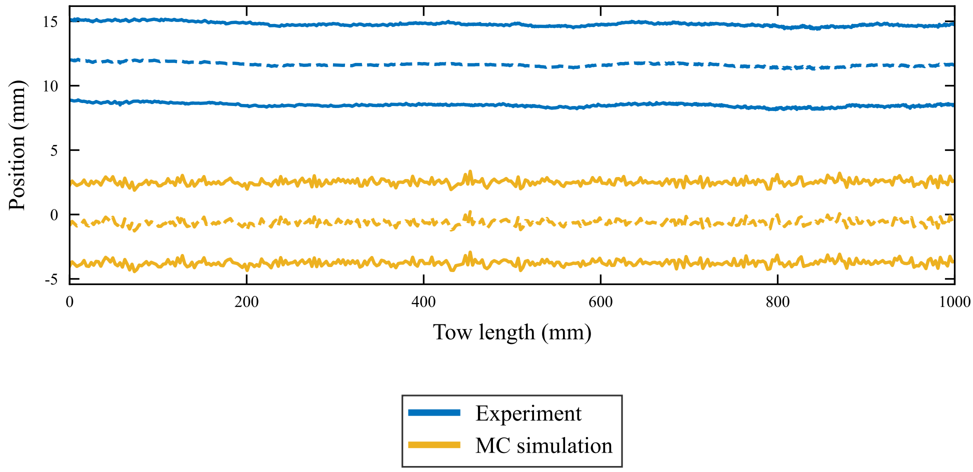

Figure 4.7: Examples of experimentally measured tow (blue) along with synthetic tows simulated using the MC method (yellow).

assembled by placing consecutive tow sections a fixed distance apart. This tow section to tow section distance was chosen as 2.65 mm. This value was based on the lowest frequency rate of the four data streams in the experimental dataset.

An example simulated tow made by this MC method of random sampling and assembly can be seen in figure 4.7 in yellow. One can observe that it is much more wavy than the experimentally recorded tow seen in blue. This difference between the real tow and the simulated tow can be explained by the nature of the chosen sampling technique. The four experimental distributions for the four sources of variations - robot inaccuracy, tow lateral movement on the roller, tow width before compaction and tow width after compaction - are based on physical aspects of the material and the AFP layup process. When being recorded the values of these variations are changing continuously. However, in the tow section simulation algorithm, these values are sampled randomly. This leads to an assembled tow where the tow position and geometry jump values and lose continuity which is seen in the real tow edges and centerlines.

	Robot inaccuracy	Tow lateral movement	Tow width variation	Tow width variation after compaction
Fit Type	Logistic	Skew Normal	Logistic	Normal
Location	$\mu = -0.93$	$\xi = 0.53$	$\mu = -0.25$	$\mu = -0.079$
Scale	$s = 0.036$	$\omega = 0.29$	$s = 0.041$	$\sigma = 0.058$
Shape	–	$\alpha = -2.29$	–	–

Table 4.2: Summary of fits to distributions of measured manufacturing variations.

4.2.2. Tow simulation based on the Random Walk Metropolis algorithm

In the earlier section, it was observed that the simulated tow showed significantly greater waviness then the real tow because of the discontinuous jumps in the randomly sampled values of position variation and geometry variation. This shortcoming has been overcome by using a sampling technique which bases current draws on the neighborhood of the past draw. This dependency on the past sampled value results in a sequence of values that forms a Markov chain.

This section details the implementation of a Markov Chain Monte Carlo simulation to create synthetic tows by using the Random Walk Metropolis algorithm (RWM) [111]. The discontinuity in the consecutively sampled position and geometry values for the tow section creation can be addressed by using the RWM sampling scheme which accounts for the past sampled value. This is because consecutive samples are more likely to be close to each other due to continuous variation of various aspects of the physical process.

The steps to create the tow section were similar to the steps described in section 4.1 except that they simulated tow section width from samples of the tow width variation after compaction only. Tow width variation before compaction was neglected due to the inability to capture the width increase in the random walk chains. Thus, the simulation was implemented in the following steps with sampling for each source of variation except the width variation before compaction.

1. The target distribution $p(x)$ is the fit to experimental data described in figure 4.6. This target distribution is defined with θ_n which represents the various fitted parameters. The consecutively drawn samples need to eventually converge to these distributions.

$$p(x) = f(x \mid \theta_n) \tag{4.9}$$

   The target distribution is Logistic for robot inaccuracy, Skew Normal for tow lateral movement and Normal for tow width after compaction. The parameters θ_n to these target distributions are listed in table 4.2. These target distributions are seen in figure 4.6 in yellow.

2. The algorithm involves proposing a new value x^* when the current value is x_0. This proposal x^* is a sample from the symmetrical proposal distribution. This proposal distribution was selected to be a Gaussian distribution centered at the current value. Thus the proposed value will be given by

$$x^* \sim \mathcal{N}(x_0, \sigma^2) \tag{4.10}$$

   The value for standard deviation σ of the Gaussian proposal distribution is chosen by calculating the standard deviation of the difference between consecutive values of the experimental data for the respective source of variation.

3. The acceptance ratio is calculated as

$$\alpha = \min\left(1, \frac{p(x^*)}{p(x_0)}\right) \tag{4.11}$$

   where $p(x^*)$ and $p(x_0)$ are the values of the probability density function of the target distribution for the proposed value and the current value of the Markov chain.

4. The proposed new value x^* is accepted or rejected according to an acceptance rule. The acceptance rule is based on the comparison of α with a random sample from a uniform distribution of numbers between 0 and 1.

$$x_1 = \begin{cases} x^*, & \text{if } U \leq \alpha, \quad U \sim \mathcal{U}(0,1) \\ x_0, & \text{otherwise.} \end{cases} \tag{4.12}$$

5. The above proposals along with acceptances/rejections are implemented iteratively to achieve a chain of samples $\{x_n\}$ whose stationary distribution corresponds to the target probability density of the relevant source of variation.

The starting point for the Markov chain is selected randomly from the experimentally measured range of the source of variation. A burn-in or converging period is minimal in this implementation because the starting point is within the range of the target distribution. New proposed values in the chain are a small random step. This random step is equally likely to be higher or lower than the current value because the proposal Gaussian distribution is symmetric with its mean at the current value. The standard deviation σ affects how much away is the proposed value from the current value. Thus it decides the neighborhood in which the chain will move. This prevents unrealistic value jumps as seen in the Monte Carlo simulations described in section 4.2.1.

The acceptance rule accepts movement of the chain towards more probable values while accepting moves towards less probable values with the probability of α. As a result, moves towards significantly lower density regions are rarely accepted while moves towards moderately lower density are accepted relatively frequently. The chain spends time in various regions in a way which is proportional to the target density. Over time it converges to the target distribution.

The distribution of the RWM samples for the respective sources of variation are annotated in green in figure 4.8. They correspond well to the respective target probability densities annotated in yellow. Table 4.3 gives the comparison of the mean and spreads of the distributions formed by the samples of the simulated Markov chains to those measured experimentally. The close agreements in these statistics signify good convergence of the random walk simulation.

The consecutive tow sections are simulated using these RWM samples and assembled into

		Robot inaccuracy	Tow lateral movement	Tow width variation	Tow width variation after compaction
Experiment	Mean (mm)	-0.93	0.30	-0.25	-0.08
	Standard deviation (mm)	0.06	0.22	0.07	0.06
Random Walk algorithm	Mean (mm)	-0.93	0.29	-0.25	-0.08
	Standard deviation (mm)	0.06	0.22	0.07	0.06

Table 4.3: Comparison of the distributions of the four sources of variations derived from the model and the experimental layup

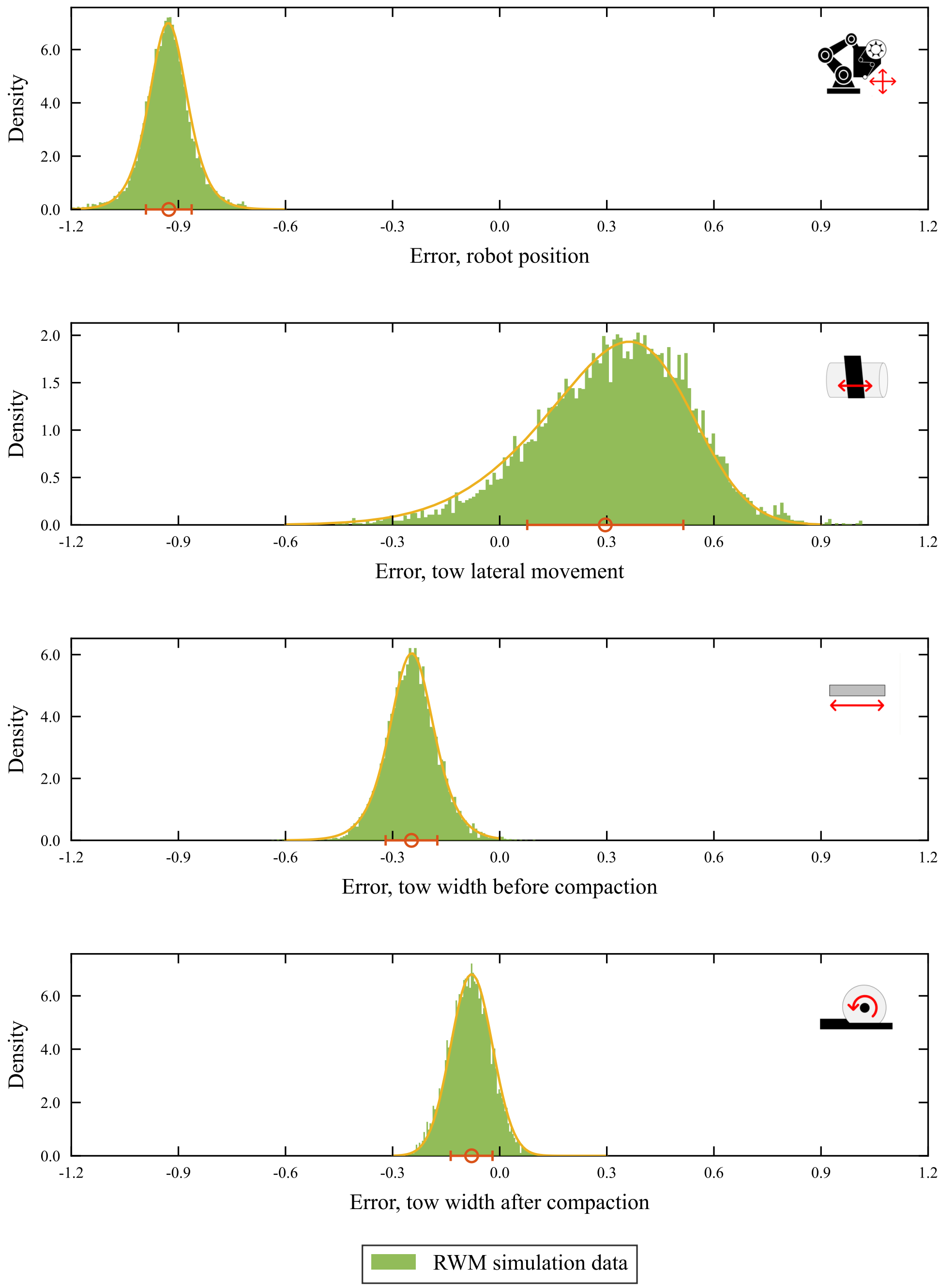

Figure 4.8: A, B, C, D (top to bottom). Fits to the target distributions are annotated in yellow. Means and $\pm 1\sigma$ values are annotated in red. Distributions from the Markov Chain Monte Carlo simulation are shown in green.

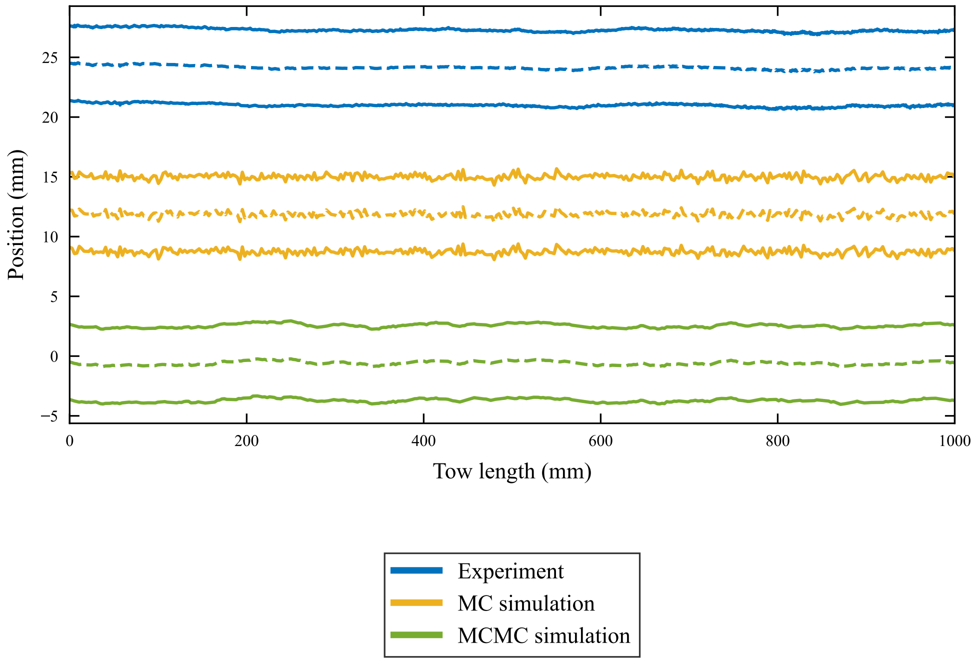

Figure 4.9: Examples of experimentally measured tow (blue) along with synthetic tows simulated using MCMC method (green) and using MC method (yellow).

a tow representation which has its position and geometry varying realistically. An example simulated tow made by this MCMC method is seen in figure 4.9. The lines in this MCMC simulated tow (green) oscillate with much lower frequency and look much more similar to the physical tows from an AFP layup (blue) compared to the example simulated tow made by the MC method (yellow). These similarities will be quantified in section 4.3. Potential framework extension avenues to further improve these similarities are discussed below.

In the MC method, the samples were random and independent. Hence the tow simulation could ensure that width after compaction is greater than the width before compaction. New values were sampled until this condition was met. The MCMC method leads to a chain of variation values which are dependent on the past values. Therefore, the section simulations can occur when the value of the chain of width variations and width variations after compaction are such that the condition of width after compaction being greater than width before compaction is not met. If the width before compaction had not been neglected, the simulated tow would show a non-physical width decrease in 3.9% of the sections. This shows the need for an advanced version of this Random Walk sampling which samples simultaneously from the width variation distribution and the width variation after compaction distribution while enforcing that the two chains are strictly kept away from directions which lead to the non-physical tow width decrease.

Additionally, future extensions could allow for the standard deviation σ values used in equation 4.10 to scale at various spatial resolutions along the length of the tow. This could improve the prediction accuracy by eliminating the spatial dilation effects in the length direction originating in the difference of the various spatial resolutions. This could potentially explain the very small wavelength fluctuations seen in the experimental tow but not in the MCMC tow in figure 4.9.

Also, while the virtual laminae in this study can be stacked up to create a laminate, it neglects the out-of-plane waviness of the tow laid on a defect. Future work can investigate simple out-of-plane waviness shape descriptors and rules to capture how these defects stack up over multiple laminae.

4.3. Validation

Figure 4.9 visually compares examples of an experimentally measured tow, an MC simulated tow and an MCMC simulated tow. The MCMC simulated tow looks more representative of the experimentally measured tow than the MC simulated tow. This visual similarity needs to be validated with quantitative and qualitative metrics to ensure that the virtual laminate with synthetic tows has a similar number and size of defects as those which would be seen in a real AFP laminate with physical tows.

For the purpose of validation, the simulated tow needs to be compared with an experimental tow to examine if it is equivalent in terms of the variations seen in the tow position and tow geometry. By extension, this equivalency would also mean that the magnitude and frequency of the gaps and overlaps will be comparable. Thus, the validation is performed at two levels, once by comparing experimental tow with the synthetic tow and then by comparing the defect characteristics in an experimental lamina with a virtual lamina.

4.3.1. Tow level comparison

The edges of the simulated tow are observed to have spatial waviness over a range of length scales. The resulting centerline of this simulated tow consequently has some spatial waviness characteristics. This can be compared to the spatial waviness characteristics of the centerline of the experimentally measured tow. Such comparisons can be achieved using a Fast Fourier Transform (FFT) on the spatial signal of the tow centerlines, yielding spatial-frequency amplitude spectra. These spectra describe how the magnitude of centerline variation is spread across spatial frequencies thus providing insight into the spatial correlation of the experimental and simulated tow centerlines. The spectral comparisons can be made using physical interpretations of metrics like spectral magnitude which reflects how large the tow centerline deviations are in amplitude and the dominant spatial frequencies which reflects the distances over which the tow waves along its length.

To compare the centerlines of the MC simulated tows, MCMC simulated tows and the experimental tows an FFT analysis was done over the spatial domain of each 1 m length of these tows. The spatial signals were interpolated onto a uniform spatial grid prior to spectral analysis to satisfy FFT sampling requirements. Figure 4.10 shows representative examples of spatial-frequency amplitude spectra of the centerline variations of an MC simulated tow, an MCMC simulated tow and an experimental tow. The figure 4.10 (a) shows that in all cases, the spectra are dominated by low spatial frequencies, indicating that the tows primarily exhibits long-wavelength undulations. The Y axis of the figure was truncated to aid clarity of the lower amplitude regions. The MCMC tow spectrum exhibits good agreement with the

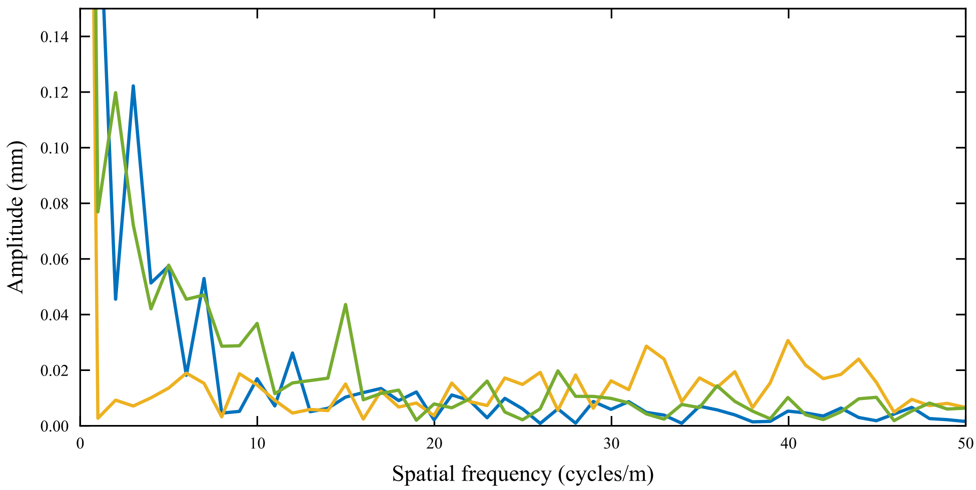

(a)

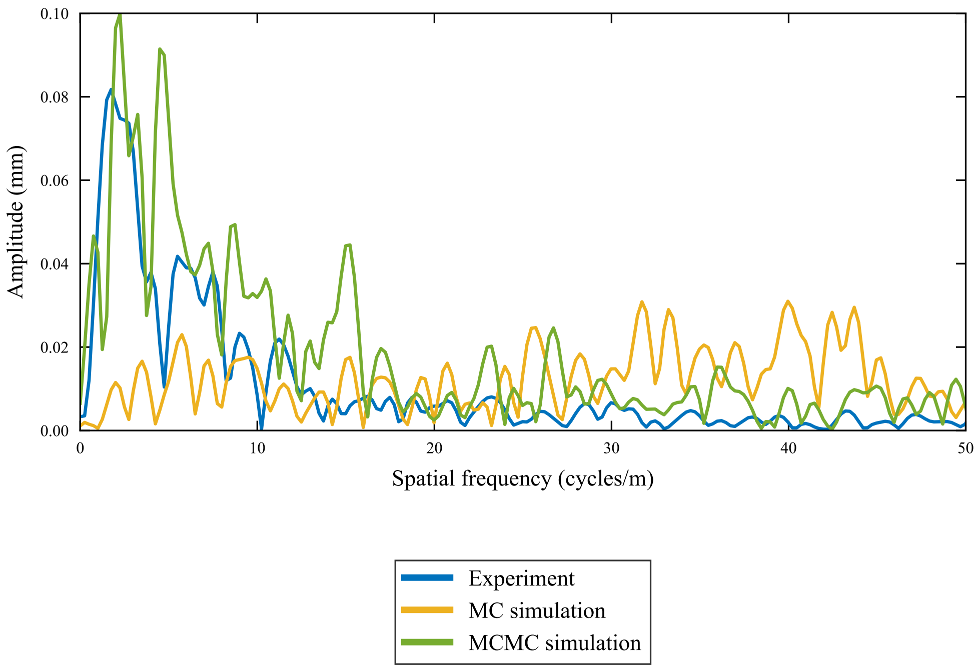

(b)

Figure 4.10: FFT analysis of tow centerlines of an example simulated tow and an experimental tow. The top figure (a) shows the resulting spectra for FFT of the tow centerlines without any additional processing. The bottom figure (b) shows the resulting spectra for FFT of the tow centerlines after processing steps like detrending, windowing and padding.

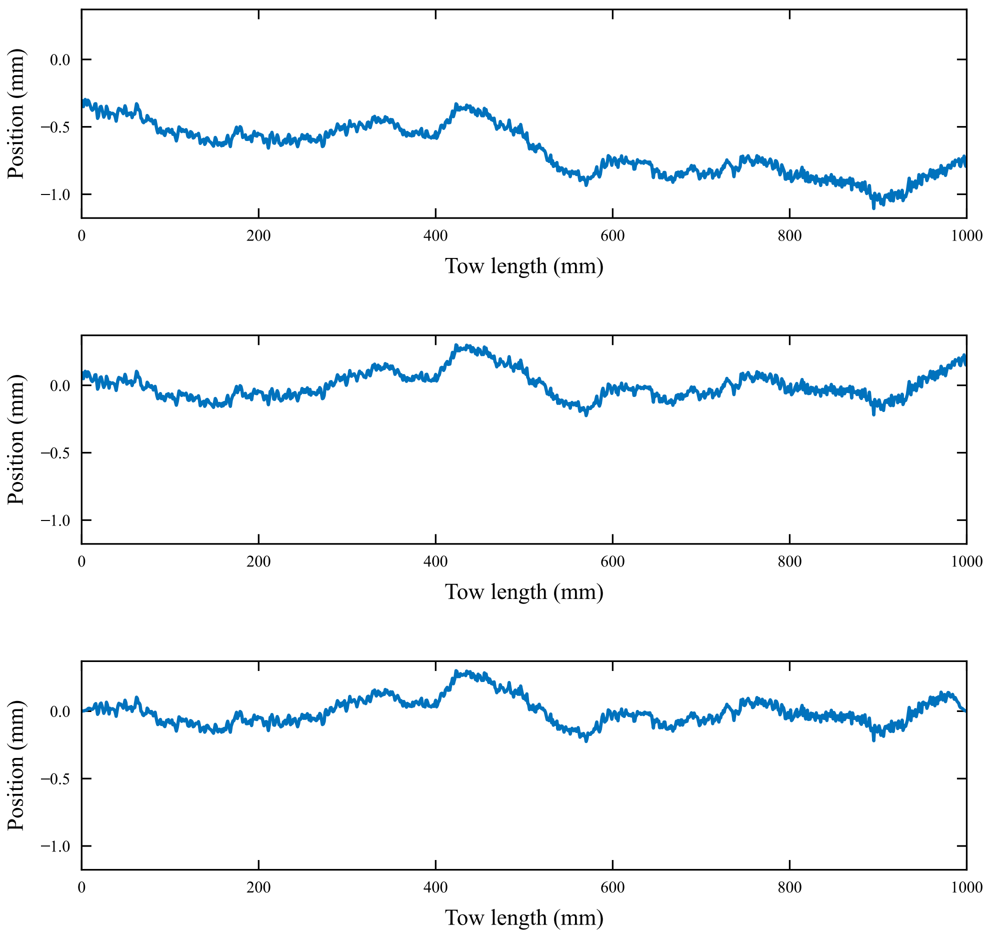

Figure 4.11: A, B, C (top to bottom). Signal processing steps applied to an example experimentally measured tow centerline prior to spatial frequency analysis. (A) Raw signal, (B) detrended signal, and (C) detrended signal with a Tukey window applied.

experimental tow spectrum in both amplitude and decay behavior across the low-frequency and mid-frequency ranges, whereas the MC tow spectrum significantly underpredicts low frequency content. At higher spatial frequencies, all spectra converge toward a low-amplitude experimental noise level.

The long-wavelength offset components of the tow centerlines reflect the global waviness behavior during AFP layup and represent relevant, physically meaningful features of the tow geometry. However, they dominate the raw FFT magnitude and could obscure shorter wavelength features. To examine shorter wavelength features in greater detail, standard preprocessing steps including linear detrending, windowing, and zero-padding were applied, resulting in the spectra seen in figure 4.10 (b). The linear detrending removed the offset component and average slope of the centerline. The windowing introduced minimal end-tapering to reduce spectral leakage from discontinuities at the start and the end of the signal. These discontinu-

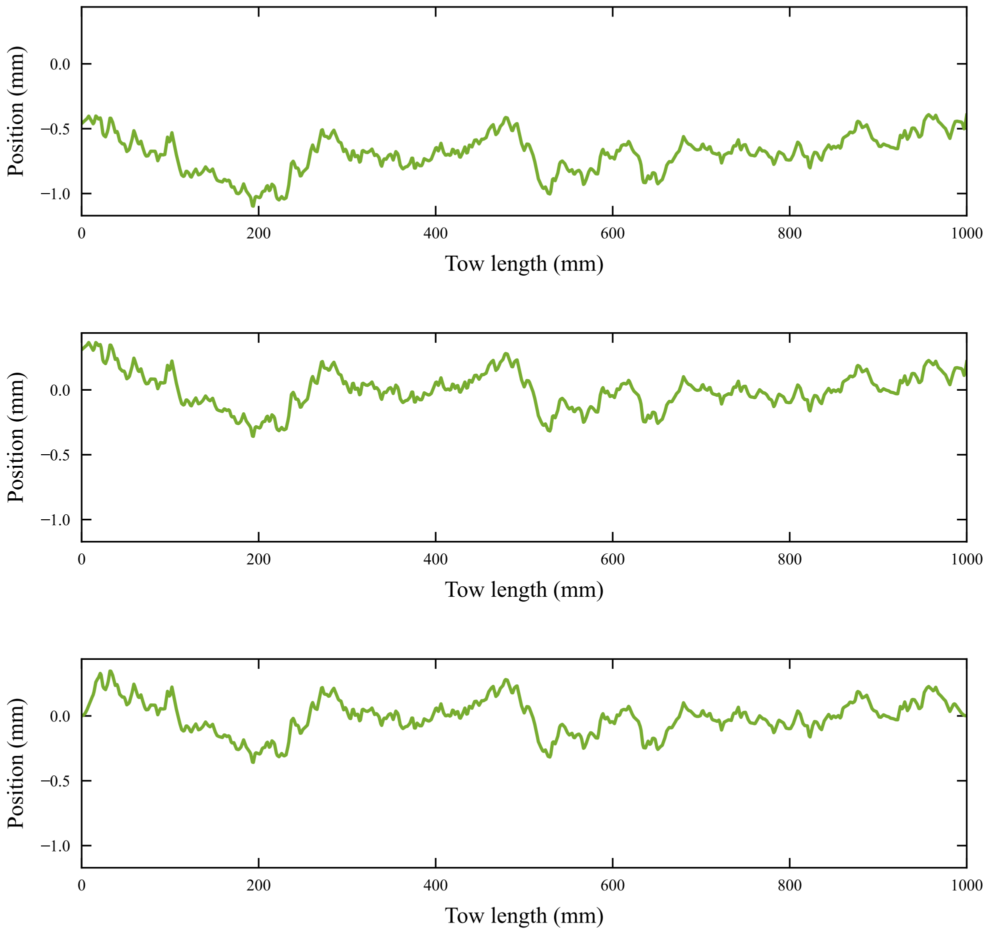

Figure 4.12: A, B, C (top to bottom). Signal processing steps applied to an example of an MCMC simulated tow centerline prior to spatial frequency analysis. (A) Raw signal, (B) detrended signal, and (C) detrended signal with a Tukey window applied.

ities exist because the tow start and end positions can be at non-zero values. Figure 4.11 and figure 4.12 show the effects of these signal preprocessing steps on an example of the centerline of an experimental and an MCMC simulated tow. The signals were then zero-padded prior to FFT evaluation to provide finer frequency binning for visualization and comparison. The spectra in figure 4.10 (b) also show similar spectral shape and comparable spectral magnitude between MCMC simulation and experimental tow. The MC simulated tow displays broadband amplitudes across the frequency range, showing weak spatial correlation with the experimental tow.

Quantitatively, the average Pearson spectral correlation coefficient for the MCMC simulated tows was $\rho = 0.752$, indicating good agreement in spectral shape with the experimental tow. For the MC simulated tows it was $\rho = -0.027$, indicating negligible correlation. The average dominant spatial frequency was 2.1 cycles/m for the experimental tows, 2.7 cycles/m for the

		Mean (mm)	Standard deviation (mm)	90th percentile (mm)	99th percentile (mm)
Measured gaps		6.24	0.34	6.59	7.25
Predicted gaps	MC simulation	6.22	0.32	6.64	6.99
	MCMC simulation	6.22	0.32	6.62	7.04

Table 4.4: Comparison of the distribution of predicted gaps for the MC and MCMC method with the distribution of experimentally measured gaps.

MCMC tows and 133.3 cycles/m for the MC tows. The MCMC tows match closely to the long-wavelength regime observed experimentally while the MC tows show much higher and noisier dominant frequencies.

All together, these qualitative and quantitative comparisons demonstrate that the MCMC method more effectively reproduces the spatial correlation structure, dominant frequencies, and overall magnitude of experimental tow waviness than the MC approach.

4.3.2. Lamina level comparison

Several simulated tows can be assembled with the appropriate offsets to create a virtual lamina. Figure 4.15 shows an example virtual lamina constructed using the MCMC method. It shows the resulting gaps and overlaps in white and dark grey respectively. These resulting defects depend on the waviness of the tow edges and on the offsets i.e. how far apart they are laid adjacently.

The programmed shift for the simulated virtual lamina was set to one tow width i.e. 6.35 mm, whereas the experimental layup had a programmed shift of 12.5 mm. For comparison purposes, the experimental data were normalized to an equivalent programmed shift of one tow width. This normalization was achieved by translating the measured tow geometries in the width direction to adjust the tow-to-tow offsets.

A virtual lamina of 31 tows was constructed to compare it to the similarly laid experimental lamina with an equal number of tows to compare the occurrence of gaps. Figure 4.13 shows the distribution of experimentally measured gaps in blue. The gaps from the MCMC virtual lamina are depicted in green while the gaps from the MC virtual lamina are depicted in yellow. The gaps from the virtual lamina created using the MCMC method quantitatively match more closely to the experimentally measured gaps than the gaps from the MC method. The location of the gap distributions align well for both the models. The experimental distribution and simulated distributions of gaps are summarized in table 4.4.

Another comparison between the two simulation methods is done by measuring the defect area. The percentage area of gap and overlaps in the normalized experimental layup was calculated to be 2.73% and 1.28%. A virtual lamina with an equal number of tows was generated numerous times using both MCMC and MC methods and the average percentage of gaps and overlaps was calculated. Both the methods show good correlation and are summarized in table 4.5.

The comparison of model performance using the distribution of defects or the defect area percentage in the earlier paragraphs lacked information on the continuity of gaps. The distribution

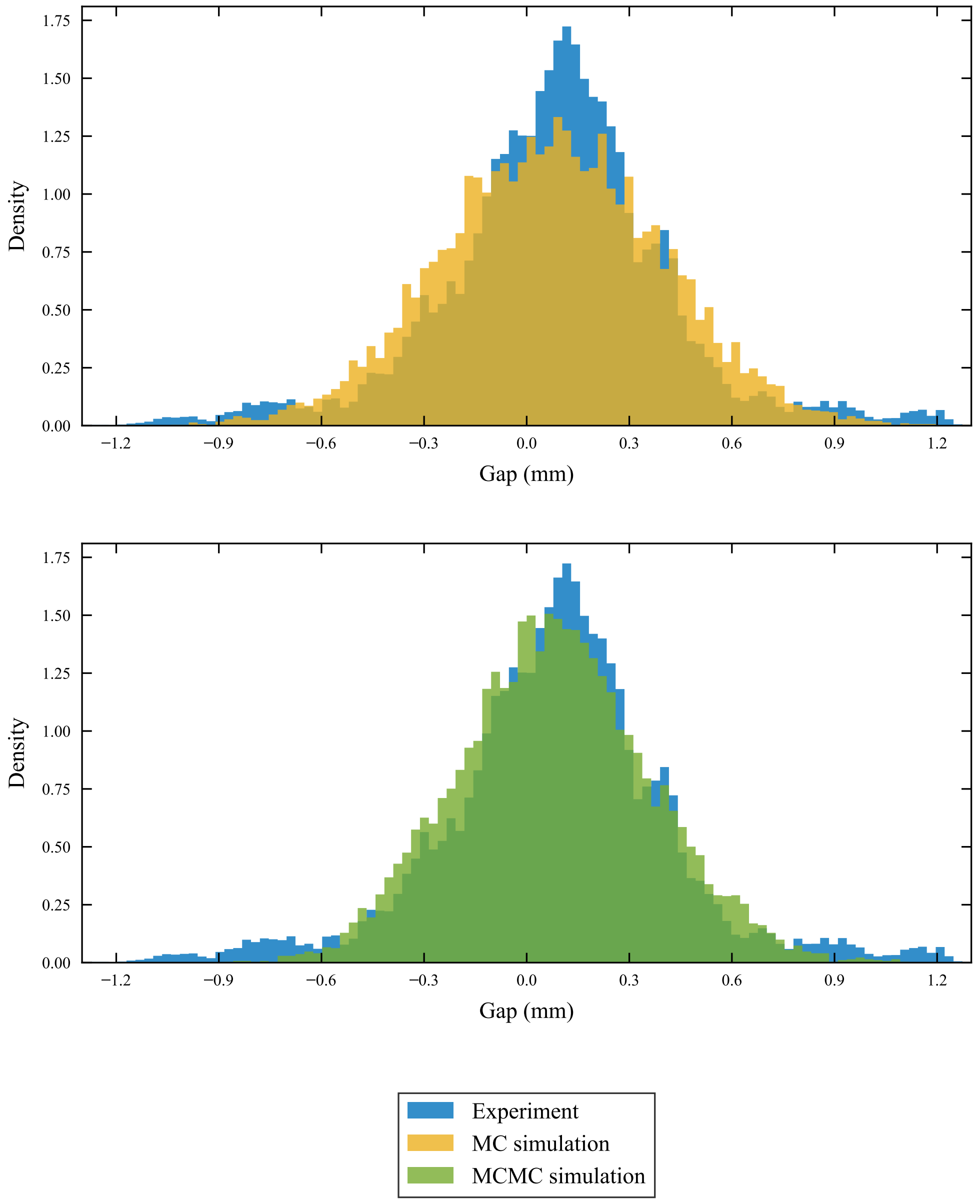

Figure 4.13: A, B (top, bottom). Comparison of predicted gaps and experimentally measured gaps. Gaps predicted using MC simulations are shown in yellow. Gaps predicted using MCMC simulations are shown in green. Experimentally measured gaps are shown in blue.

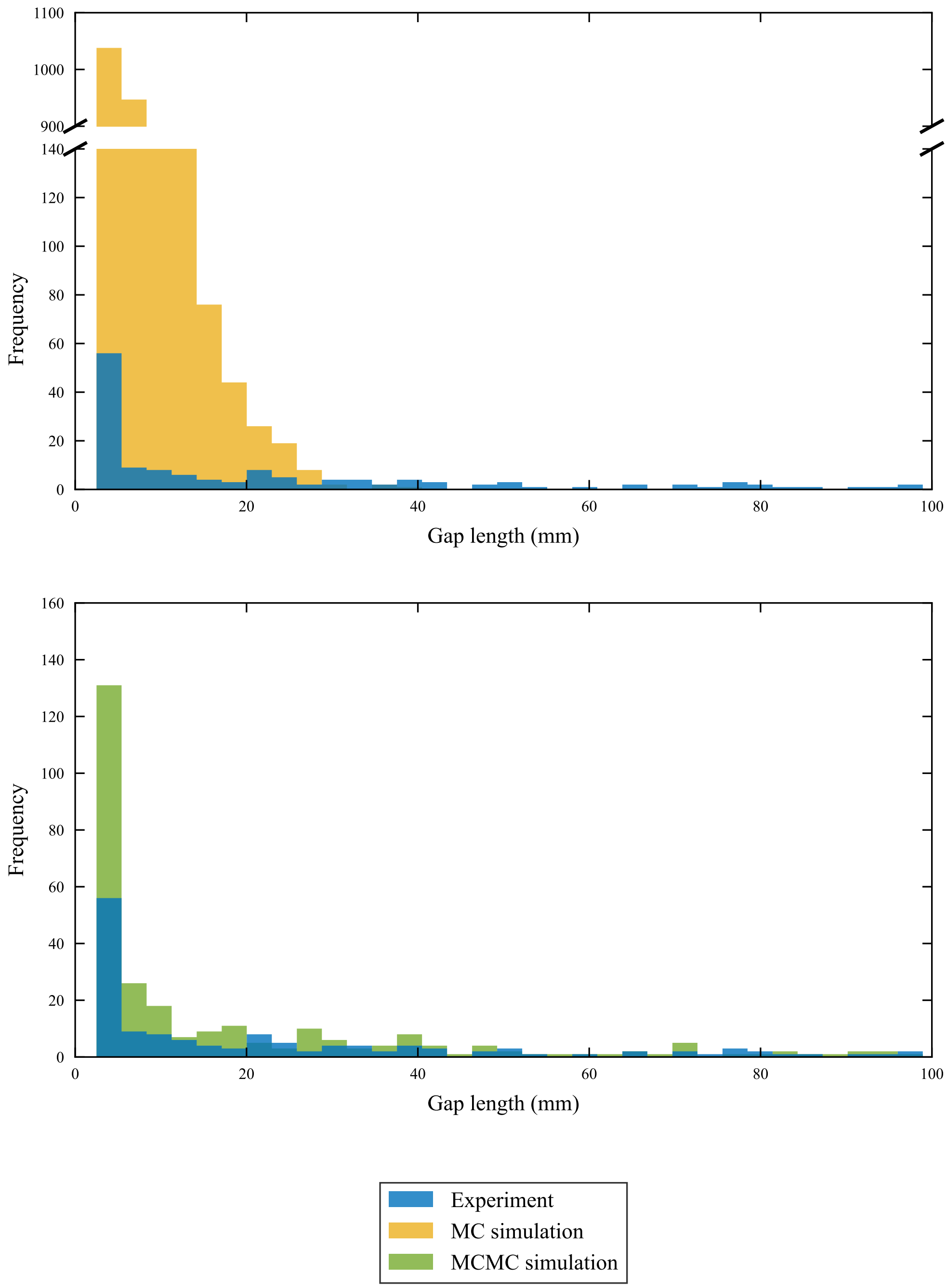

Figure 4.14: Comparison of the distributions of length of defects between the experimental lamina and the simulated lamina.

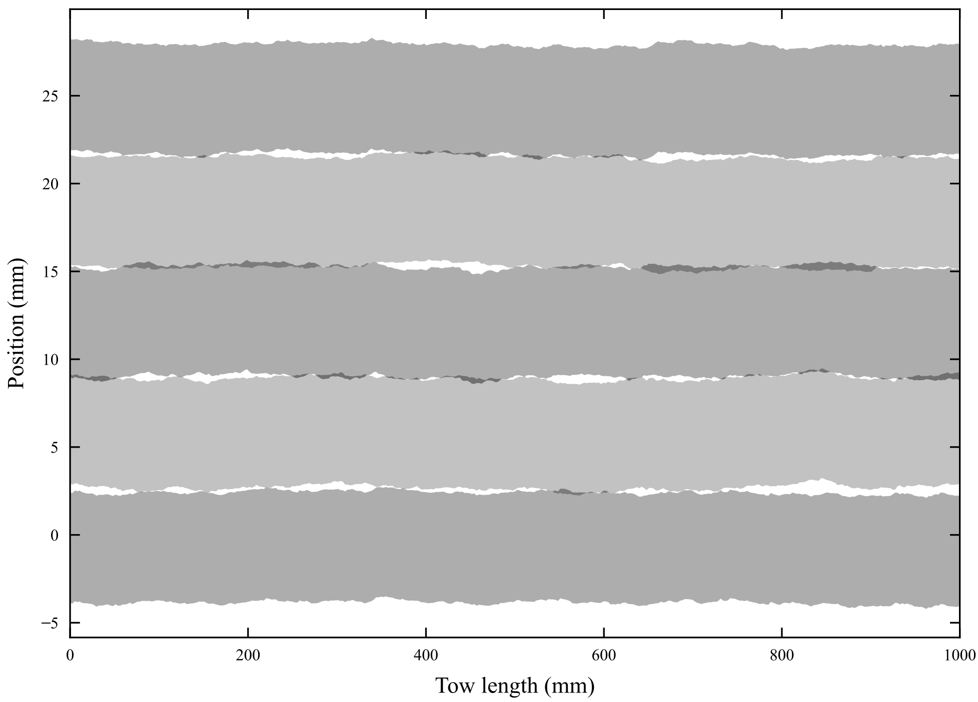

Figure 4.15: Example virtual lamina simulated using the MCMC method.

		Gaps % area	Overlaps % area
Experimental layup		2.73	1.28
Virtual lamina	MC simulation	2.60	1.48
	MCMC simulation	2.77	1.58

Table 4.5: Comparison of predicted gap and overlap defect area for the MC and MCMC method with experimentally measured gap and overlap defect area.

or the percentage area of defects do not have a one-to-one conversion to the length of the defects. Thus it is essential to compare the lengths of the defects formed in the virtual lamina and the experimental lamina as seen in figure 4.14. It can be observed that the MC method overestimates the number of smaller gaps and also completely misses the higher gap lengths. The MCMC method estimate of the length of defects is much more closely correlated to the experimentally measured lamina.

To summarize, the various comparisons between the two methods of simulation and the experimental data have shown that the defect distribution or area can be acceptably predicted by both the MC and MCMC simulation methods. However, the MCMC method simulates tows and laminae which are representative in not just the defect frequency and defect magnitude but also in the length of defects found in real laminae. The neighborhood sampling used in the MCMC method leads to position and geometry samples which vary continuously, similar to the physical phenomenon they are based on. Owing to this sampling method where each sample is informed by the past sample, the MCMC method can be used to simulate tows and construct virtual laminae which are similar to real layups.

4.4. Geometry description for AFP modeling

AFP manufacturing can involve layups with thermoset prepreg tow, thermoplastic tow, or dry fiber tow, all of which lead to gap and/or overlap defects. These defects are expected to evolve during subsequent manufacturing steps, which may include autoclave processing, oven heating, vacuum-bag-only (VBO) processing, or resin infusion. During these steps, defect geometry influences consolidation mechanisms such as air and void evacuation, matrix percolation, and squeeze flow. In the final manufactured laminate, gaps and overlaps can negatively affect structural performance depending on their severity and location.

Investigations into both the manufacturing process behavior and the structural response of AFP composites therefore require accurate geometric descriptions of the layup, including information about the size, frequency, and spatial distribution of gap and overlap defects. All process and structural modeling efforts related to AFP defects begin with such geometric descriptions. Thus, realistic representations of the layup geometry are a prerequisite for predictive modeling of AFP composites.

At present, cross-sectional microscopy and X-ray micro-computed tomography (micro-CT) scans are commonly used to obtain geometric information about AFP layups. Cross-sectional microscopy is destructive and provides information only at discrete sections, requiring assumptions about defect evolution away from the observed plane. X-ray micro-CT scanning is constrained by limitations in specimen size, resolution, scanning time, and cost, and is therefore not always practical for large or industrially representative AFP parts. Moreover, both approaches are destructive and resource-intensive.

As a result, process and structural modeling efforts can benefit from alternative methods for generating accurate geometric layup descriptions. Gap and overlap defects arising from manufacturing process variations cannot be fully predicted prior to layup. To the best of the author's knowledge, existing AFP tow models rely on deterministic geometry descriptions. The methods presented in this work enable the creation of defect-equivalent mesoscale representations of AFP layups based on measured manufacturing variations. The results presented here focus on single-lamina geometry in the width direction and therefore neglect interactions between adjacent laminae. Future work can extend this framework by introducing simplified geometric descriptors to capture tow waviness through the thickness and its influence on neighboring laminae.

4.5. Utility for AFP technology and process design

In addition to the uses mentioned in the introduction, simulated tows and the resulting virtual lamina can also give insights for AFP technology and process improvements.

4.5.1. Optimal programmed shift

The programmed shift or (interband) offset is the distance between planned paths of adjacent tows or courses of an AFP layup. This programmed shift between adjacent tows needs to be minimized to reduce gaps. This is because gaps are associated with structural performance knockdowns. However, decreasing the programmed shift has the effect of increasing the probability of overlap defects. Overlap defects during the layup need repair and rework thus slowing the process and leading to higher manufacturing costs. Thus the programmed shift is a tradeoff between the mechanical knockdowns from gaps defects and the additional manufacturing process cost due to overlap defects.

The MCMC method was used to simulate laminae with various values of the programmed shift. This resulted in the values of gap and overlap defect areas for a range of programmed shift values as plotted in figure 4.16 in red and blue. It shows the increase in gap area percentage as the programmed shift increases and the increase in overlap area percentage as the programmed shift decreases. The optimal programmed shift at which the total defect area is minimized is 6.27 mm. This plot can be modified to weigh the gap and overlap curves with associated costs. The gap curve can be weighted for mechanical knockdown costs while the overlap curve can be weighted for process cost with rework. Optimization of the weighted defect curves would yield an optimal programmed shift. Thus, the developed simulation methods could be useful for a tradeoff analysis between gaps and overlaps. The simulation could be used for programmed shift value selection before qualification and thus can help reduce expensive prototype iterations. These simulations can also be informed by the gap size threshold for getting "erased" in the post-processing steps.

The stochasticity in each simulation leads to slight variation in the defect area percentage of each simulated lamina. The simulations were run 100 times for each value of the programmed shift to find the statistical variation in the gap and overlap defect area. The bounds of this variation are annotated in figure 4.16 as light blue and light red color bands. Thus, these MCMC simulations statistically relate AFP process parameters to defect population characteristics and

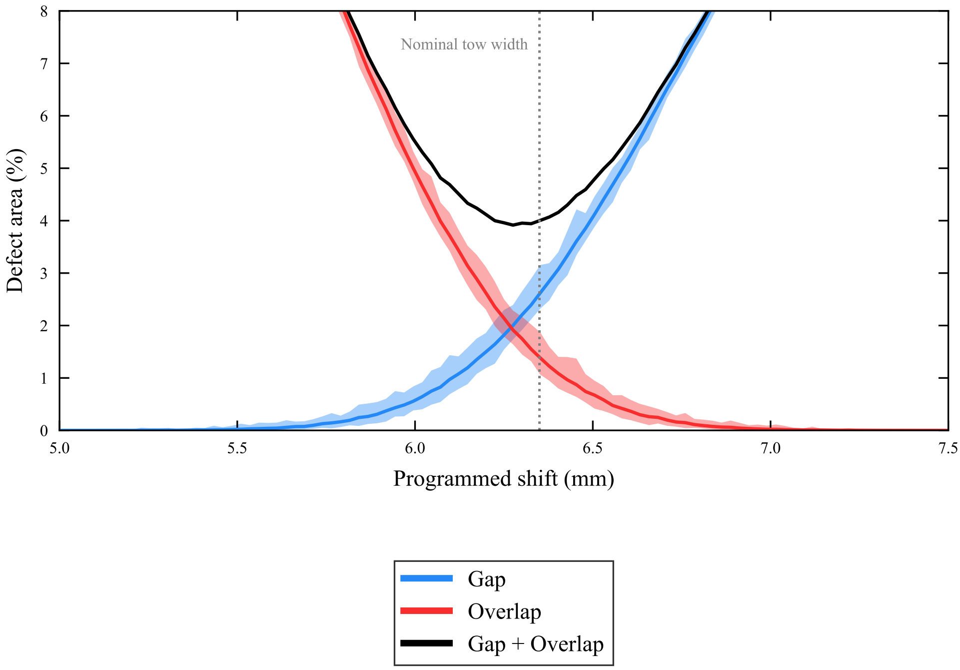

Figure 4.16: Illustration of optimal programmed shift for minimizing defect area percentage. The variation bands show the stochasticity of the defect population obtained by performing multiple simulations for each value of the programmed shift.

scatter.

This information can be useful for certification activities such as establishing manufacturing allowables by providing statistically grounded estimates of defect magnitude, lengths and frequency. Rather than relying on highly conservative worst-case assumptions, allowable limits can be informed by the predicted defect populations and their variability. This enables manufacturing process designs that are less conservative while remaining compliant, particularly in structurally critical regions where stacking effects and defect accumulation are a concern.

4.5.2. Prioritizing AFP process improvements using uncertainty propagation

There are various technological ways to reduce the manufacturing process variations in AFP layups. The robot accuracy can be improved by installing secondary feedback loops or newer robot models with higher path accuracy. The AFP feed system can be improved to reduce the tow lateral movement. The replacement schedules of worn rollers can also play a role. The tow material dimensional specification can be made tighter. Each of these process improvements entails different costs. Thus knowing the effectiveness of these measures in laminate quality will be useful in prioritizing these measures for layup quality improvements.

Figure 4.17 shows the gap and overlaps area percentages in laminae when eliminating the

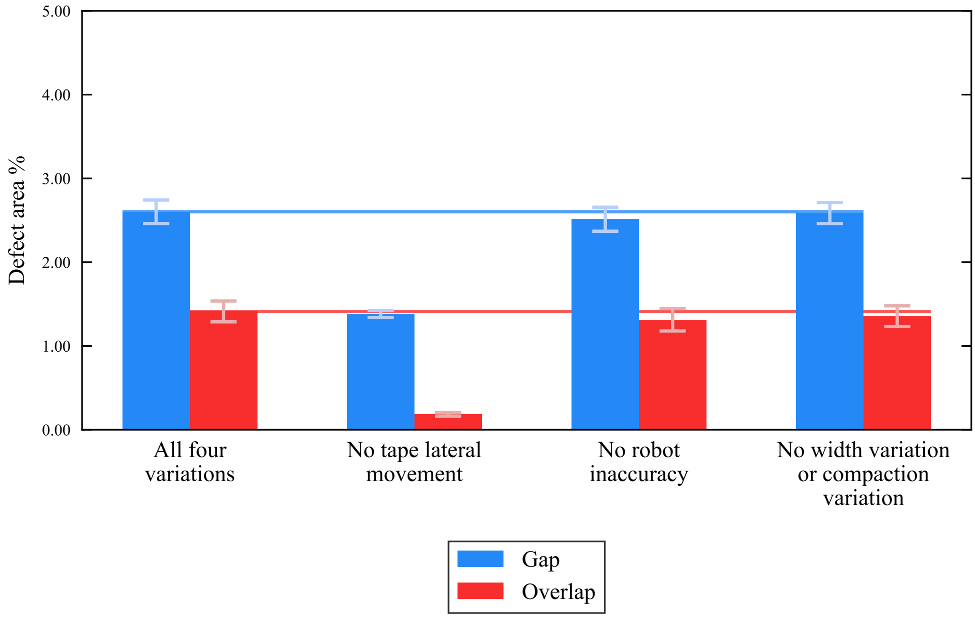

Figure 4.17: Defect area percentage when variations from the various sources of variations are eliminated one at a time.

various sources of variations one at a time. This figure was created by simulating laminae a 100 times for each elimination. For our AFP head, material system and process conditions, the gap defect percentage will be reduced by 47%, 4% and 1% when tape lateral movement, robot inaccuracy and width variations are eliminated, respectively. In this case, eliminating position variations of the tow lateral movement will lead to a higher improvement in laminate defects than eliminating geometry variations of the tow width.

Figure 4.17 resulted from running the simulations with stochastic inputs based on the fits to the four measured sources of variations in our experiment. But more generic simulations can be executed to understand the behavior of this statistical framework which describes the AFP process. For these generic simulations, the four stochastic inputs were represented using normal distributions. Normal distributions were selected because they are widely used parametric descriptions of manufacturing variability. Moreover, the focus is on the propagation behavior of framework rather than the input variation characteristics. The mean and standard deviation were chosen to be 0 mm and 0.1 mm respectively for the baseline simulation. Input variations were individually perturbed to higher values and were then compared with the baseline simulation to understand their effects on the defect population. The higher values for the mean and standard deviation were chosen to be 0.5 mm and 0.15 mm respectively. The various mean and standard deviation values were chosen to be comparable to the experimentally observed values. The changes in mean would represent a process bias such as average tow width being offset from the specified width, or tow lateral movement which is biased to one side of the

No.	Input variations	Output distributions		Comments
		μ (mm)	σ (mm)	
1	All four inputs with $\mu = 0$ and $\sigma = 0.1$	0.0003	0.2123	Baseline simulation
2	Higher μ for one PV	0.0005	0.2121	Negligible effect
3	Higher σ for one PV	-0.0012	0.2656	25% increase in defect spread
4	Higher σ for both PVs	0.0001	0.3058	44% increase in defect spread
5	Higher μ for one GV	-0.5002	0.2113	Shift in defect mean toward overlap region
6	Higher μ for both GVs	-0.5819	0.2083	Shift in defect mean toward overlap region*
7	Higher σ for one GV	0.0015	0.2271	7% increase in defect spread
8	Higher μ and σ for PVs and GVs	-0.6230	0.3121	Combined worst case scenario*

Table 4.6: Propagation of input distribution perturbations through the MCMC simulation to the resulting defect distribution. The increased input values of μ and σ were 0.5 mm and 0.15 mm, respectively, compared with baseline values of 0 mm and 0.1 mm. Stochastic noise is present in the reported values. PV = position variation; GV = geometry variation; * = obtained using MC simulation.

roller center due to reasons like roller wear and bearing misalignment. The changes in standard deviations represent the control on the spread of the geometry or position variables such as tape slitting width changes or robotic path variation in various sections of the workspace. The results of the generic simulations for various uncertainty scenarios are briefly summarized in table 4.6. They have been compared to the resulting defect distribution from the baseline simulation which had a mean of 0 mm and a standard deviation of 0.21 mm.

It was found that changing the mean of any of the position variations had negligible effect on the defect magnitude distributions. This was due to the collective shifting of all the tows rather than relative to each other. However, increasing the standard deviation of one or both positional variations to 0.15 mm increased the output standard deviation by 25% and 44%, respectively, relative to the baseline. Thus, the spread in the position variations is not an additive effect. The two position variations interact and propagate non-linearly.

When the mean of the geometry variation from the width after compaction was increased to a value of 0.5 mm, this caused many more overlaps than gaps, thus shifting the mean of the defect magnitude distribution to -0.5 mm. When both the geometry variations had an increased mean value of 0.5 mm, the shifting of the mean of the defect magnitude distribution towards the overlap direction was greater at -0.58 mm. Thus, the combined effect was not additive. When the standard deviation of the geometry variation from the width after compaction was increased to 0.15 mm, the standard deviation of the defect magnitude distribution increased slightly by 7%. A minor further increase was seen in the standard deviation of the defect magnitude distribution when the standard deviation of both the geometry variations was increased.

If the mean and the standard deviations were increased for all the variations, representing a hypothetical worst case scenario, the standard deviation of the defect magnitude distribution increased by 50%. Overall, position variations primarily broadened the defect distributions while a systemic bias in geometry variations mainly shifts the mean of the defect distributions

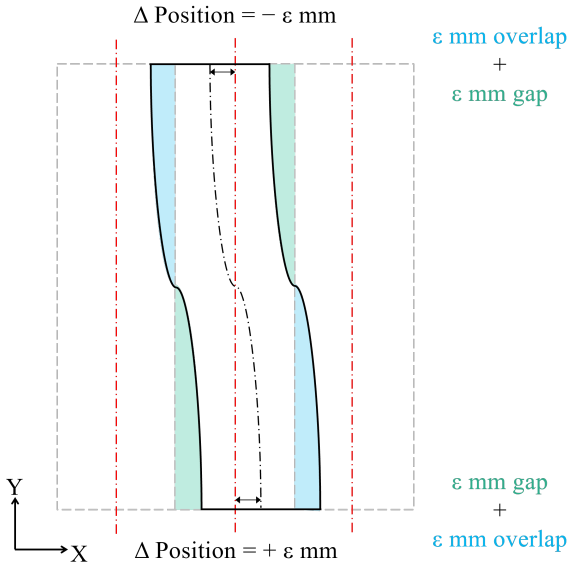

(a)

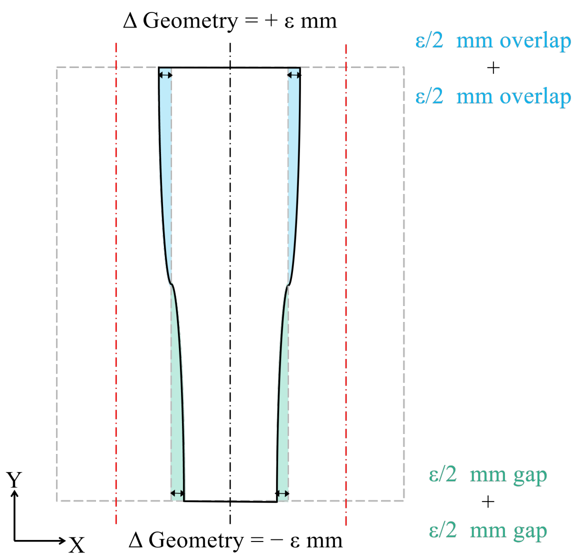

(b)

Figure 4.18: Comparison of the effect of position variations (a) and geometry variations (b) in an AFP tow on the formation of gaps and overlap defects.

in opposite directions of the bias.

Thus, this framework can be used to implement an uncertainty propagation study to provide such quantitative and qualitative insight about how the individual inputs propagate via the AFP manufacturing process to affect the defect population characteristics.

Another effect captured by the simulation framework is the relative effects of position variations and geometry variations in the formation of gap and overlap defects on either side of the tow. This relative significance of position variations and geometry variations is illustrated in figure 4.18. This figure compares the effect of position variations and geometry variations of the same magnitude. In figure 4.18 (a), the position variation changes in magnitude from $+\varepsilon$ to $-\varepsilon$, while in figure 4.18 (b), the geometry variation changes in magnitude from $+\varepsilon$ to $-\varepsilon$. Both figures show the formation of gaps and overlaps due to these variations. The position variation leads to a gap of magnitude ε and an overlap of magnitude ε, whereas the geometry variation leads to a gap of magnitude $\varepsilon/2$ and an overlap of magnitude $\varepsilon/2$. Thus, variations of the same magnitude produce substantially greater edge waviness when arising from position variations rather than geometry variations.

5

Tow lateral movement at the compaction roller during AFP steering

तदेजति तन्नैजति
तद्दूरे तद्वन्तिके ।

— ईशोपनिषद् ५

It moves, and yet it does not move;
it is far, and it is near.

— *Īśā Upaniṣad* 5

This chapter is based on the following publications:

- *Tow lateral movement at the compaction roller during Automated Fiber Placement composite layup under steering conditions.* Manuscript under review.
- *Tape at the compaction roller while steering: Does it move laterally?* Presented at the 6th International Symposium on Automated Composites Manufacturing (ACM6, 2024), Columbia, South Carolina, USA.

Lateral movement of the tow at the compaction roller is a dominant source of manufacturing process variation which causes incorrect tow position. While chapter 3 established this for straight line layups, this phenomenon has not been investigated under steering conditions. Studying the mechanism of formation of gaps and overlaps in VSLs would provide an insight about their causes and would help formulate strategies to mitigate them. Moreover, the characterization of this variation could also inform statistical predictions such as those developed in chapter 4. The objective of this chapter was to measure tow lateral movement under various steering conditions and to predict it. The chapter begins with an experimental characterization of the tow lateral movement while steering at various steering radii. This is followed by an interpretation of the observed behavior through an analytical framework. Finally, the implications of this analytical framework towards improved steered AFP layups are discussed.

5.1. Background and motivation

The tow feeding system of an AFP setup moves tow from the spool to the compaction roller using a system of pulleys and chutes. During the start of each course, tow is extended below the roller before the AFP head approaches the tool and presses against it to start laying. The cantilever extended tow may not remain straight due to self-weight and residual stresses. This can start the tow at a position shifted sideways from its intended position at the center of the compaction roller. The tow is under tension due to the spool brake as it goes under the compaction roller during layup. This tow tension acts against the lateral movement of the tow. Reduced tension on the tow during some phases of the layup translates to a higher possibility for lateral movement. After the cutoff, the tow loses tension followed by an exit of the tow chute. These conditions combined with the lateral bending stiffness of the tow can lead to lateral movements of the tow.

The experimental results described in figure 3.7 revealed the relative significance of the sources of manufacturing variations in the AFP process. The tow lateral movement was the largest contributor to gaps and overlaps with a range of 1.041 mm. This is 16.4% of the 6.35 mm width of the tow. These values are from an experiment involving tow layup in a straight line [112]. The tow lateral movement which contributes most to the formation of these defects during AFP manufacturing of composite parts has not been investigated under steering conditions.

Past work suggests that this tow lateral movement phenomenon may worsen under steering conditions. Legenstien et al. and Füssel et al. studied the strain behavior of highly aligned discontinuous fiber thermoplastic tow during steering and also recorded the presence of a drift/inaccuracy [99, 100]. Rajan et al. conducted a finite element analysis of the tow under the compaction roller in steering conditions and found shear forces on the tow due to traction from the roller [58]. These forces have a radial component which may cause the tow to move on the roller in the radially outward direction.

The focus of most AFP steering studies mentioned in section 2.4 has been on wrinkling defects. The effect of steering on gap and overlap defects during the layup of continuous unidirectional tow materials has not been studied. The mechanism leading to placement inaccuracy of such tow material in steering conditions has not been investigated.

5.2. Experimental methodology

An experiment was designed to measure the tow lateral movement at the compaction roller during an AFP layup under steering conditions. These experiments were performed using an

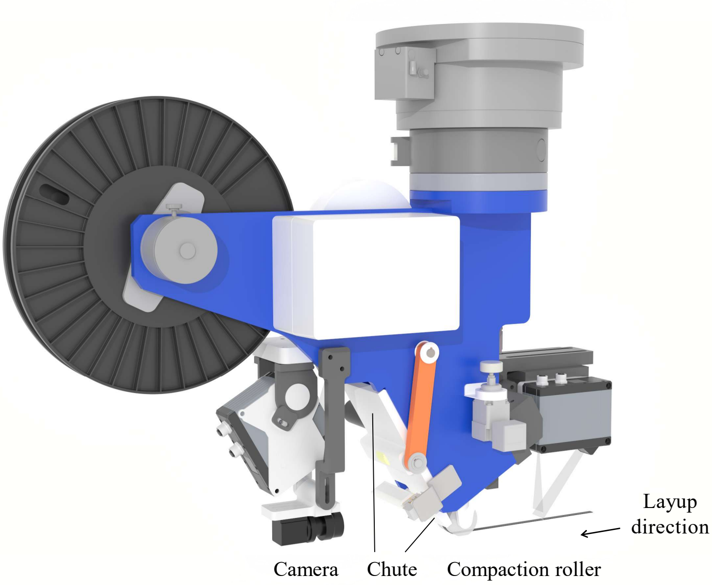

Figure 5.1: CAD model showing various sensors setup on the AFP head.

AFP machine in the robotic cell located at SAM XL (Smart Advanced Manufacturing XL). Since this experiment is similar to the experiment described in chapter 3, some details have been omitted.

5.2.1. Experimental setup overview

The measurement system consists of a camera mounted on an AFP head as illustrated in figure 5.1. The AFP-XS head made by ADD Composites is the end effector on a KUKA KR 210 R2700 robot manipulator. AFP-XS has a silicone compaction roller with a width of 31 mm and a diameter of 40 mm. The roller has a Shore hardness of 45A. It has an infrared heater that increases the tack of the thermoset tow during layup [102].

The camera - Ximea xiC USB 3.1 Gen1 MC050MG-SY-UB - views the tow position as it goes under the compaction roller. The data stream from the camera gives insight into the tow position variation during layup. The mount geometry was designed to rigidly hold the camera while allowing it to be moved and set in relation to the tow it is observing. Data from the camera is acquired via a high-speed USB cable routed from the manipulator arm.

5.2.2. Layup procedure

The experiment involved laying down two different unidirectional carbon fiber thermoset composite tow materials. The two materials will be referred to as material 1 and material 2 for confidentiality reasons. Material 1 was thinner and less tacky while material 2 was thicker and tackier. Their respective properties are presented later in subsection 5.4.1.

Layup was done on a flat substrate while recording tow position on the compaction roller

Radii	No. of runs	
	Material 1 (Lower thickness, tackiness)	Material 2 (Higher thickness, tackiness)
1000 mm	2	2
1200 mm	2	3
1400 mm	3	2
1600 mm	3	3
1800 mm	2	2
2000 mm	3	3

Table 5.1: Layup summary

using the above-mentioned camera. The substrate consisted of a flat plate tool layup area which was covered with thermoset tow. Figure 5.2 (top) shows the layup taking place on the substrate. The tool was a 1.5 m by 1 m rectangular steel plate which was clamp mounted on a measurement table. The 300 W IR heater was used at 80% power during the layup. The compaction force was measured to be 377 N.

The curvilinear layups were programmed with steering radii varying from 1000 mm to 2000 mm in increments of 200 mm. 3 tows were laid for each value of the steering radius. 18 tows were laid for each material while steering. Each of the 36 runs was 1 m long. The maximum speed was set at 50 mm/s. The robot accelerated after the starting runway phase and decelerated for the stop at tow cutoff. It accelerated again at the end of the layup. Figure 5.2 (bottom) shows an example of the velocity profile of the layup measured during one of the laydowns. Data was not available for three of the runs due to data acquisition system issues. Data from another three runs was discarded due to tow twists. Table 5.1 gives the summary of the runs for which data was acquired.

5.2.3. Data acquisition and analysis

The 5-megapixel monochrome optical camera was paired with a lens that provides manual control on the focal length [105]. The Ximea CamTool application was used to control and operate the camera. The metadata from the application was used to get the timestamp for each frame.

The exposure time of the camera was set at 1 ms such that it captures an image that shows the black tow against the white roller with sufficient contrast for the chosen heater power setting.

The tow position on the compaction roller was measured using image processing on each recorded frame. Figure 5.3 shows a red window of size 1500 pixels by 50 pixels. This is the region of the frame where the image is the sharpest. The center of the roller is annotated with a white dashed line. Each frame is cropped to the window size and the average intensity of each column of pixels is calculated. The black tow has a much lower intensity than the white roller. Thus, the edge of the tow with respect to the dashed center line is calculated by detecting this change in average intensity.

This value in pixels is converted to a metric measurement by using a pixel-to-mm length conversion scale. This scale is obtained from a reference image which has a checkerboard scale

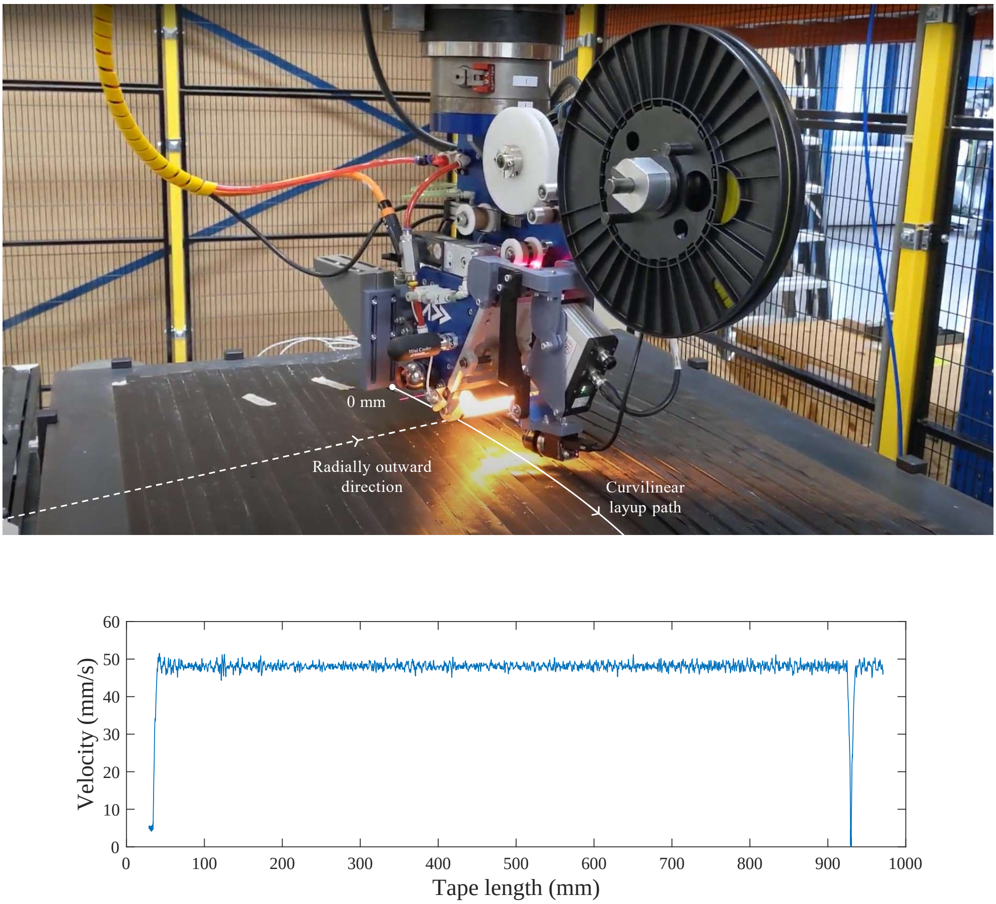

Figure 5.2: Material 2 being laid with a steering radius of 1400 mm. The planned circular layup path is annotated (top). AFP layup velocity profile (bottom).

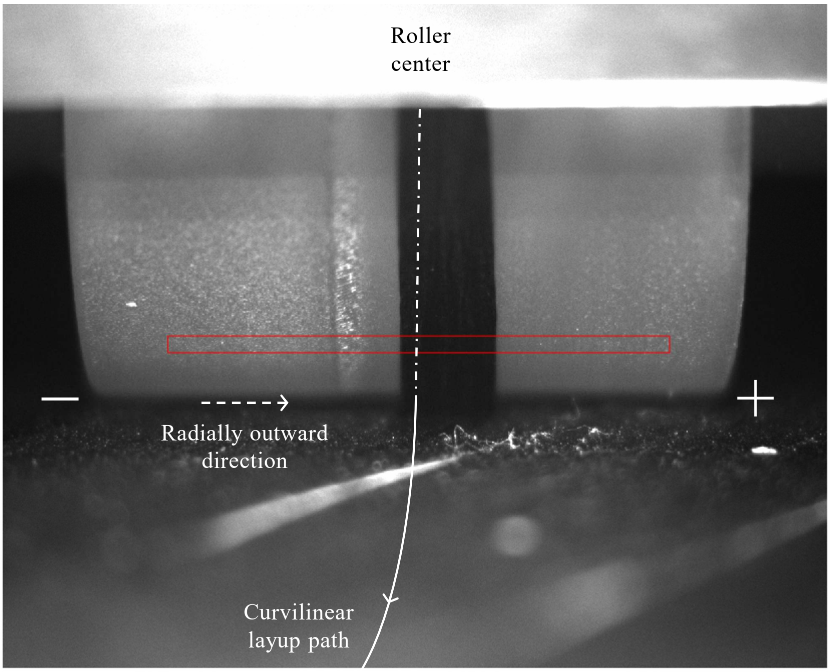

Figure 5.3: Example frame recorded by the camera. The measurement window is annotated in red while the roller center is annotated with a white dashed line.

whose dimensions are accurately known from its micrograph. The details of this method of tow detection and measurement can be found in section 3.1.3.

5.3. Experimental results

The tow lateral movement measured during the experiment while being laid down at various steering radii, has been presented in figure 5.4. The top two plots in figure 5.4 show the tow lateral movement as it is measured during the numerous 1 m arc length layups for material 1 (top, left) and material 2 (top, right). The dash dotted line represents the center line of the roller.The upward arrow represents the radially outward direction in relation to the planned circular path. Note that the tow position measurements at the various locations along the arc length of the tow have been plotted from the point of view of the camera mounted on the AFP head. Therefore, while the layup was curvilinear, tow lateral movement measurements with respect to the roller center line are plotted about a straight line i.e. along a straightened arc length, for ease of comparison.

The dark blue lines represent the tightest turning radii while the greenest lines represent the shallowest turning radii. The lines gradually change color from green to blue as the turning radius gets tighter. The tow tends to shift in the radially outward direction for both material 1 and material 2. This effect is more apparent for material 2.

The line plots start a bit after 0 mm because the camera doesn't measure the small initial lengths of the tow which has been extended beyond the camera view before the layup starts. However,

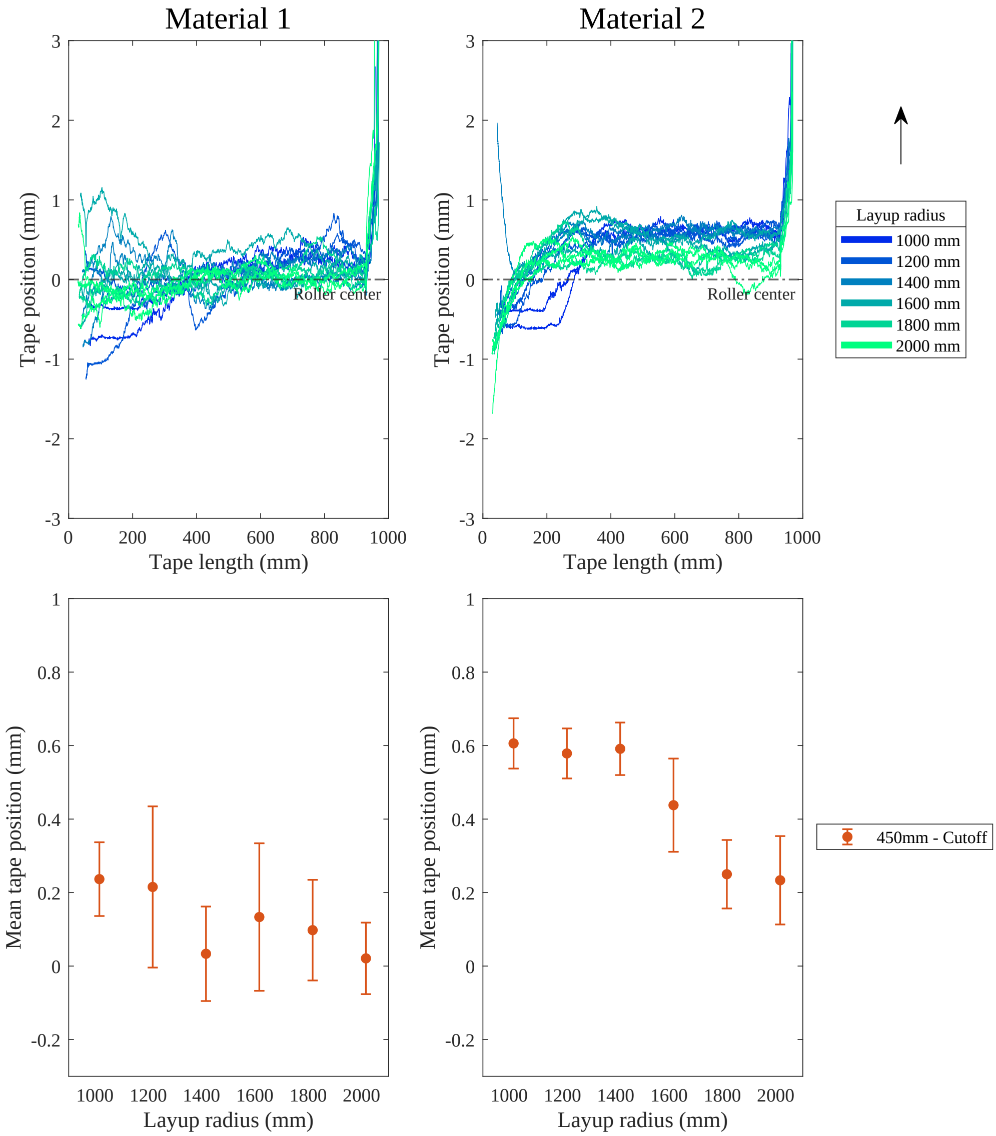

Figure 5.4: Tow lateral movement for material 1 (left, top and bottom) and material 2 (right, top and bottom) for various values of steering radii. The top two figures show tow lateral movement tracked by the camera as the layups progress in arc length from 0 to a 1000 mm. The tracked tow lateral movement is plotted along the straightened arc length of the laid tow for clarity. The arrow indicates the radially outward direction of the curvilinear layup paths. The bottom two figures show the means and $\pm 1\sigma$ values of the tow position for the portion of the layup from 450 mm to the cutoff at 930 mm.

the effect of the variations in the start positions on tow lateral movement are still visible for both materials. The start positions are expected to be affected by the guillotine cutter action in the preceding layup before the extension of unsupported tow. They are also affected by the contact of the unsupported tow with the tool during the approach motion. For material 1, the tow start positions seem to be well distributed on both sides of the roller centerline while for material 2, the tow start positions seem to be mostly on one side of the roller. These trends are expected to affect the tow lateral movement behavior in the initial lengths of the layups.

For material 2 (top, right), one can observe that the tow positions for all steering radii shift in the radially outward direction and stabilize by the time the tow length reaches 450 mm. Moreover, a gradient from green to blue is seen signifying that as the layup radius reduces, the tow stabilizes at a value further away from the center. This phenomenon is also observed for material 1 (top, left), albeit less clearly. Moreover, the tow position for material 1 has more variation.

To better understand this phenomenon, the mean position and the standard deviation of the tow position for each steering radius is shown in the bottom plots of figure 5.4. These means were calculated for the stabilized region of the tow layup from 450 mm to the cutoff at 930 mm. For material 1 (bottom, left), a trend of increasing average tow shift for decreasing steering radius is observed. For material 2 (bottom, right), this trend is observed more clearly. The variation of the tow position of material 1 (top, left) is also reflected in the relatively higher spread seen in the distribution of the mean tow position values (bottom, left).

The layup after the cutoff (i.e., at tow lengths greater than 930 mm) shows a distinct increase in shift of tow position. The tow position starts shifting after the cutoff while a part of the remaining tow is still in the chute. Once the tow has exited the chute the rate of position shift increases even further.

5.4. Analytical framework for tow lateral movement

The experimental observations presented in section 5.3 revealed several behaviors such as the steering radius dependent tow movement in the radially outward direction, the stabilization of the tow and the noise characteristics. These behaviors are the central contribution of this study because, to the best of the author's knowledge, they have not been previously observed or measured. The following preliminary analytical framework was implemented to capture the major principles of the process to give context to these experimental observations rather than to provide a comprehensive treatment like in complex, resource intensive finite element analysis.

The framework consists of a static force model and kinematic analysis which was developed to understand the observed tow lateral movement behavior on the compaction roller. The model for a single tow segment combines beam bending, shear deformation, and Coulomb friction. It is formulated under quasi-static equilibrium assumptions during steady AFP placement, without time integration or dynamic effects.

The analytical model calculates the resultant lateral force on the tow when given the values of various process and material parameters.This leads to the calculation of the unbalanced force on the tow. The direction of this unbalanced force implies the direction of the tow lateral movement. The equilibrium of these forces would signify stability of the tow lateral position.

5.4.1. Model parameters and inputs

The model inputs related to the layup process parameters and the AFP head configuration include steering radius, tow spool brake torque, spool fill level, compaction force, chute geometry, tow and roller geometry. Inputs related to material properties include tow moduli and frictional properties.

Tow, roller and chute geometry

Figure 5.5 shows the tow exiting the chute and going under the compaction roller as it is being laid. The tow exits the chute and tangentially makes contact with the compaction roller. This unsupported length between the chute and the tangential contact point is abbreviated as UL. The length UL was measured to be 12.2 mm for the AFP head used in the layup. After making contact with the compaction roller the tow approaches the nip point. This length of tow between the point it touches the compaction roller and the nip point is denoted as length A. The length of the tow which is under the compaction roller is denoted as length B. These lengths/regions of the tow are annotated as such in the figure 5.5. The region A of the tow is in contact with the compaction roller while region B is in contact with both the roller and the substrate.

As the compaction force gets higher, the contact area of the compaction roller with the tool increases. Thus, length B will increase while length A will decrease. The geometrical relationship between length A and length B involves the roller diameter and the respective subtended central angles. The AFP head used for the experiment has a compaction roller which is mounted on a pneumatic piston with a diameter of 40 mm. One can set the pressure in the piston to change the force on the roller. Pressure was varied from 0.1 to 0.5 MPa and the length B was measured by a length scale under the roller. The acquired data points were fit with a 4th order polynomial equation to get a relationship between the total compaction force and region B geometry.

The experimental data were fit with the following polynomial relationship:

$$\text{Tape length } B = -231.26\,P^4 + 525.34\,P^3 - 401.86\,P^2 + 135.45\,P + 0.0071 \tag{5.1}$$

where P is the pneumatic piston pressure (MPa). The pressure was converted to compaction force using the piston dimensions:

$$F_c = P \cdot \pi R_p^2 \tag{5.2}$$

where R_p is the piston radius. Figure 5.6 shows the relationship between the compaction force and the length B along with the fit.

Tow material properties

The model was run using various material properties for material 1 and material 2. Some of the properties were provided by the manufacturer while others were chosen from a range found in literature. These material properties were assumed to be uniform and constant.

Material 1 was thinner with a nominal thickness of 0.185 mm while Material 2 was thicker with a nominal thickness of 0.24 mm. Both materials have a nominal width of 6.35 mm. Nominal material dimensions were used, and any dimensional variations were neglected because of their relatively minor role on the results. Both the prepregs were made from Toray T700SC carbon fiber but had two different epoxy matrices. Material 1 was less tacky and had a fiber volume

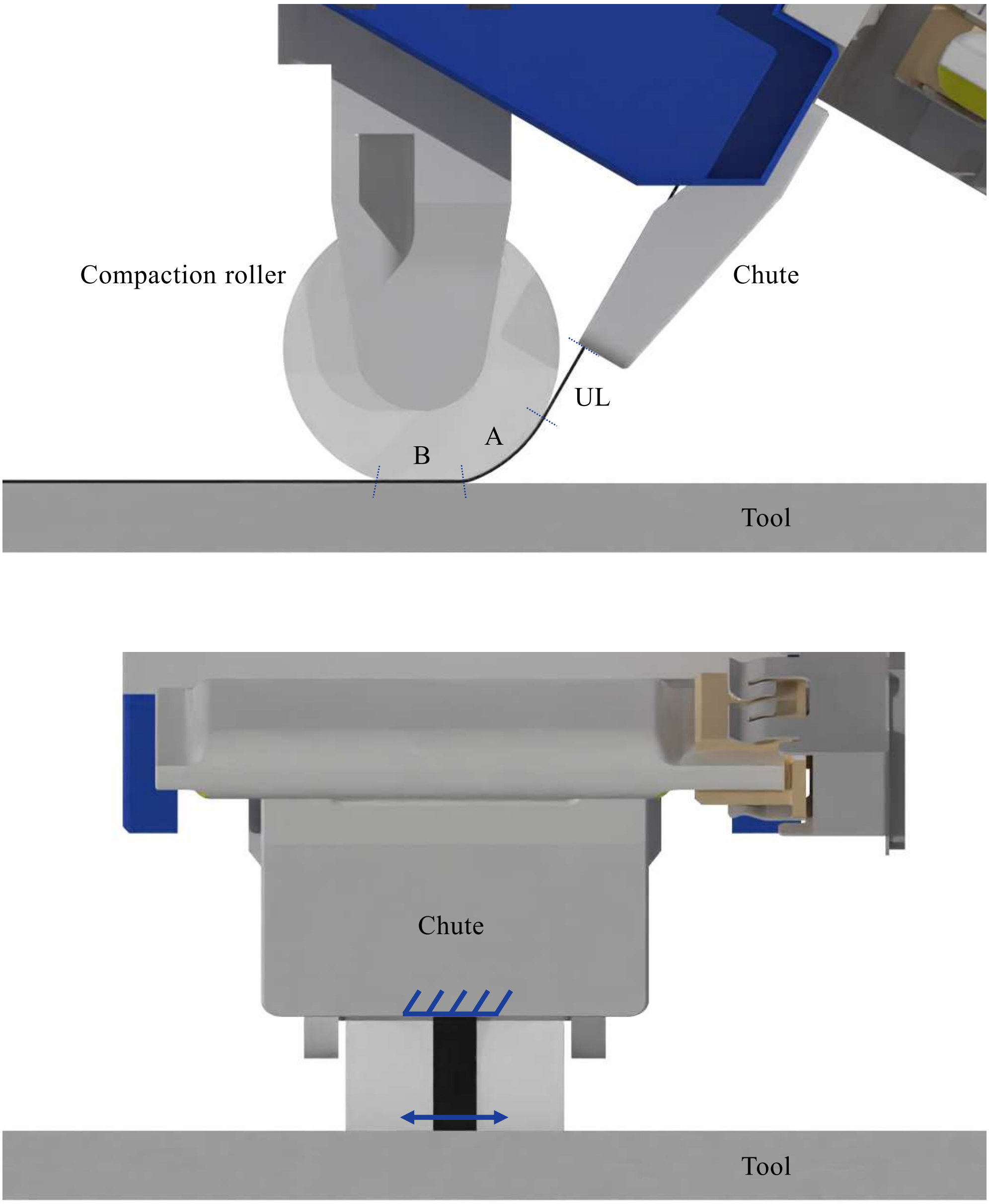

Figure 5.5: Geometry details of the tow going under the compaction roller after exiting the chute (top). Annotations showing fixed support of the beam along with the direction of deflection (bottom).

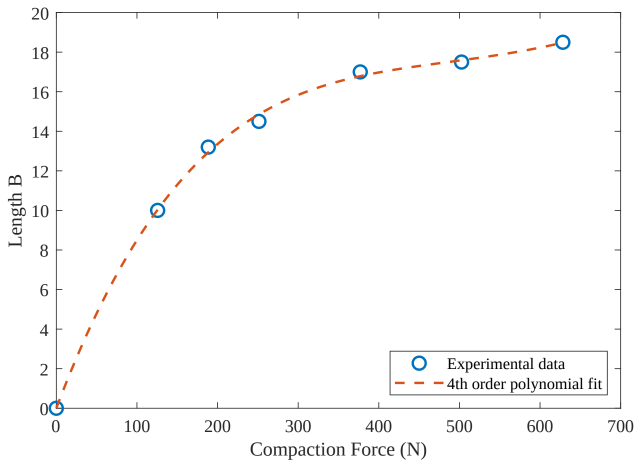

Figure 5.6: Polynomial fit to experimental data obtained by measuring the roller compaction region width B for various values of compaction pressure.

fraction of 65% while material 2 was tackier and had a fiber volume fraction of 67%. The stiffness of the fibers and the fiber volume fraction was known from the material specification sheet. Properties like the Poisson's ratio, matrix stiffness were selected to reflect typical values for such aerospace-grade thermoset materials. Voigt's expression was used to calculate the Young's modulus of the prepreg tow [113].

$$E_1^V = V_f E_1^f + V_m E^m + \frac{2V_f V_m \left(\nu_{12}^f - \nu^m\right)^2}{V_f X_m + V_m X_f} \tag{5.3}$$

$$X_m = \frac{(1+\nu^m)(1-2\nu^m)}{E^m} \qquad X_f = \frac{1-\nu_{23}^f}{E_2^f} - \frac{2(\nu_{12}^f)^2}{E_1^f} \tag{5.4}$$

where $V_f + V_m = 1$, E_1^f and E_2^f are the fiber longitudinal and transverse moduli, ν_{12}^f and ν_{23}^f are the fiber Poisson's ratios and E^m, ν^m are the matrix Young's modulus and Poisson's ratio.

The coefficient of friction of 0.1 was chosen for the tow-roller interface while the coefficient of friction of 0.2 was chosen for the tow-tool interface. These coefficients were assumed to be constant. A sensitivity study has shown that the average tow shift prediction is almost insensitive to these coefficients. The frictional properties were chosen from a range found in literature for thermoset prepreg tows [114, 115].

Shear modulus calibration

The shear modulus of the prepreg tow under AFP layup conditions is not directly available from manufacturer data and is expected to be sensitive to factors such as resin state, temperature history, and shear-dominated deformation in B-staged thermoset systems. Therefore, the

Property	Material 1	Material 2
Width (mm)	6.35	6.35
Thickness (mm)	0.185	0.24
Youngs modulus (GPa)	129	138
Shear modulus (GPa)	2	0.67

Table 5.2: Tow properties.

tow shear modulus was determined through calibration against experimental observations. A literature-informed range of shear modulus values was explored using a grid search approach. Calibration was performed using experimental tow lateral movement data from four steering radii (1200, 1400, 1600, and 2000 mm), with the objective of minimizing the discrepancy between model-predicted and experimentally observed equilibrium zone mean and range values across these radii. The shear modulus value that provided the best overall agreement was selected for each material. Once calibrated, the shear modulus was kept unchanged for all subsequent simulations including predictions for steering radii which are not included in the calibration set.

Consequently, the known, calculated and calibrated values of the tow properties discussed in the previous two sections which are utilized in the model are listed in table 5.2. The predictive accuracy of the model will depend on these model parameters. While this affects the quantitative predictions, the model should be able to capture dominant physical relationships. However, experimental determination of material parameters is identified as an important direction for future work on this analytical framework. Future extensions of the framework could also replace the calibrated apparent shear modulus with a time and temperature dependent shear response that incorporates viscoelastic effects. As the tow segment forming the effective beam length is replaced rapidly during layup, the effect of viscoelastic relaxation timelines on the beam behavior has not been quantified and therefore warrants investigation.

5.4.2. Governing equations

The various forces acting on the tow are calculated for every measured value of tow lateral movement. This included the bending force F_b, the tension lateral component T_{lat} and the tow-roller shear force F_s. These forces acting in the respective positive or negative directions are summed to find the interim resultant force.

$$F_{\text{net}} = \pm F_b \pm T_{\text{lat}} + F_s \tag{5.5}$$

All the friction forces from region A and region B combine to oppose the interim resultant force. The tow is considered to have a final resultant force acting on it only if the interim resultant force is greater than the total friction force.

$$F_{\text{resultant}} = \begin{cases} F_{\text{net}} - F_{\mu,\text{total}} & \text{, if } |F_{\text{net}}| > |F_{\mu,\text{total}}| \\ 0 & \text{, otherwise} \end{cases} \tag{5.6}$$

An example of this force balance is illustrated in figure 5.7. Note that magnitude and directions

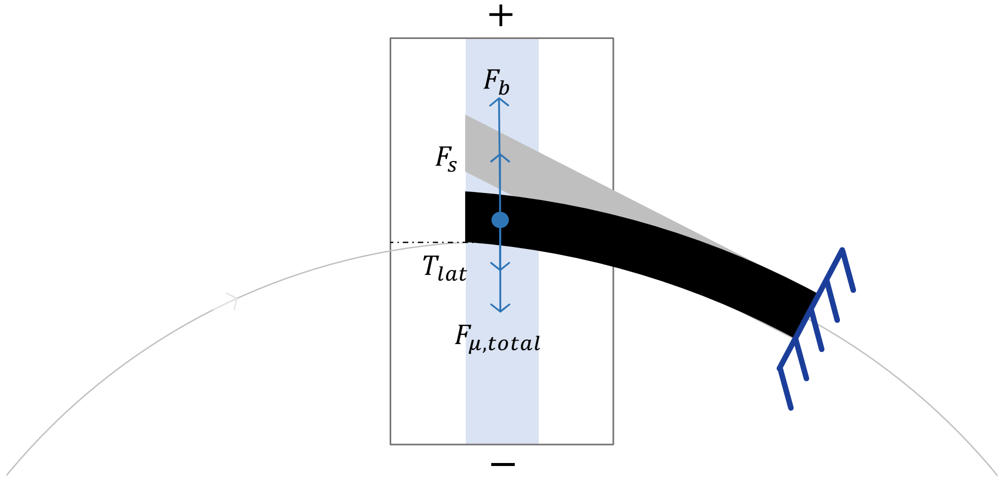

Figure 5.7: Schematic showing example forces acting on the tow segment treated as a cantilever beam. The magnitude and directions of the illustrated forces change according to tow position. Schematic is not to scale, in interest of clarity.

of the respective forces can change depending on the tow position with respect to the roller center.

Bending force

During steering, the straight tow is being deflected to lay it along a circular path. This deflection is indicated as $\delta_{\text{straighten}}$ in the schematic figure 5.9, showing the tow at the compaction roller. The beam tries to remain straight by deflecting in the radially outward direction trying to minimize its bending strain energy. Thus, the beam deflection is considered zero when the tow position has a value of $\delta_{\text{straighten}}$ in the positive direction. This zero-deflection beam configuration is shown in grey. The orange dot annotated in figure 5.9 is at a distance of $\delta_{\text{straighten}}$ from the roller center and depicts the tow position when the bending strain energy is zero.

The arrows in figure 5.9 show the direction of positive and negative tow lateral movement (TLM) with respect to the roller center line. The deflections measured in the experiment are measured about the roller center. The effective deflection of the beam is calculated about the zero deflection point annotated in orange in figure 5.9.

When the tow is deflected to a value greater than $\delta_{\text{straighten}}$, the bending force acts in the positive direction. This would mean that the reaction force is acting in the negative direction. When the tow is deflected to a value lower than $\delta_{\text{straighten}}$, the bending force acts in the negative direction. This would mean that the reaction force is acting in the positive direction. The reaction forces act in directions which reduce the deflection magnitude to minimize strain energy.

Thus, if Δy is the tow lateral position, the effective deflection of the tow beam, δ, is given by

$$\delta = \begin{cases} \delta_{\text{straighten}} + |\Delta y| & , \Delta y < 0 \\ \delta_{\text{straighten}} & , \Delta y = 0 \\ \delta_{\text{straighten}} - |\Delta y| & , \Delta y > 0 \quad \& \quad |\Delta y| < \delta_{\text{straighten}} \\ 0 & , \Delta y > 0 \quad \& \quad |\Delta y| = \delta_{\text{straighten}} \\ |\Delta y| - \delta_{\text{straighten}} & , \Delta y > 0 \quad \& \quad |\Delta y| > \delta_{\text{straighten}} \end{cases}$$

A Timoshenko beam model is used because shear strain is expected to be significant in the prepreg unidirectional tow. A rectangular cross-section is assumed with a shear correction factor $k_s = 5/6$. Therefore, the bending force which would result in an effective beam deflection of δ is given by

$$F_b = |\delta| \cdot \left(\frac{1}{E_B + T_s} \right) \tag{5.7}$$

$$E_B = \frac{L_b^3}{3EI} \tag{5.8}$$

$$T_s = \frac{L_b}{k_s\, G\, A} \tag{5.9}$$

where L_b is the beam length, δ is the effective beam deflection, E is the Young's modulus, G is the shear modulus. I is the second moment of the area of the tow cross-section and A is the cross-sectional area of the tow whch are given by

$$I = \frac{T_t \cdot W_t^3}{12} \tag{5.10}$$

$$A = W_t \cdot T_t \tag{5.11}$$

where T_t is the tow thickness and W_t is the tow width. Figure 5.8 shows the tow cross-section and the sideways direction of deflection for clarity.

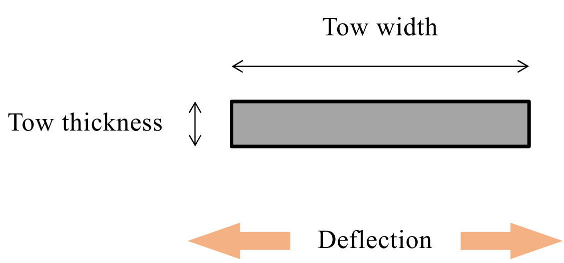

Figure 5.8: Tow cross-section and direction of deflection of the tow segment

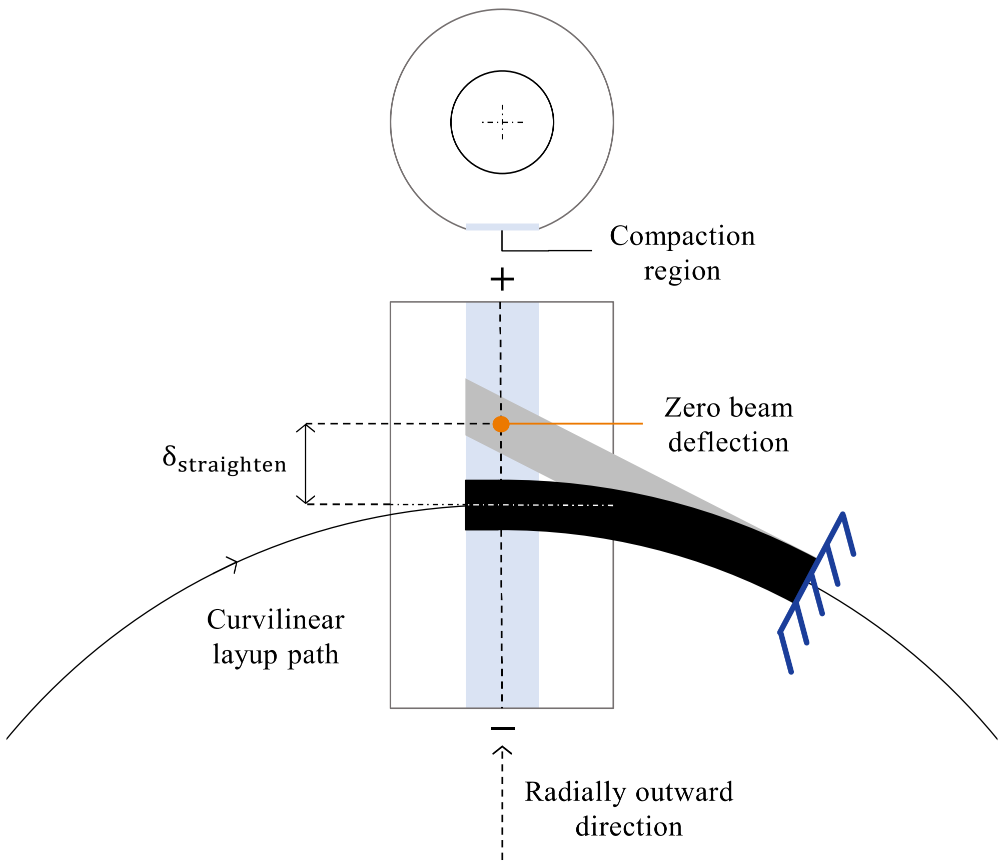

Figure 5.9: Schematic showing details of the beam deflections and tow lateral movement reference system. Note that the elements are not to scale, in interest of clarity.

Tow tension

The spool is mounted on a rotary magnetic brake which can be set to create the desired amount of tension in the tow. For example, the experiments were carried out at 75% braking capacity which translated to a 423.3 Nmm braking torque. The spool was approximately half full resulting in a moment arm of 125 mm. Thus the resulting tow tension was 3.4 N. When the tow is at the roller center, the tension is in the tow length direction. However, when the tow is moving laterally, a component of the tension acts in the lateral direction. The lateral component of tension is given by

$$T_{\text{lat}} = T \cdot \cos(\theta_{\text{tow}}) \tag{5.12}$$

$$T = \frac{\tau}{r_s} \tag{5.13}$$

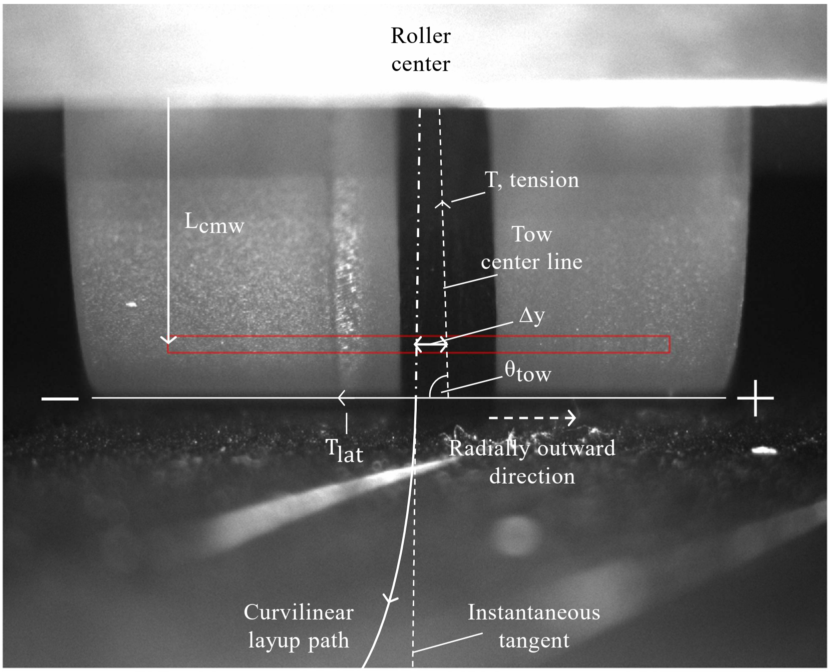

Figure 5.10: Example camera frame shows an instance when the tow is seen in a position shifted from the roller center. The tow angle with the roller center is annotated.

$$\theta_{\text{tow}} = \tan^{-1}\left(\frac{L_{\text{cmw}}}{|\Delta y|}\right) \tag{5.14}$$

where T is the tow tension, τ is the spool brake torque, r_s is the spool radius, L_{cmw} is the tow length from the chute to the annotated measurement window, Δy is the tow lateral position and θ_{tow} is the angle made by the tow with the roller center. These are illustrated in figure 5.10.

This tension lateral component acts in the positive direction when the lateral movement is on the negative side of the roller center line. Similarly, the tension lateral component acts in the negative direction when the lateral movement is on the positive side of the roller center line. Thus, the tension lateral component pushes the tow towards the tow roller center.

Roller-tow shear force

Rajan et al. found that as the tow is being laid up in a curvilinear path, the roller exerts shear forces on the top surface of the tow [58]. A component of the roller-tow shear forces acts in the positive direction shown in Figure 5.7, which is also the radially outward direction. This shear force tends to zero as the steering radius approaches infinity i.e. becomes a straight line.

Values of tow-roller shear forces were known for two steering radii from the numerical study of Rajan et al. [58]. This study also used a prepreg thermoset material albeit with a different matrix than the one used in our experiment. However these values were chosen because, to the best knowledge of the author, it is the sole source of such data in literature. The experimental data was therefore fit with an exponential decay function giving the shear force F_s as

$$F_s = a \cdot e^{-b \cdot \text{Steering radius}} \tag{5.15}$$

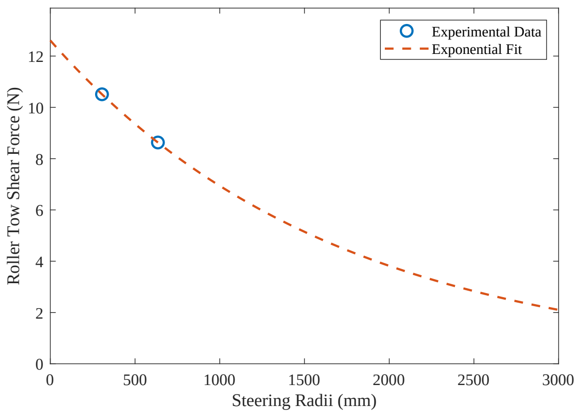

Figure 5.11: Exponential fit to data about tow-roller shear force at different steering radii from Rajan et al. [58].

where $a = 12.61$, $b = 5.97 \times 10^{-4}$. Figure 5.11 shows the two data points along with the fit. The exponential decay function was selected because it asymptotically approaches zero. It is recognized that there are not enough data points. However, alternative fits like a linear or power law, did not change the conclusions of the chapter.

Frictional forces

The compaction roller assembly is mounted on a pneumatic piston cylinder arrangement. The total compaction force F_c is calculated from the piston dimensions and the applied pneumatic pressure. The total compaction area A_c is given by

$$A_c = B \cdot W_r \tag{5.16}$$

where B is the length of the tow under the compaction roller as seen earlier in figure 5.5. W_r is the width of the compaction roller.

Compaction pressure is obtained from

$$P_c = \frac{F_c}{A_c} \tag{5.17}$$

Thus, effective compaction force on the tow of width W_t would be

$$F_{c,\text{eff}} = P_c \cdot B \cdot W_t \tag{5.18}$$

A component of the tow tension also acts towards the center of the compaction roller as seen in figure 5.12. It is assumed to create a uniformly distributed bearing load. The radial force from tension F_r, is dependent on θ_{wrap} which is the tow wrap angle on the compaction roller. θ_{wrap} is the central angle subtended by tow length A and B. F_r is distributed among region A and region B depending on the relative lengths of A and B. This bearing load is normal to the tow in region A and region B. Note that the bearing load on region B is in opposite direction of the compaction force.

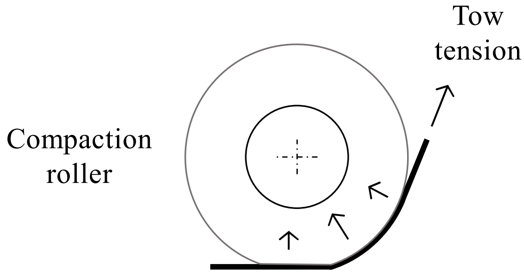

Figure 5.12: A component of the tow tension acts toward the roller axis, resulting in a bearing load.

The compaction force and the bearing loads together determine the forces on region A and region B which are given by

$$F_B = F_{c,\text{eff}} - \frac{B}{A+B} \cdot F_r \tag{5.19}$$

$$F_A = \frac{A}{A+B} \cdot F_r \tag{5.20}$$

A is the length of the tow from the contact point to the nip point as seen earlier in figure 5.5.

The normal force values from the compaction force and the bearing load are used to calculate friction forces acting on the tow in region A and region B. Now, the friction forces in region A are due to tow-roller contact while the friction forces in region B are due to the tow-roller contact and the tow-tool contact. The factor γ used in equation 5.25 is detailed in the following section 5.4.3. The direction of the frictional forces $F_{\mu,\text{total}}$ is in opposition to the interim resultant force defined in equation 5.5. This is also illustrated in the schematic of the example forces in figure 5.7.

$$F_{\mu,A} = \mu_{\text{tow-roller}} \cdot F_A \tag{5.21}$$

$$F_{\mu,B}^{\text{top surface}} = \mu_{\text{tow-roller}} \cdot F_B \tag{5.22}$$

$$F_{\mu,B}^{\text{bottom surface}} = \mu_{\text{tow-table}} \cdot F_B \tag{5.23}$$

$$F_{\mu,B} = F_{\mu,B}^{\text{top surface}} + F_{\mu,B}^{\text{bottom surface}} \tag{5.24}$$

$$F_{\mu,\text{total}} = F_{\mu,A} + \gamma \cdot F_{\mu,B} \tag{5.25}$$

Figure 5.13 summaries the flow of parameter values in various interconnected relationships related to the tow bending force, tow tension, roller-tow shear, and friction forces.

5.4.3. Applied boundary conditions

The tow is observed to move laterally in the camera data but is constrained in the chute. It is thus modeled as a cantilever beam with the chute as the fixed end. Figure 5.5 (left) shows the length dimensions of the beam. Figure 5.5 (right) shows the fixed end of the beam at the chute exit while the arrows show the direction of the deflection of the beam. The width of the tow is the height of the beam model while the thickness of the tow is the depth of the beam model.

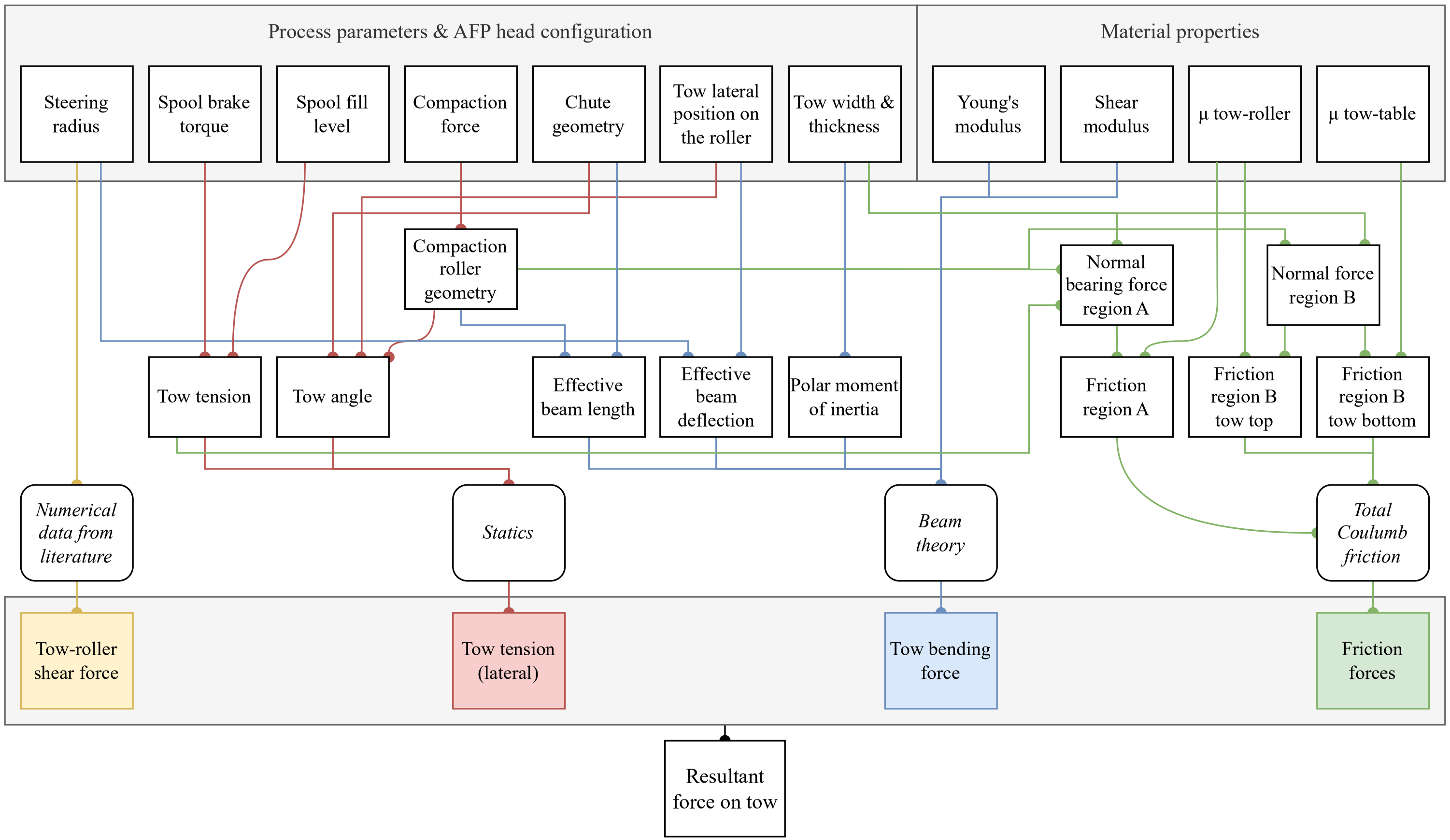

Figure 5.13: Summary flowchart for the resultant force model for tow lateral movement with various input variables, governing equations and outputs.

The tow bonding to the substrate is dependent on its tackiness. The tow cannot deflect once bonded to the substrate. Thus, the beam length L_b is given by

$$L_b = UL + A + \gamma \cdot B \tag{5.26}$$

where $\gamma \in [0, 1]$ is a factor which denotes the proportion of length B included in the beam length.

For materials with high tackiness, the tow would bond with the substrate as soon as it reaches the compaction roller and, thus, γ would be closer to 0. For materials with low tackiness, the opposite is true and γ would be closer to 1. The higher tackiness of material 2 was reflected in the length of the beam seen in figure 5.5. Tack is the material's ability to form an adhesive bond under certain pressure conditions in relevant contact times. A higher tack material more readily wets and adheres to the substrate upon initial contact, thereby reducing the distance required to achieve bonding. The material 2 is assumed to bond to the substrate at 1/3 of the length B while material 1 is assumed to bond to the substrate at 2/3 of the length B. This effectively shortens the length of the beam model for material 2 compared to material 1 by a small margin.

5.4.4. Model predicted equilibrium behavior

The model results in a stable region of tow positions which are offset from the roller center depending on the steering radii. These regions are where the interim resultant forces from the model are not large enough to overcome the total friction in regions A and B. When the tow is on either side of this stable region, the resultant forces push it into the stable region. The further away the tow is from the stable region, the greater is the resultant force pushing the tow towards the stable region. The model results show that when the tow enters this stable region it will stay there. This is because if the tow tries to exit the stable region, the resultant force will act towards the stable region.

This behavior is seen in the experimentally recorded tow lateral movement. The tow was observed to move to a stabilized position away from the roller center. The stable regions from the model for material 1 and material 2 can be seen in figure 5.14 (top, left & top, right respectively) in gray color. The same plots are overlayed with experimental tow lateral movement data in orange color. The solid orange and hollow orange markers show the experimentally observed maximum and minimum values of tow lateral movement. Note that the experimental data shown in figure 5.14 is from the stabilized layup region from 450 mm to 930 mm (tow cutoff). Figure 5.14 (middle, left & middle, right) shows the mean of the model stable regions along with the mean of the experimentally observed tow lateral movement data. Figure 5.14 (bottom, left & bottom, right) shows the range of the model stable regions along with the range of the experimentally observed tow lateral movement data.

5.4.5. Model validation and predictive accuracy

For material 2, one can see good correlation between the model data and the experimental data in terms of both the mean and the range of tow lateral movement values. The model correctly predicts the greater shift of the tow lateral movement stable regions as the steering radius reduces.

For material 1, the predicted range correlates well with the range of the experimental data. However, the means of the model for material 1 correlate with the experimental means only

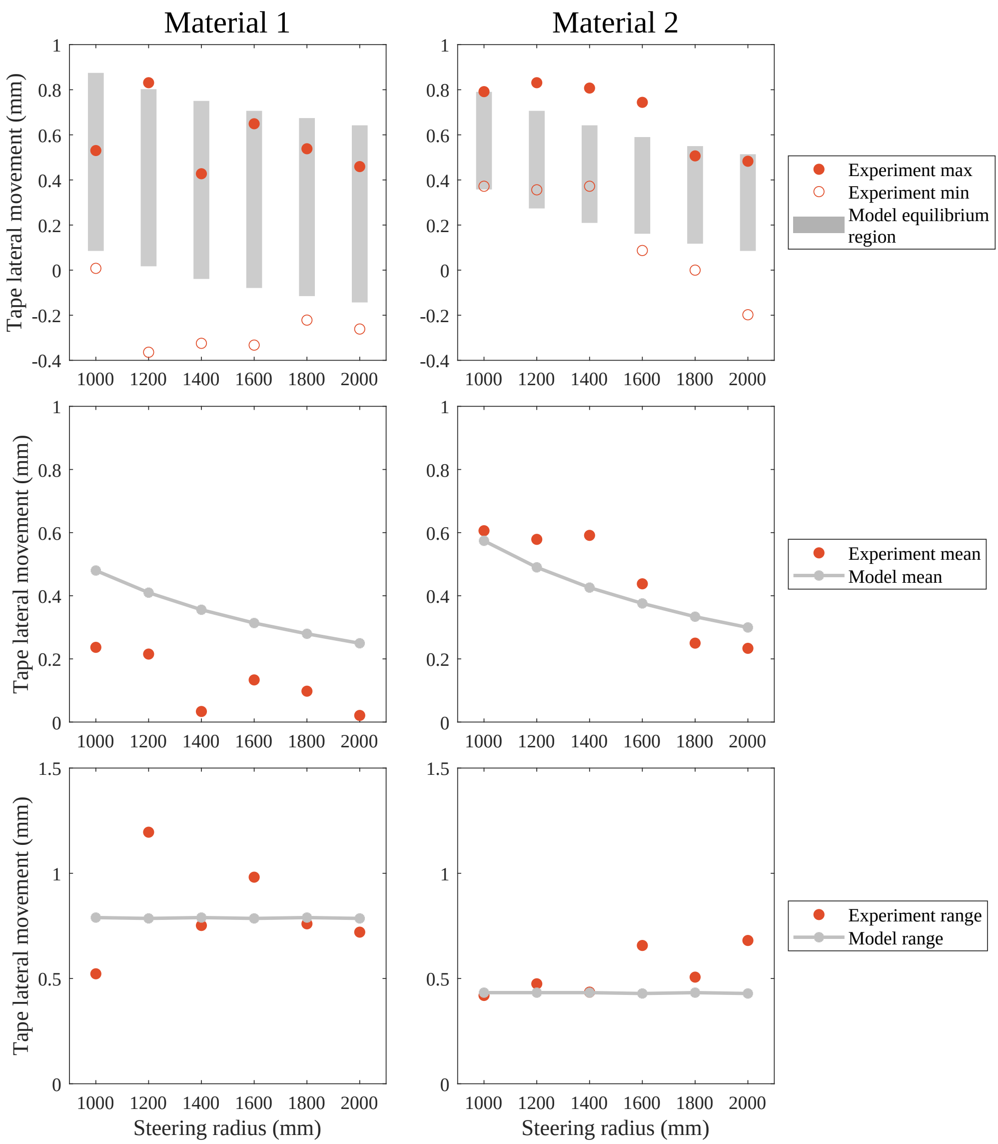

Figure 5.14: Equilibrium zones predicted by the model plotted along with the experimental data for material 1 and material 2 for various steering radii. The experimental data only includes the layup region of 450 mm - cutoff.

in trend but not in magnitude. This could be because the model is static and does not account for visco-elastic properties of the tow. More accurate measurements of the tow properties in the layup conditions could also help improve the accuracy of the model.

To validate the model, comparisons between the experiment and the model were done for the extrapolated steering radius of 1000 mm and the interpolated steering radius of 1800 mm, for material 2. These radii were not used for the calibration discussed in 5.4.1.

Mean absolute error (MAE) was used for the comparison.

$$\text{MAE} = \frac{1}{n}\sum_{i=1}^{n}|y_i - \hat{y}_i|$$

where n is the number of data points used in the comparison, y_i is the experimentally measured value, and $\hat{y}_i$ is the corresponding model-predicted value.

The MAE for the tow lateral movement mean and range for 1200, 1400, 1600 and 2000 mm steering radii is 0.17 mm and 0.07 mm. Whereas, the MAE values for the tow lateral movement mean and range for 1000 mm and 1800 mm steering radii was calculated to be 0.3 mm and 0.23 mm.

To get a quantitative sense of these MAE values, they were also expressed in terms of percentage of the measured tow lateral movement mean and range. The tow lateral movement mean and range were 38% and 13% for 1200, 1400, 1600 and 2000 mm steering radii. Whereas, for 1000 mm and 1800 mm steering radii they were 67% and 43%.

In figure 5.4 (top) noise is seen in the tow lateral movement experimental data from the individual layups. This could be because of the scatter in the geometry and material properties of the tow, roller and tool. This noise is higher for material 1 than material 2. This could be related to the stability of the tow in the equilibrium region. If the resultant forces keeping the tow in the stable region are weaker, as in the case of material 1, they would result in a wider range of tow lateral movement as seen in figure 5.14 (top, left).

5.5. Utility of predicting tow lateral movement

5.5.1. Sensitivity analysis

Since the model captures some of the physics of the tow lateral movement, a sensitivity analysis can help understand the significant parameters associated with the observed phenomenon. This might give insight on how this phenomenon might be reduced or compensated against. The various process parameters which were used in the model are listed in table 5.3. The table includes the nominal values and a typical range of these parameters. The model was run while varying each of these parameters individually while keeping the others at nominal values. The model results in stable regions where the interim resultant forces from the model are not large enough to overcome the total friction. When the tow is on either side of this region, the resultant forces push it into the region. Once the tow enters this stable region it will stay there. In the model results, the mean value of the stable region would signify the expected average magnitude of the tow lateral movement shift away from the roller center. The range of the stable region would signify the noisiness of the tow lateral movement when the tow is within the stable region. The model was run to understand how the means and ranges of the stable

Parameter	Nominal value	Range	
		Min	Max
Steering radius (mm)	1500	1000	2000
Tow length UL (mm)	12.2	10	20
Tow length A (mm)	15	10	20
Tow length B (mm)	15	10	20
Tow width (mm)	6.35	6.1	6.6
Tow thickness (mm)	0.21	0.185	0.24
Tow Young's modulus (GPa)	152	145	160
Tow shear modulus (GPa)	1.5	0.6	3
Tow-roller coefficient of friction	0.1	0.05	0.5
Tow-tool coefficient of friction	0.2	0.05	0.5
Compaction force (N)	377	126	628
Spool radius (mm)	125	85	155
Spool brake torque (N mm)	423	124	608

Table 5.3: Nominal values and range of parameters used in the sensitivity study.

region would vary for various parameter values. Thus, these calculations would give insights about the sensitivity of the tow lateral movement behavior to various process parameters.

The gray bars in figure 5.15 show that the expected magnitude of tow lateral movement away from the center is most sensitive to the steering radius and the geometry of the tow beam. The increasing shift of the tow for tighter steering radii has already been observed in the experimental results. The tow feed system consists of a chute from which the tow reaches the compaction roller. The distance and angle at which the tow is fed to the compaction roller determines the value of unsupported length UL and the length A where the tow is in contact with just the roller. This would mean that tow placement accuracy is dependent on the technology design of the feed system chute.

The light green bars in figure 5.15 show that the tow lateral movement stable region range is most sensitive to the tow-roller coefficient of friction and the tow-table coefficient of friction followed by the compaction force. These three parameters together decide the magnitude of the friction forces acting against the tow lateral movement.

Figure 5.16 and 5.17 show the trends in model results for a gradual change of the individual process parameter values within the ranges listed in table 5.3. In the original model, tow length A and tow length B are dependent on the compaction force. To attain these trend plots for tow length A and tow length B, the original model was modified to have them as independent variables.

5.5.2. Tow offset programming

Figure 5.18 shows the distribution of the measured tow position for material 2 when the layup length is changing from 450 mm to 930 mm. At 930 mm is the tow cutoff point. This figure

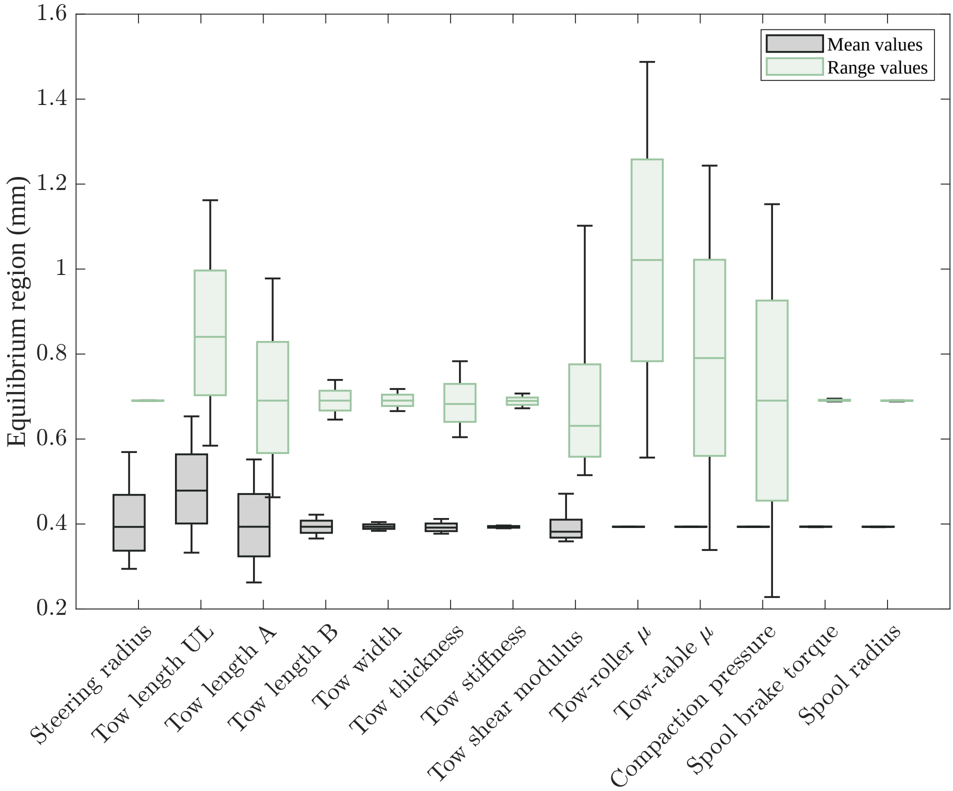

Figure 5.15: Sensitivity analysis of tow lateral movement behavior to various AFP process parameters

shows that the mean of the tow lateral movement is expected to increase gradually in the radially outward direction for decreasing values of steering radii. Thus the tow resultant force model allows us to predict the shift in mean position of the tow with respect to the programmed curvilinear path. Thus, knowing the shift before the programming can help in compensating against it by shifting of the programmed path in the radially inward direction i.e the opposite direction of the expected tow lateral movement. This would reduce the magnitude of gap and overlap defects in a laminate involving a curvilinear layup.

The curvilinear layup in this study was perfectly circular. However the model can calculate the shift for other curvilinear paths as long as the instantaneous radius from the Frennet-Serret frame is known along the path. If the curvilinear path is S-shaped, the shift will need to be calculated and compensation will be needed in both lateral directions of the path. The curvature in an S shaped path changes gradually, becomes zero and then changes direction. Thus compensation will also change gradually as the instantaneous curvature changes and will flip direction. In such a scenario the length of the curved path and the time taken to reach the stable zone will also need to be taken into account.

The AFP layup length can be divided into various clear phases. Phase A is when the tow is

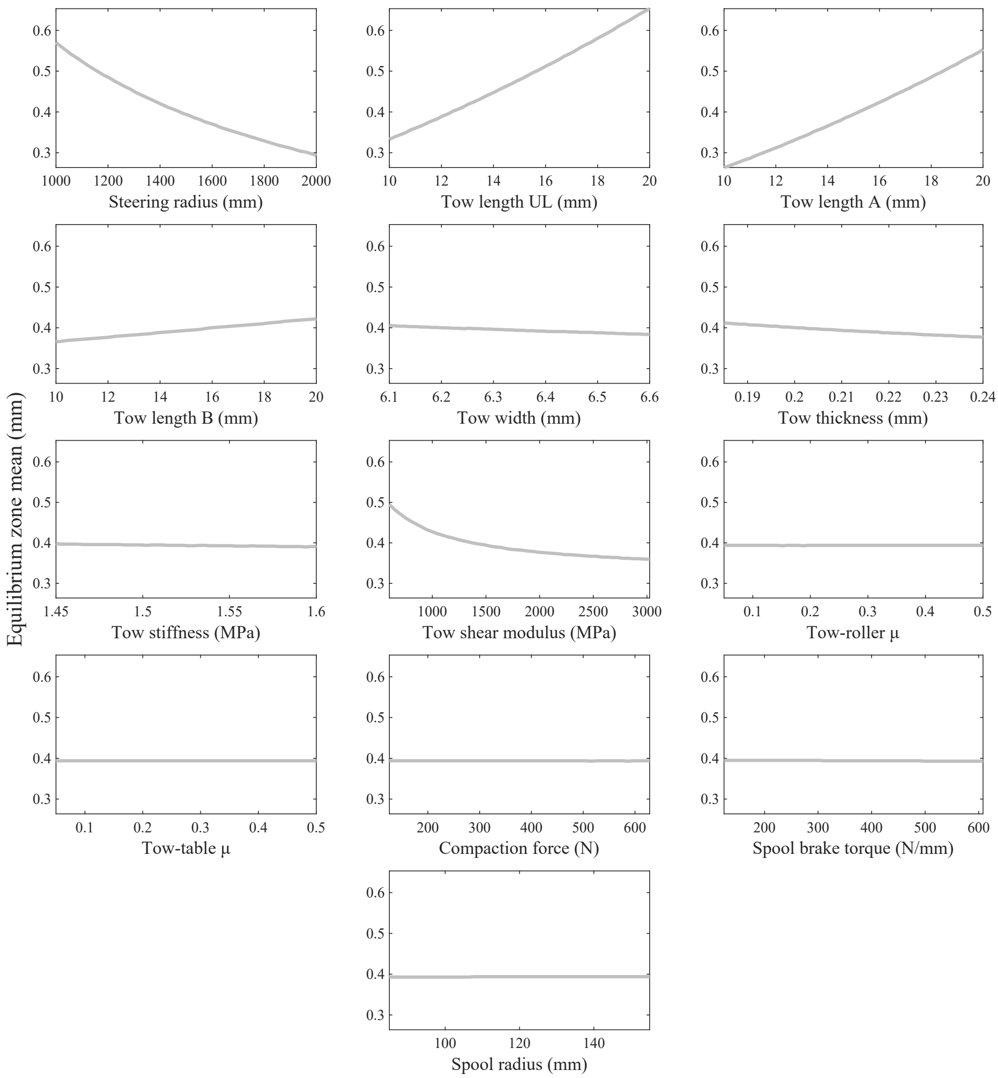

Figure 5.16: Trends in the equilibrium zone mean values for variations in the values of individual process parameters.

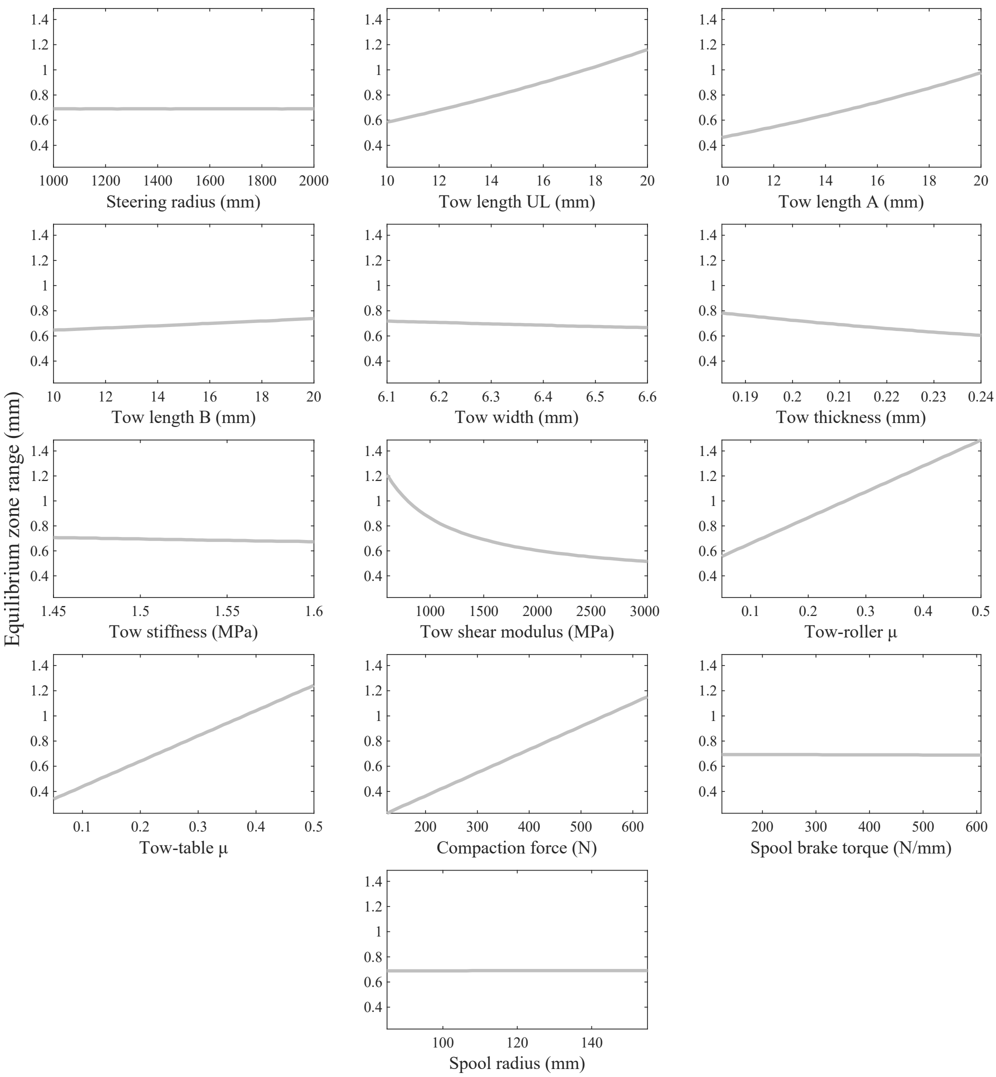

Figure 5.17: Trends in the equilibrium zone range values for variations in the values of individual process parameters.

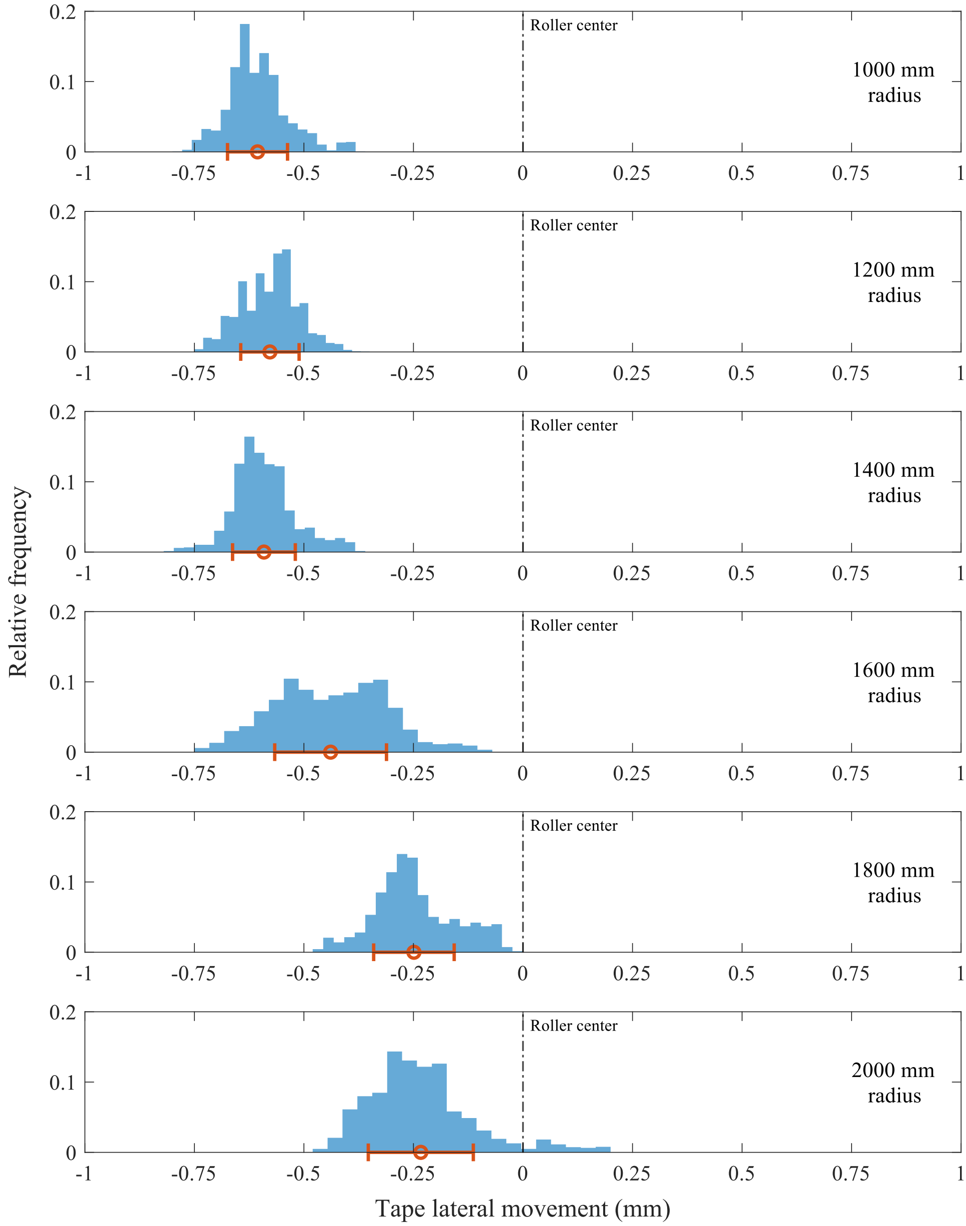

Figure 5.18: Experimentally measured distribution of tow positions for phase B of the material 2 layup at various steering radii.

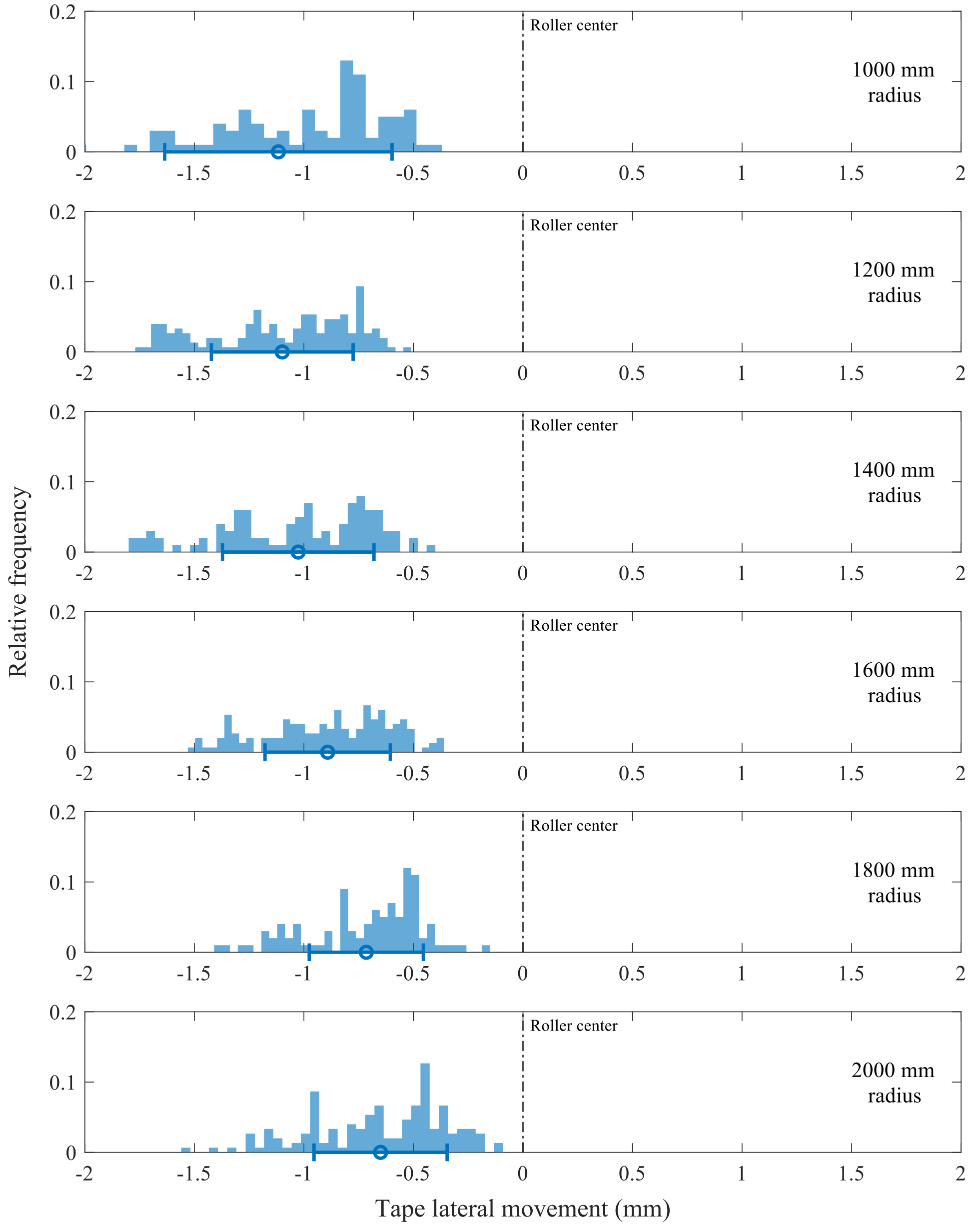

Figure 5.19: Experimentally measured distribution of tow positions for phase C of the material 2 layup at various steering radii.

moving laterally from the initial position to the stabilized position. Phase B is when the tow position is stabilized as is seen between 450 mm to 930 mm in figure 5.4. Phase C consists of the layup length when it is changing from 930 mm until the tow exits the chute at 975 mm. And phase D consists of the layup length when the tow exits the chute till the tow end. Figure 5.19 shows the distribution of the measured tow position from phase C for material 2. This phase of the layup is also seen in figure 5.4 (top, right) where the shift in tow position rises steeply at the end. This kind of shifts at the end of the layup would mean that every VSL would need its boundary areas to be trimmed away and wasted to avoid the very high deviations in tow position. This phase of the layup was not modeled. However, one can observe from figure 5.19 that the tow lateral movement maintains the same trend as seen in phase B shown in figure 5.18 but at a higher value of the shift of the mean position and also a higher spread. Thus, it might be possible to have an offset programmed for this phase of the AFP layup as well. This offset could be a linearly increasing value from the mean shift in phase B to the mean shift in phase C.

5.6. Limitations and future work

It is important to recognize the limitations of the current model since it predicts the lateral movement behavior after it has stabilized. This stabilized tow behavior was seen in the tow layup length of 450 to 930 mm from figure 5.4. Future work can focus on predictions for the phase of the layup before it reaches the stable regions or even after cutoff.

It was noted that the starting position of the extended tow before the layup approach also has a bearing on how early in the layup it will reach the stable region. The model presented here does not take into account the past values of tow lateral movement to predict the future values. This aspect could be explored in future works as well.

The roller wear band as seen in figure 5.10 is expected to have at least a minimal effect on the tow lateral movement. The wear band leads to the tow edges being in contact with the inclined wall of the wear profile on the cylindrical roller at the start of the steered layup. Comparative experiments with pristine and worn out rollers could be implemented to quantify this effect.

Since AFP manufacturing is widely applied to curved components, future studies can work on extending this model for steering on surfaces with various magnitudes of Gaussian curvature by accounting for the changed shape of the roller and its effects on the magnitude and directions of the tow tension, tow-roller shear force and friction. The proposed model should be viewed as a building block to which additional capability can be added, relatively easily, as required by the complexity of the part being made and the machine being used.

The experimental work in this investigation was achieved using a research purpose AFP head which lays down a single tow at a time. However, industrial AFP machines often have the capability to simultaneously lay down multiple tows adjacent to each other. In this scenario, steering would have the effect of trying to laterally move the inner tows with higher magnitudes than the outer tows. This could lead to inner tows bunching up against the outer tows. The relative time to achieve stable position will also vary between the inner and outer tows. Future work could attempt to experimentally observe these effects. The presented model would have to be enhanced to account for the boundary conditions involving contact between the multiple tows for predictive models of such complex interactions.

Further trials with tow lateral movement measurements during layup could use a broader range of process conditions to grow the model's domain beyond the scope of this investigation. These may include a range of layup speeds, compaction pressures and tow dimensions. The layup could also be done with varying magnitudes and directions of steering radii in a single layup path to understand the stabilization behavior and time over an arc length.

6

Conclusion

श्रेयान्द्रव्यमयाद्यज्ञाज्
ज्ञानयज्ञः परन्तप।
सर्वं कर्माखिलं पार्थ
ज्ञाने परिसमाप्यते॥

— भगवद्गीता 4.33

Greater than material action
is the pursuit of understanding;
for all action, without exception,
culminates in knowledge.

— Bhagavad Gītā 4.33

This chapter summarizes the key original findings of this thesis and the potential advantages of this work for AFP composites technology and process design. Possible future research directions which could build upon the insights developed by this work have also been discussed.

6.1. Scientific contributions

Identification and classification of the sources of variation

Gaps and overlaps are an inevitable reality of AFP composite layups. These defects warrant attention because they influence the subsequent manufacturing steps and the structural performance of AFP composites. These defects were divided into two broad classes depending on their causal origins. The first class of gaps and overlaps occur due to an inherent limitation in tow path generation for parts that have tows laid in non-geodesic paths. This occurs in flat parts manufactured by fiber steering or in doubly curved parts due to their geometry. The second class of gaps and overlaps are formed due to manufacturing process variations during the layup. The various sources of manufacturing process variations cause incorrect relative positioning of the edges of the tow. The manufacturing-induced defects were further classified based on whether this incorrect relative positioning of tow edges is caused due to position variations or geometry variations.

The position variations were broken down into robot path inaccuracies and tow lateral movement at the compaction roller. Tow lateral movement at the compaction roller is identified as an independent source of manufacturing variation in AFP. The geometry variations were broken down into tow width variations in the spool material and the tow width variations after compaction.

This structured breakdown is based on distinct and unambiguous causal mechanisms rather than observed defect morphology. This classification provides a conceptual foundation for experimental and statistical modeling efforts. Thus, it enables an understanding of how the different sources of variations contribute to defect formation and how they interact during the layup process.

Novel measurement techniques

An experimental setup involving various sensors mounted on an AFP head was implemented to simultaneously measure the sources of manufacturing variations in AFP composites. The experimental setup consisted of an AFP head instrumented with a laser tracker, a camera and laser line scanners. Each of these sensors measured a particular source of variation as described in the causal breakdown tree. The identified tow lateral movement was quantified for the first time using calibrated camera-based measurements and image processing of recorded frames.

A data acquisition system was built to simultaneously measure timestamped and position-stamped variation data from the four sensors measuring the respective four variations. This simultaneity was imperative for isolating individual contributions of the sources.

Relative significance of the sources of variation

The results of the methodology for measuring sources of variations for the AFP head-material combination used in the experiment are detailed in chapter 3. Among all the measured sources of variations, lateral movement of the tow was the biggest contributor to gap/overlap causing deviations. The four distributions were later utilized in the statistical modeling efforts. While the AFP head-material combination may change from the one used in the experiment, the methodology and the resulting data are nevertheless expected to provide meaningful insight into the variation characteristics particular to the various industrial AFP implementations.

Another observation made in this thesis is about the relative importance of the position and geometry variations. When position and geometry variations of the same magnitude occur, the defect due to position variation has twice the magnitude of the defect due to geometry variation.

Laminate level statistical predictions

The four distributions obtained by measuring these sources of manufacturing variations were fit with various probability density functions (PDFs). Random samples from these four distribution fits were used to simulate adjacent tow sections. The distribution of predicted gaps from these simulations was compared with the distribution of measured gaps. The location and spread of these distributions were in good agreement. Thus, statistical information from a trial experiment can be useful in predicting the magnitude and frequency of gap and overlap defects caused by manufacturing variations in AFP composite laminates.

By statistically characterizing the measured sources of variation, this thesis demonstrates that both the size and frequency of such defects can be predicted probabilistically. Such simulations successfully connect manufacturing scatter characteristics to defect populations in an AFP composite layup.

Stochastic simulations of AFP tows and laminae

Statistical data about the sources of AFP manufacturing variations was used to predict and resolve mesoscale geometry at the individual tow level. This was achieved by simulating sections of laid tow and assembling them in the tow length direction to construct synthetic tows which are similar to real tows in their in-plane waviness after layup. These simulated tows were used to create virtual laminae with gap and overlap defects which appeared similar to an experimental lamina.

Two methods to simulate the tow were implemented - Monte Carlo (MC) simulations and Markov Chain Monte Carlo (MCMC) simulations. Tows created using the Monte Carlo method had more waviness compared to the observations of real AFP laid tows. This limitation was improved upon in the Markov Chain Monte Carlo simulations which used the Random Walk Metropolis (RWM) method for sampling. This led to simulated tows whose waviness is more realistic than the simulated tows created by random sampling.

The validation efforts for these two methods were done on the tow level and the lamina level. On the tow level, an FFT analysis of the tow centerlines showed spatial-frequency amplitude spectra with acceptable correlation between the experimental tow and the MCMC simulated tow. The MC simulated tow did not match the dominant spatial amplitudes seen in experimental tows. On the lamina level, the gap distributions and the gap area percentage yielded close values for both the MCMC and the MC simulations. However, the MC method led to a simulated lamina with a high number of shorter gaps and no longer gaps. It lacked a match with the experimental observations of the length of defects. The MCMC method led to a closer match with the experimental observations across shorter and longer length of defects. These comparisons also showed that the virtual and experimental lamina equivalence must be established not just in the frequency and magnitude of the defects but also in the length of the defects.

The realistic AFP tows and laminae created by these stochastic simulations are based in experimental reality and are therefore better representative starting geometries for use in process and structural simulations. These representative AFP layups should therefore enable higher accuracy in predicting process and structural phenomena.

Prioritizing process improvements

There are various technological ways to reduce the manufacturing process variations in AFP layups. The robot accuracy can be improved by installing secondary feedback loops or newer robot models with higher path accuracy. The AFP feed system can be improved to reduce the tow lateral movement. The replacement schedules of worn rollers can also play a role. The tow material dimensional specification can be made tighter. Each of these process improvements entails different costs. Thus, another use of the simulation methods described in the preceding sections is in prioritizing these process improvements required in tightening the quality of an AFP layup. These simulations can help understand the effect of the location and spread of the PDFs which describe the various manufacturing variations. For example, it was shown for the AFP head-material combination used in the experiments described earlier that a reduction of the spread tow lateral movement would result in lower levels gap and overlap defects compared to a reduction of the spread of robot inaccuracies or tow widths. These insights enable efficient allocation of resources towards the targeting of AFP process improvements.

Optimal programmed shift

It was demonstrated that virtual AFP laminae generated using MCMC simulations can be used to identify an optimal programmed shift between adjacent tows. The programmed shift represents a trade-off between structural performance knockdowns caused by gap defects and manufacturing rework costs which increase due to overlap defects. An optimal shift minimizing total defect area was identified by quantifying the statistical spread of gap and overlap defect areas across a range of programmed shift values. The stochastic framework captures variability in defect populations, enabling evaluation of uncertainty and scatter relevant to certification and manufacturing allowables. Consequently, the developed approach supports informed process design decisions and reduces reliance on costly physical prototyping during AFP qualification.

Tow lateral movement during steering

After the straight layups, the effect of fiber steering on the tow lateral movement phenomenon was investigated. An experimental campaign was run to measure the tow lateral movement under steering conditions. Data were collected for different steering radii and with two different materials. For both materials, the tow started from its initial position on the compaction roller and gradually moved in the radially outward direction before stabilizing at a position away from the roller center. For both tow materials, the stabilized position for the tow was further away from the roller center when the steering radius was tighter.

Modeling framework for tow lateral movement

An analytical model was developed to explain and predict this tow lateral movement. An analysis of the forces acting on the tow segment after the chute led to the determination of the resultant force. The resultant force on the tow pushes it towards the equilibrium zone from positions on both sides of the zone. This behavior was seen clearly in the tow lateral movement experimental results. This model correctly predicts that the equilibrium zone is further away from the roller center for tighter steering radii. Good correlation was found for one of the materials while the predictions for the other material only matched tests in trend and not in magnitude. The model can also help explain other aspects observed during the tests such as the higher tow position noise in one of the materials.

Defect mitigation strategies in steered layups

A sensitivity analysis was carried out using a reasonable range of values for various process parameters and material properties. The analysis showed that the steering radii, the unsupported tow length from the chute to the compaction roller (UL) and the tow length in contact with only the roller (A) had the most influence on the magnitude of the shift while the tow-roller coefficient of friction, tow-tool coefficient of friction and compaction force had the most influence on the width of the equilibrium zone. This could have utility in the process design for steered AFP components and also in the technology design of the AFP head.

Since the tow lateral movement behavior has been recorded from its initial position to the stabilized position up to the cutoff point, it may be possible to compensate the planned layup path for a VSL in appropriately varying magnitudes and directions to reduce the occurrence of gap and overlap defects during manufacturing.

6.2. Recommendations for future work

Influence of tow start position

It was noted that the starting position of the extended tow before the layup approach can also have a bearing on the defect formation. The limited experimental data did show an average trend of reducing defects across the length of the layup. However, more trials are needed to confirm this behavior.

In section 5.3 which describes the tow lateral movement experimental observations, the starting point is expected to affect the time or length of layup taken to move to the stable region of the compaction roller. However, this too needs more trials to be confirmed as a phenomenon.

Effects of roller wear

During several discussions, most AFP domain peers wondered if the band of wear on the compaction roller channels the tow and keeps it from moving laterally. One the other hand it could be an imperfection which causes noisy lateral movement as the tow enters and exits this minor band of wear which is depressed from the initial cylindrical geometry of the roller. This bug vs feature question remains unanswered and is worthy of a comparative layup experiment with new and worn out compaction rollers.

Extending tow section simulations to multi-tow scenarios

The tow section simulations presented in chapter 4 will need to be enhanced to make the predictive framework more applicable to industrial AFP systems. In such multi-tow systems, the tow lateral movement behavior is expected to differ across the course due to the difference in boundary conditions of the two outside tows in a course as against the inside tows. Therefore, the framework needs to account for the statistical differences in the inter-course interactions and the intra-course interactions. This reformulated simulation will thus sample from separate distributions for the different tows within a course. The sampling for the other three variations can remain unchanged, except that they will be referenced across the individual chute centerline instead of the roller centerline.

Defect interactions within adjacent plies

Chapter 4 presented modeling frameworks to predict the size and frequency of defects in AFP layups. However, it assumed defects in a ply do not interact with adjacent plies. In effect, it neglects out of plane waviness caused in a tow being laid over a substrate region with a defect. In case of a gap, one can expect the tow to wave into the substrate while in case of an overlap we can expect it wave out of the substrate. This waviness is a large cause of structural knockdown. These interactions need to be geometrically or mechanistically modeled to complete the AFP defect description in a laminate.

Defect morphology for varying defect magnitudes

Defect morphology in AFP composites has received significant attention but more so for thermoset material layups where the matrix fills the gap defects. In contrast, defects in ISC-TP AFP layups will persist as-is. Gap defects of varying magnitude can be expected to lead to varying shape and magnitude of voids as seen in figure 6.1. Moreover, the effect of various processing parameters like compaction pressure, temperature and layup speed is not known. The voids in the figure have sharp corners, however, percolation flow can fill the sharp corners and make the void more rounded. This investigation is necessary to understand the variations in defect morphology likely to be seen in an ISC-TP composite part.

Thickness evolution and surface undulations in ISC-TP AFP laminates

Thermoset AFP composite layups on a tool are polymerised in an autoclave under pressure on the bagging material which acts on the air-evacuated layup. This results in a smooth tool side part surface along with a less smooth air side part surface. For some industrial AFP parts, a caul plate or two part tool is used to achieve a smooth surface on both sides of the part while minimizing the undulations from the gaps and overlaps [116].

One of the major advantages of thermoplastic laminates is the ability to cost effectively fasten them by welding. However, welding processes are sensitive to dimensional variations as they affect the contact conditions between the joined parts. Thus the undulations or "waffling" on the air side of ISC-TP parts needs to be investigated to understand the mechanisms of thickness development through a stacking sequence in the presence of defects.

Structural knockdown mechanisms in ISC-TP AFP

Figure 6.1 illustrates the peculiarities of defect morphology in ISC TP composites in contrast to thermoset composites. These are informed by micrographs of such layups with varying magnitudes of defects [117]. When the gap magnitude is small, the void volume is expected to be larger while waviness of the subsequent layers is lower. As the gap magnitude increases, the void gets smaller but the waviness of the subsequent layers is higher. Once the subsequent layers have gone from a bridge configuration to an touchdown contact or a collapsed bridge configuration with extended contact, the void volume is stabilized and the half waves move away from each other. In such scenarios, it is not known if bigger gaps might be more structurally advantageous than smaller gaps.

For thermoset AFP composites, gap defects cause the biggest knockdowns in notched compression properties. Composite coupons with gap defects fail in fiber kinking or inter-laminar failure depending on the degree of waviness. These mechanisms in conjunction with the void and waviness development in ISC-TP AFP composites with varying defect magnitudes has not been investigated yet.

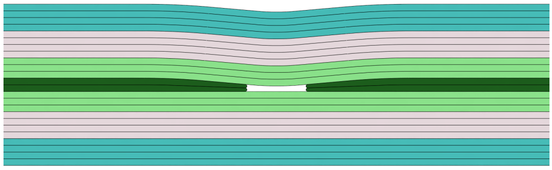

(a)

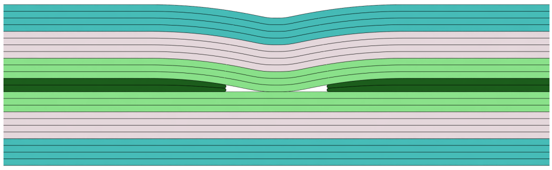

(b)

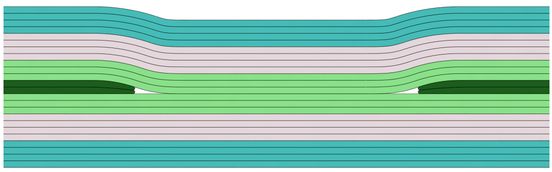

(c)

Figure 6.1: Sectional views of a parametrized CAD geometry of a composite coupon. The sub-figures show the resulting void when a gap defect of increasing magnitude (top to bottom) have subsequent tows laid on it. This CAD geometry was informed by micrographs of real ISC-TP composite coupons. In the top figure (a) the subsequent tow bridges the gap defect. In the middle figure, the tow just touches the bottom layer underneath the gap. In the bottom figure with the biggest gap magnitude, the subsequent tow is in extended contact with the bottom layer underneath the gap.

Tow-to-tow interactions during steering in industrial AFP machines

In multi-tow AFP systems, adjacent tows interact with each other during layup, particularly under steering conditions, which is not captured in single tow experiments. During steering, inner tows are expected to experience larger lateral movements than outer tows, which may lead to tow bunching. The relative time to achieve stable position will also vary between the inner and outer tows. Future work could aim to experimentally observe these effects during fiber steering. Recording the tow lateral movement phenomenon in such machines would require advanced image processing to be able to distinguish between adjacent tows also in scenarios where their edges touch each other or even overlap on the roller. Such interaction between multiple tows on a roller has not been recorded and measured.

Influence of substrate curvature on tow lateral movement

Since AFP manufacturing is widely applied to curved components, future studies can work on extending the work in chapter 3 and chapter 5 to account for curvature in the direction of the layup and also in directions removed from the direction of the layup. Moreover, the analytical model which predicts tow lateral movement will need to be extended for various magnitudes of Gaussian curvature by accounting for the changed shape of the roller and its effects on the magnitude and directions of the tow tension, tow-roller shear force and friction. The proposed model can be viewed as a building block to which additional capability can be added, relatively easily, as required by the complexity of the part being made and the machine being used.

Dynamic aspects of tow lateral movement

The analytical model presented in section 5.4 predicts the lateral movement behavior after it has stabilized. The model does not take into account the past values of tow lateral movement to predict the future values. The dynamic aspects of the observed phenomenon could be explored in future works as well. This could thus lead to predictions for the phase of the layup before it reaches the stable regions or even after cutoff.

Tow characterization and model domain expansion

The characterization of the Young's modulus, shear modulus and friction coefficients for various tow materials would be valuable for accurate structural modeling of tow behavior during layup because such models rely on physical and contact property data.

Moreover, further trials with tow lateral movement measurements during layup could use a broader range of process conditions to grow the model's domain beyond the scope of this investigation. These may include a range of layup speeds, compaction pressures and tow dimensions. The layup could also be done with varying magnitudes and directions of steering radii in a single layup path to understand the stabilization behavior and time over an arc length.

Toolpath offsets and online correction for steered layups

Section 5.5.2 discussed some ideas for implementing offsets of steered toolpaths to reduce the occurrence of defect formation due to tow lateral movement. Future work could look into testing these offset toolpaths in proof of concept trials involving few common tow materials. Long term work would involve integrating these offset rules into CAM software used to program layups.

Enhanced AFP CAM software

Current CAM software used for AFP robot programming relies on nominal definitions of the tow width and thickness when generating layup toolpaths on a mold or tool surface. As a result, manufacturing variability in both the width and thickness directions is not captured. Variations in tow width lead to coverage variations and therefore gaps and overlaps as demonstrated in this thesis. These in-plane coverage defects induce out-of-plane waviness, resulting in a laminate whose tool side is smooth and flat while the air side exhibits undulations. Tow thickness variability further affects local compaction behavior, as compaction pressure depends on the tool center point (TCP) depth relative to the assumed substrate plane.

Future CAM software could incorporate enhanced programming capabilities that explicitly account for statistical variations in tow geometry. By adaptively modifying toolpaths and compaction parameters based on expected tow width and thickness distributions, such approaches could reduce defect occurrence.

Current CAM software already supports export of layup geometry and defect information to structural analysis tools. These exports could be made more representative by replacing nominal tow definitions with realistic tow geometries generated using the statistical modeling methods developed in this thesis. Such an integrated digital thread would enable more accurate process and structural simulations that account for as-manufactured stochasticity.

Cost models combining AFP manufacturing and structural efficiency

Existing cost models for aerostructure manufacturing processes are largely decoupled from composite structural efficiency calculations. However, in case of AFP layups, the manufacturing process parameters like tighter steering radii, lower programmed shifts and low allowable defect magnitudes are linked to lower production rates due to the frequent stops for repair and rework. Steering enabled variable stiffness and the frequency of defects on the other hand will affect laminate sizing and final part weight.

Future cost models could therefore combine process-dependent defect statistics, their associated structural knockdowns and the resulting impact on laminate sizing. This enables trade-offs between manufacturing efficiency and structural performance that reduce overall aerostructure lifecycle cost. These cost models might also help in reducing overregulation by the methods departments in original equipment manufacturers.

Defect-aware postprocessing strategies for AFP composites

Thermoplastic AFP parts require post-processing to reduce defect severity and improve consolidation. Such post-processing steps introduce elevated temperature and/or pressure via oven heating, heated tooling, vacuum over-bagging, or short autoclave cycles. The duration of exposure to elevated temperature or pressure required to reduce defect severity is expected to depend on the frequency, magnitude and length of defects present in the layup. Future work could therefore investigate the relationship between the post-processing cycle length and the defect population characteristics.

References

[1] Evtol news, *Supernal (Hyundai Motor Group) S-A1 (concept design)*. Available online: URL.

[2] Boeing Images, *777-8 Standard View Illustration*. Available online: URL.

[3] Wikimedia Commons, *Studie des Airbus A400M für die Luftwaffe*, 2007. Available online: URL.

[4] Delta Airlines, *Airbus A220-100*. Available online: URL.

[5] A. David Zahn *et al.*, "UAM Instrument Flight Procedure Design and Evaluation in the Joby Flight Simulator", 2023.

[6] Lilium GmbH, *Lilium jet*. Available online: URL.

[7] *GeminiJets Incorporated/Airliners Distributing, Inc.* Available online: URL.

[8] *Aircraft illustration by Norebbo.com*. Available online: URL.

[9] R. Jones. CRC Press, 1999, ISBN: 9781315272986. DOI: `https://doi.org/10.1201/9781498711067`.

[10] C. Kassapoglou, *Design and Analysis of Composite Structures*. 2010, ISBN: 9780470972632. DOI: `10.2514/4.867804`.

[11] W. Yu, *Multiscale structural mechanics*. John Wiley & Sons Inc, 2025, ISBN: 9781119092674.

[12] Toray Carbon Fibers America, *Torayca T800H Technical Data Sheet*, High-performance intermediate-modulus carbon fiber used in aerospace structures, 2023. Available online: URL.

[13] Toray Carbon Fibers America, *Torayca M60J Technical Data Sheet*, High-modulus carbon fiber for spacecraft and satellite structures, 2023. Available online: URL.

[14] Owens Corning, *E-Glass and S-Glass Fibers: Material Data Sheets*, Typical properties of E-, S-, and D-glass reinforcement fibers, 2022. Available online: URL.

[15] DuPont, *Kevlar 49 Aramid Fiber Technical Guide*, Typical mechanical and thermal properties of Kevlar 49 aramid fibers, 2023. Available online: URL.

[16] "Composite materials handbook, volume 2: Polymer matrix composites - materials properties", U.S. Department of Defense, Tech. Rep. MIL-HDBK-17-2F, 1999.

[17] S.-J. Park, *Carbon Fibers* (Springer Series in Materials Science). Springer Singapore, 2018, vol. 210, ISBN: 978-981-13-0538-2. DOI: `10.1007/978-981-13-0538-2`. Available online: URL.

[18] R. Harik and A. Brasington, *Automated Fiber Placement : Status, Challenges, and Evolution*. Warrendale, Pennsylvania: SAE International, 2025, ISBN: 9781468603057; 9781468603064; 9781468603071. Available online: URL.

[19] CompositesWorld, *GKN Aerospace, Joby Aviation sign aerostructures agreement*, Online; accessed 2026-01-06, 2023. Available online: URL.

[20] M. O. Kenward, *Composites take off*, Ingenia, Royal Academy of Engineering; accessed 2026-01-06, Sep. 2019. Available online: URL.

[21] SimpleFlying, *The MC-21 Wing — Why It's a World's First*, Online; accessed 2026-01-06, Nov. 2021. Available online: URL.

[22] Stratview Research, "Aircraft AFP / ATL Composites Market Trend, Forecast, Competitive Analysis, and Growth Opportunity: 2019-2024", no. January, pp. 2019–2024, 2019.

[23] Boeing Images, *787-10 Standard View Illustrations*. Available online: URL.

[24] Red Bubble, *Airbus A320 with Winglets*. Available online: URL.

[25] Avions Legendaires, *Airbus Helicopters H145*. Available online: URL.

[26] Wikipedia Commons, *Three-way view of the Lockheed Martin F-35A Lightning II.* Available online: URL.

[27] The Complete Encyclopedia of World Aircraft, *Sikorsky S-65 / CH-53 Sea Stallion, 1962*, 1997. Available online: URL.

[28] Embraer commercial aviation, *An aircraft that redefines regional aircraft*. Available online: URL.

[29] SAMXL, STUNNING, *Thermoplastics composite fuselage assembly*. Available online: URL.

[30] ADD Composites, *Identifying the Pain Points: "Navigating the Complexities of Aerostructure Manufacturing"*. Available online: URL.

[31] Collins Aerospace, *Flight Control Surfaces Enhanced mission capabilities through advanced technologies*. Available online: URL.

[32] J. Blackman, *Lockheed Martin opens new smart manufacturing facility in California*, 2021. Available online: URL.

[33] S. Black, *Improving composites processing with automated inspection*, 2018. Available online: URL.

[34] Spirit Aerosystems, *Advanced Composite Fabrication*. Available online: URL.

[35] A350 XWB News, *32-meter invar tools for A350 wing covers.* 2015. Available online: URL.

[36] R. Harik, C. Saidy, S. J. Williams, Z. Gurdal, and B. Grimsley, "Automated fiber placement defect identity cards: Cause, anticipation, existence, significance, and progression", *International SAMPE Technical Conference*, vol. 2018-May, 2018.

[37] C. Sacco *et al.*, "On the effect of manual rework in AFP quality control for a doubly-curved part", *Composites Part B: Engineering*, vol. 227, no. October, p. 109 432, 2021, ISSN: 13598368. DOI: `10.1016/j.compositesb.2021.109432`. Available online: URL.

[38] S. McArthur, J. Mehnen, C. Yokan, and I. Bomphray, "An overview of current research in automated fibre placement defect rework", *Procedia Computer Science*, vol. 232, no. 2023, pp. 2167–2180, 2024, ISSN: 18770509. DOI: `10.1016/j.procs.2024.02.036`. Available online: URL.

[39] T. Rudberg, J. Nielson, M. Henscheid, and J. Cemenska, "Improving AFP Cell Performance", *SAE International Journal of Aerospace*, vol. 7, no. 2, pp. 317–321, 2014, ISSN: 19463901. DOI: 10.4271/2014-01-2272.

[40] Hexcel Corporation, *Hexcel presentation in SEC 14A definitive proxy statement*. Available online: URL.

[41] M. Kaufmann, D. Zenkert, and P. Wennhage, "Integrated cost/weight optimization of aircraft structures ", *Structural and Multidisciplinary Optimization*, vol. 41, no. 2, pp. 325–334, 2010, ISSN: 1615-1488. DOI: 10.1007/s00158-009-0413-1. Available online: URL.

[42] J. Sloan, "Large, high-volume, infused composite structures on the aerospace horizon", *CompositesWorld*, 2019. Available online: URL.

[43] J. Sloan, "Evolving AFP for the next generation", *CompositesWorld*, 2019. Available online: URL.

[44] Coriolis Composites, *Coriolis Industry References*, 2024. Available online: URL.

[45] Y. C. Roth *et al.*, "Cleansky2/ Clean Aviation Large Passenger Aircraft for More Sustainable Commercial Fuselage Technologies–Major Achievements", *ICAS Proceedings*, pp. 1–20, 2024, ISSN: 29584647.

[46] R. Young and H. P. Manager, "NASA Hi-Rate Composite Aircraft Manufacturing (HI-CAM) project overview and other related topics: U.S. Aviation Climate Action Plan (2021)", pp. 1–23,

[47] R. Dakota, S. Jansen, K. Antcliff, *et al.*, "Urban Air Mobility (UAM) Concept of Operations", NASA, Tech. Rep., 2020, NASA Technical Report. Available online: URL.

[48] TORAY Industries, "From 200 to 200,000: Challenges in Advanced Air Mobility Market Scaling", Toray UAM/AAM Solutions, White Paper, 2020, Accessed: 2025-12-11. Available online: URL.

[49] D. Del Rossi, V. Cadran, P. Thakur, M. Palardy-Sim, M. Lapalme, and L. Lessard, "Experimental investigation of the effect of half gap/half overlap defects on the strength of composite structures fabricated using automated fibre placement (AFP)", *Composites Part A: Applied Science and Manufacturing*, vol. 150, no. May, p. 106 610, 2021, ISSN: 1359835X. DOI: 10.1016/j.compositesa.2021.106610. Available online: URL.

[50] J. P. Belnoue *et al.*, "Understanding and predicting defect formation in automated fibre placement pre-preg laminates", *Composites Part A: Applied Science and Manufacturing*, vol. 102, pp. 196–206, 2017, ISSN: 1359835X. DOI: 10.1016/j.compositesa.2017.08.008. Available online: URL.

[51] D. H. Lukaszewicz, C. Ward, and K. D. Potter, "The engineering aspects of automated prepreg layup: History, present and future", *Composites Part B: Engineering*, vol. 43, no. 3, pp. 997–1009, 2012, ISSN: 13598368. DOI: 10.1016/j.compositesb.2011.12.003. Available online: URL.

[52] W. E. Guin, J. R. Jackson, and C. M. Bosley, "Effects of tow-to-tow gaps in composite laminates fabricated via automated fiber placement", *Composites Part A: Applied Science and Manufacturing*, vol. 115, pp. 66–75, Dec. 2018, ISSN: 1359-835X. DOI: 10.1016/J.COMPOSITESA.2018.09.014.

[53] M. Ghayour, R. Ganesan, and M. Hojjati, "Flexural response of composite beams made by Automated Fiber Placement process: Effect of fiber tow gaps", *Composites Part B: Engineering*, vol. 201, no. April, p. 108 368, 2020, ISSN: 13598368. DOI: 10.1016/j.compositesb.2020.108368. Available online: URL.

[54] M. Mayer, A. Schuster, L. Brandt, D. Deden, and F. Fischer, "Integral Quality Assurance Method for a CFRP Aircraft Fuselage Skin: Gap and Overlap Measurement for Thermoplastic AFP", in *Flexible Automation and Intelligent Manufacturing (FIAM 2023)*, 2023, pp. 525–534. DOI: https://doi.org/10.1007/978-3-031-38241-3_59.

[55] A. van Grootel, J. Chang, B. L. Wardle, and E. Olivetti, "Manufacturing variability drives significant environmental and economic impact: The case of carbon fiber reinforced polymer composites in the aerospace industry", *Journal of Cleaner Production*, vol. 261, p. 121 087, 2020, ISSN: 09596526. DOI: 10.1016/j.jclepro.2020.121087. Available online: URL.

[56] A. M. Mendes Florindo, "LayLa: An open-source offine programming framework for com-posite deposition", 2020. Available online: URL.

[57] B. Greenway, "Robot accurary", in *Industrial Robot*, 4, vol. 27, Emerald Group Publishing Ltd., 2000, pp. 257–265. DOI: 10.1108/01439910010372136.

[58] S. Rajan, M. A. Sutton, S. Sockalingam, W. McMakin, Z. Gurdal, and A. Kidane, "Simulations and experiments for automated fiber placement of prepreg slit tape: Wrinkle formation and fundamental observations", *Composites Part B: Engineering*, vol. 201, no. January, p. 108 287, 2020, ISSN: 13598368. DOI: 10.1016/j.compositesb.2020.108287. Available online: URL.

[59] J. van Kollenburg, "The Effects of Local Fibre Steering", 2022, pp. 3333–3336, ISBN: 0780344286. Available online: URL.

[60] S. Agarwal, "Width deformation of thermo- plastic prepreg tapes during in- situ Automated Fiber Placement", Delft University of Technology, 2023. Available online: URL.

[61] P. D. Juarez and E. D. Gregory, "In Situ Thermal Inspection of Automated Fiber Placement for manufacturing induced defects", *Composites Part B: Engineering*, vol. 220, no. January, p. 109 002, 2021, ISSN: 13598368. DOI: 10.1016/j.compositesb.2021.109002. Available online: URL.

[62] M. Mussatayev, Q. Yi, M. Fitzgerald, V. K. Maes, P. Wilcox, and R. Hughes, "Directional eddy current probe configuration for in-line detection of out-of-plane wrinkles", *Composites Part B: Engineering*, vol. 268, no. August 2023, p. 111 048, 2024, ISSN: 13598368. DOI: 10.1016/j.compositesb.2023.111048. Available online: URL.

[63] M. Rivard *et al.*, "Enabling responsive real-time inspection of the automated fiber placement process", *International SAMPE Technical Conference*, vol. 2020-June, 2020. DOI: 10.33599/s.20.0258.

[64] G. Nehls, "Fives introduces COAST in-process composite inspection technology", *CompositesWorld*, Oct. 2023. Available online: URL.

[65] N. Yadav and R. Schledjewski, "Inline tape width control for thermoplastic automated tape layup", *Composites Part A: Applied Science and Manufacturing*, vol. 163, Dec. 2022, ISSN: 1359835X. DOI: 10.1016/J.COMPOSITESA.2022.107267.

[66] D. Peeters, P. Quenzel, L. Netzband, A. M. Florindo, S. Hesseler, and T. Gries, “Predicting the formation of gaps and overlaps due to width variations of dry-fiber tapes during automated fiber placement”, in *ACM5 : Fifth International Symposium on Automated Composites Manufacturing*, 2022. Available online: URL.

[67] I. Tretiak *et al.*, “Real-time material measurement for automated fibre placement”, in *20th European Conference on Composite Materials - Composites Meet Sustainability*, vol. 2, 2022, pp. 25–31. DOI: 10.5075/epfl-298799_978-2-9701614-0-0. Available online: URL.

[68] H. Ghayoor, F. Shadmehri, and S. Van Hoa, “Development of experimental technique for measuring strain and deformation in manufacturing of thermoplastic composites using Automated Fiber Placement (AFP)”, in *SAMPE 2014 | SEATTLE, WA*, 2014. Available online: URL.

[69] M. Uhart, O. Patrouix, Y. Aoustin, and J. Canou, “Improving accuracy in robotized fiber placement”, *ICCM International Conferences on Composite Materials*, vol. 2013-July, pp. 778–786, 2013.

[70] G. De Itzel Ojeda Jesus, O. Patrouix, and Y. Aoustin, “Dynamic Tool Center Point (DTCP) implementing in Automated Fiber Placement (AFP)”, in *The third International Symposium on Automated Composites Manufacturing (ACM3)*, 2017. Available online: URL.

[71] K. A. Jeffries, “Enhanced Robotic Automated Fiber Placement with Accurate Robot Technology and Modular Fiber Placement Head”, *SAE International Journal of Aerospace*, vol. 6, no. 2, pp. 774–779, 2013, ISSN: 19463901. DOI: 10.4271/2013-01-2290.

[72] T. Rudberg, “Increasing Machine Accuracy by Spatially Compensating Large Scale Machines for Use in Constructing Aerospace Structures”, *SAE International Journal of Aerospace*, vol. 6, no. 1, pp. 2013–01–2298, Sep. 2013, ISSN: 1946-3901. DOI: 10.4271/2013-01-2298. Available online: URL.

[73] M. Bock, M. Perner, C. Krombholz, and B. Beykirch, “Relation between repeatability and speed of robot-based systems for composite aircraft production through multilateration sensor system”, in *Sensors and Smart Structures Technologies for Civil, Mechanical, and Aerospace Systems 2015*, vol. 9435, SPIE, Mar. 2015, 94352G, ISBN: 9781628415384. DOI: 10.1117/12.2083846.

[74] L. Cheng, L. Zhang, J. Li, and Y. Ke, “Measurement, identification, and compensation of pose errors for six-axis gantry automated fiber placement machine”, *International Journal of Advanced Manufacturing Technology*, vol. 120, no. 3-4, pp. 2259–2276, May 2022, ISSN: 14333015. DOI: 10.1007/s00170-021-08373-9.

[75] X. Xu, L. Cheng, Y. Guo, J. Li, and Y. Ke, “A Modeling and Calibration Method of Heavy-Duty Automated Fiber Placement Robot Considering Compliance and Joint-Dependent Errors”, *Journal of Mechanisms and Robotics*, vol. 15, no. 6, pp. 61 011–61 012, Dec. 2023, ISSN: 1942-4302. DOI: 10.1115/1.4056405. Available online: URL.

[76] N. Niknafs Kermani, V. Gargitter, P. Simacek, and S. G. Advani, “Gap filling mechanisms during the thin ply Automated Tape Placement process”, *Composites Part A: Applied Science and Manufacturing*, vol. 147, no. April, p. 106 454, 2021, ISSN: 1359835X. DOI: 10.1016/j.compositesa.2021.106454. Available online: URL.

[77] P. Simacek, N. Niknafs Kermani, V. Gargitter, and S. G. Advani, “Role of resin percolation in gap filling mechanisms during the thin ply thermosetting automated tape placement process”, *Composites Part A: Applied Science and Manufacturing*, vol. 152, no. September 2021, p. 106 677, 2022, ISSN: 1359835X. DOI: 10.1016/j.compositesa.2021.106677. Available online: URL.

[78] V. C. Jamora, V. Rauch, S. G. Kravchenko, and O. G. Kravchenko, “Effect of Resin Bleed Out on Compaction Behavior of the Fiber Tow Gap Region during Automated Fiber Placement Manufacturing”, *Polymers*, vol. 16, no. 1, 2024, ISSN: 20734360. DOI: 10.3390/polym16010031.

[79] “Prediction of the in-plane permeability and air evacuation time of fiber-placed thermoplastic composite preforms with engineered intertape channels”, *Composites Part C: Open Access*, vol. 14, no. April, p. 100 475, 2024, ISSN: 26666820. DOI: 10.1016/j.jcomc.2024.100475. Available online: URL.

[80] S. Khaleghi, J. G. Kirchhoff, J. Pandher, J. Lacalle, and M. Tehrani, “Efficient consolidation of thermoplastic composites using AFP-engineered air channels and optimized VBO processing”, *Composites Part B: Engineering*, vol. 310, p. 113 134, 2026, ISSN: 1359-8368. DOI: https://doi.org/10.1016/j.compositesb.2025.113134. Available online: URL.

[81] K. Fayazbakhsh, M. Arian Nik, D. Pasini, and L. Lessard, “Defect layer method to capture effect of gaps and overlaps in variable stiffness laminates made by Automated Fiber Placement”, *Composite Structures*, vol. 97, pp. 245–251, 2013, ISSN: 02638223. DOI: 10.1016/j.compstruct.2012.10.031. Available online: URL.

[82] “Experimental and numerical investigation on the open-hole compressive strength of AFP composites containing gaps and overlaps”, *Journal of Composite Materials*, vol. 51, no. 26, pp. 3631–3646, 2017, ISSN: 1530793X. DOI: 10.1177/0021998317690917.

[83] A. J. Sawicki and P. J. Minguet, “Effect of intraply overlaps and gaps upon the compression strength of composite laminates”, *Collection of Technical Papers - AIAA/ASME/ASCE/AHS/ASC Structures, Structural Dynamics and Materials Conference*, vol. 1, pp. 744–754, 1998, ISSN: 02734508. DOI: 10.2514/6.1998-1786.

[84] D. D. Rossi, “Effect of Half Gap/Overlap Defects on the Strength of Composite Structures Fabricated with Automated Fiber Placement Methods”, Ph.D. dissertation, McGill University, 2019.

[85] F. Diemar *et al.*, “X-ray micro-computed tomography for mechanical behaviour analysis of Automated Fiber Placement (AFP) laminates with integrated gaps and overlaps”, *Composite Structures*, vol. 351, no. June 2024, p. 118 601, 2025, ISSN: 02638223. DOI: 10.1016/j.compstruct.2024.118601. Available online: URL.

[86] X. Li, S. R. Hallett, and M. R. Wisnom, “Modelling the effect of gaps and overlaps in automated fibre placement (AFP)-manufactured laminates”, *Science and Engineering of Composite Materials*, vol. 22, no. 2, pp. 115–129, 2015, ISSN: 21910359. DOI: 10.1515/secm-2013-0322.

[87] Q. Chen *et al.*, “Modeling on the effect of automated fiber placement induced gaps in curved composite laminates”, *Composite Structures*, vol. 328, no. October 2023, p. 117 721, 2024, ISSN: 02638223. DOI: 10.1016/j.compstruct.2023.117721. Available online: URL.

[88] P. Ribeiro, H. Akhavan, A. Teter, and J. Warmiński, “A review on the mechanical behaviour of curvilinear fibre composite laminated panels”, *Journal of Composite Materials*, vol. 48, no. 22, pp. 2761–2777, 2014, ISSN: 1530793X. DOI: 10.1177/0021998313502066.

[89] G. G. Lozano, A. Tiwari, C. Turner, and S. Astwood, “A review on design for manufacture of variable stiffness composite laminates”, *Proceedings of the Institution of Mechanical Engineers, Part B: Journal of Engineering Manufacture*, vol. 230, no. 6, pp. 981–992, 2016, ISSN: 20412975. DOI: 10.1177/0954405415600012.

[90] A. Beakou, M. Cano, J. B. Le Cam, and V. Verney, “Modelling slit tape buckling during automated prepreg manufacturing: A local approach”, *Composite Structures*, vol. 93, no. 10, pp. 2628–2635, 2011, ISSN: 02638223. DOI: 10.1016/j.compstruct.2011.04.030. Available online: URL.

[91] M. Y. Matveev, P. J. Schubel, A. C. Long, and I. A. Jones, “Understanding the buckling behaviour of steered tows in Automated Dry Fibre Placement (ADFP)”, *Composites Part A: Applied Science and Manufacturing*, vol. 90, pp. 451–456, 2016, ISSN: 1359835X. DOI: 10.1016/j.compositesa.2016.08.014. Available online: URL.

[92] M. Belhaj and M. Hojjati, “Wrinkle formation during steering in automated fiber placement: Modeling and experimental verification”, *Journal of Reinforced Plastics and Composites*, vol. 37, no. 6, pp. 396–409, 2018, ISSN: 15307964. DOI: 10.1177/0731684417752872.

[93] R. Wehbe, R. Harik, and Z. Gürdal, “In-plane tow deformations due to steering in automated fiber placement”, *AIAA Scitech 2019 Forum*, no. January, pp. 1–13, 2019. DOI: 10.2514/6.2019-1271.

[94] N. Bakhshi and M. Hojjati, “Time-dependent wrinkle formation during tow steering in automated fiber placement”, *Composites Part B: Engineering*, vol. 165, no. October 2018, pp. 586–593, 2019, ISSN: 13598368. DOI: 10.1016/j.compositesb.2019.02.034. Available online: URL.

[95] A. Nedelcu *et al.*, “The influence of tow tackiness on tow pull-up during the manufacturing of a composite pressure vessel”, *Manufacturing Letters*, vol. 40, pp. 132–135, 2024, ISSN: 22138463. DOI: 10.1016/j.mfglet.2024.03.011. Available online: URL.

[96] N. Bakhshi and M. Hojjati, “An experimental and simulative study on the defects appeared during tow steering in automated fiber placement”, *Composites Part A: Applied Science and Manufacturing*, vol. 113, pp. 122–131, Oct. 2018, ISSN: 1359835X. DOI: 10.1016/j.compositesa.2018.07.031. Available online: URL.

[97] Y. Wang, S. Mahapatra, J. P.-H. Belnoue, D. S. Ivanov, and S. R. Hallett, “Modelling the effect of process conditions on steering-induced defects in automated fibre placement (AFP)”, *Composites Part A: Applied Science and Manufacturing*, vol. 173, no. May, p. 107 702, 2023, ISSN: 1359835X. DOI: 10.1016/j.compositesa.2023.107702. Available online: URL.

[98] R. Wehbe, C. Sacco, A. Baz Radwan, M. Albazzan, and R. Harik, “Influence of process parameters in AFP fiber steering on cylinders: Constant curvature paths”, *Composites Part C: Open Access*, vol. 2, no. June, p. 100 036, 2020, ISSN: 26666820. DOI: 10.1016/j.jcomc.2020.100036. Available online: URL.

[99] L. Füssel, T. A. Cender, V. Austermann, J. W. Gillespie, and D. Heider, "Tow Steering of Stretchable Tuff Thermoplastic Tape With Laser Tape Placement", *International SAMPE Technical Conference*, vol. 2022-May, no. 2, 2022. DOI: 10.33599/nasampe/s.22.0756.

[100] A. Legenstein, L. Füssel, D. Heider, J. W. Gillespie, and T. A. Cender, "Stretch-steering of highly aligned discontinuous fiber tape with automated fiber placement", *Composites Part B: Engineering*, vol. 287, no. August, p. 111 801, 2024, ISSN: 13598368. DOI: 10.1016/j.compositesb.2024.111801. Available online: URL.

[101] L. Raps, A. Chadwick, D. Fricke, and Y. Schäfer, "Steering limitations for in-situ automated fibre placement manufactured structures", in *ICCM23*, DLR.

[102] ADD Composites, *ADD Composites (Espoo, Finland) website*. Available online: URL (visited on 04/20/2023).

[103] Hexagon, *Laser Tracker Fundamentals (11400-00-00)*. Available online: URL (visited on 04/20/2023).

[104] Hexagon AB, *Leica Absolute Tracker AT960*. Available online: URL.

[105] Ximea, *Ximea xiC Camera*. Available online: URL (visited on 04/20/2023).

[106] D. H. Nguyen, X. Sun, I. Tretiak, M. A. Valverde, and J. Kratz, "Automatic process control of an automated fibre placement machine", *Composites Part A: Applied Science and Manufacturing*, vol. 168, p. 107 465, May 2023, ISSN: 1359-835X. DOI: 10.1016/J.COMPOSITESA.2023.107465.

[107] Micro-Epsilon Messtechnik GmbH & Co. KG, *scanCONTROL 30x0*. Available online: URL (visited on 04/20/2023).

[108] S. Pantoji, C. Kassapoglou, and D. Peeters, "Measuring Sources of Manufacturing Process Variations in Automated Fiber Placement Composites", in *Twenty-third international conference on composite materials (ICCM23)*, Belfast, Ireland, 2023. Available online: URL.

[109] D. King, "Automated Fibre Placement of Ox-Ox CMCs", in *23rd International Conference on Composite Materials*, 2023. Available online: URL.

[110] V. C. Jamora, C. M. Sherin, S. Dong, B. Bhattacharjee, K. Kaipa, and O. G. Kravchenko, "The effect of prepreg laminate thickness on transverse fiber tow deformation during the deposition of afp composites", *Composites Part A: Applied Science and Manufacturing*, vol. 201, p. 109 443, 2026, ISSN: 1359-835X. DOI: https://doi.org/10.1016/j.compositesa.2025.109443. Available online: URL.

[111] N. Metropolis, A. W. Rosenbluth, M. N. Rosenbluth, A. H. Teller, and E. Teller, "Equation of state calculations by fast computing machines", *The Journal of Chemical Physics*, vol. 21, no. 6, pp. 1087–1092, 1953.

[112] S. Pantoji, C. Kassapoglou, and D. Peeters, "Predicting gaps and overlaps in automated fiber placement composites by measuring sources of manufacturing process variations", *Composites Part B: Engineering*, vol. 291, p. 111 891, 2025, ISSN: 1359-8368. DOI: https://doi.org/10.1016/j.compositesb.2024.111891. Available online: URL.

[113] W. Yu, "Common Misconceptions on Rules of Mixtures for Predicting Elastic Properties of Composites", *AIAA Journal*, vol. 62, no. 5, pp. 1982–1987, 2024, ISSN: 1533385X. DOI: 10.2514/1.J063863.

[114] S. Liu, J. Sinke, and C. Dransfeld, “An inter-ply friction model for thermoset based fibre metal laminate in a hot-pressing process”, *Composites Part B: Engineering*, vol. 227, no. June, p. 109 400, 2021, ISSN: 13598368. DOI: 10.1016/j.compositesb.2021.109400. Available online: URL.

[115] C. Pasco, M. Khan, J. Gupta, and K. Kendall, “Experimental investigation on interply friction properties of thermoset prepreg systems”, *Journal of Composite Materials*, vol. 53, no. 2, pp. 227–243, 2019, ISSN: 1530793X. DOI: 10.1177/0021998318781706.

[116] M. Lan, D. Cartié, P. Davies, and C. Baley, “Microstructure and tensile properties of carbon – epoxy laminates produced by automated fibre placement : Influence of a caul plate on the effects of gap and overlap embedded defects”, *Composites Part A*, vol. 78, pp. 124–134, 2015, ISSN: 1359-835X. DOI: 10.1016/j.compositesa.2015.07.023. Available online: URL.

[117] J. Öge, “Morphology of Gaps and Overlaps in ISC-AFP Composites”, Master’s thesis, Delft University of Technology, Delft, The Netherlands, 2025.

Acknowledgements

First and foremost, I am deeply grateful to Dr. Daniël Peeters and Dr. Christos Kassapoglou, who together formed an exceptional supervisor–promoter team. They were genuinely invested in my research and cared for my well-being. I consider myself truly fortunate to have had them as mentors.

Daniël's foresight in identifying critical bottlenecks greatly helped in planning and maintaining steady progress towards the timely completion of this thesis. He led by example through his impressive productivity and commitment to his own research. Always available for scientific guidance, he made it a point to be present for important milestones and events. His relaxed and approachable demeanor brought a calm, positive energy to our meetings and helped me keep smiling through the challenging moments. I will always value his example of excellence, efficiency, and humility.

Christos is an inspiring composites expert whose deep knowledge and broad perspective have been my north star. His ability to balance demanding industrial and academic responsibilities while still offering thoughtful, timely feedback on our manuscripts was truly remarkable. Christos bridges the worlds of academic inquiry and industrial application, and I hope to emulate that balance one day. His fascinating stories always made for interesting conversations about the aerospace industry. In many ways, he has been a mirror to my own passion for composites and aerospace.

I am sincerely thankful to all my colleagues from the Faculty of Aerospace Engineering and SAM | XL who contributed to my research and experiments. André Mendes Florindo, our automation engineer, deserves special mention for patiently teaching me how to operate the AFP robotic cell and for his kind and pleasant company. Daniel Atherstone supported me with high-quality, methodical CAD models for various parts and composite laminates essential to my work. His creativity and attention to detail are also beautifully reflected on the cover of this thesis. I would also like to thank Sungi Han and Henry Weng for their invaluable assistance during my experiments.

I am equally grateful to my students from the AE2224 Test, Analysis & Simulation course - Clifton-John Walle, Martijn van der Voort, Séan McCarthy, Manuel Cruz, Diogo Ying, and Giovanni Zattoni and to my MSc thesis student Joep Öge for being such dedicated student-researchers and for reminding me how deeply fulfilling teaching can be.

My colleagues from the Automated Fiber Placement field - Avyadhish, Lieth, Emma, Gamar, Alex and Kasahun - thank you for all the specialist talk which was not possible with anyone else at the faculty.

My journey in composites began with two hands-on graduate courses, AAE 590 Manufacturing of Advanced Composite Materials and MSE 597 Experimental Characterization of Advanced Composite Materials, taught by the inspiring Dr. Byron Pipes. The CMSC Laboratory was an incredible place to learn, thanks to the guidance of Dr. Pipes and Dr. Goodsell, whose mentorship shaped my foundational understanding of the field. I am also grateful to Dr. Kuldeep Mahajan and Dr. Appasaheb Keste for their steady support to my academic and extracurricular pursuits during my undergraduate years.

This acknowledgment would be incomplete without heartfelt thanks to some exceptional teachers who guided me throughout my educational path. My wonderful science teacher, Mr. Nandu Phadke, demonstrated science rather than merely teaching it. He valued curiosity over grades, and his encouragement of the (sometimes exploding!) machines I built in high school helped the shy, awkward, and often-bullied kid I once was find a little confidence. Another key figure in nurturing my early passion for aerospace was my aeromodelling teacher, Mr. Madhav Khare, who introduced me to hands-on work with various tools and lightweight materials. Those early lessons built the foundation for my comfort in designing and executing complex experimental projects.

I would also like to thank my office mates, Srikanth, Shreyas, Victor, Roderick, Guido and Hauke, for creating a friendly and lively environment. Srikanth's company was especially enjoyable; our conversations about life, academia and AI were a constant source of reflection and laughter. Behind his unserious demeanor and frequent roasting was one of the most thoughtful and supportive colleague and well-wisher. Shreyas was the ideal office mate for long discussions on military aviation, defense, and geopolitics, topics we both loved exploring.

It was also a pleasure to interact with and learn from many senior staff members - Julien, Sergio, John-Alan, Julie, Otto, Jurij, Roger, Saullo, Berthil and many others. Laura was especially helpful during my onboarding and made me feel that I belonged. I am also thankful to Roeland, Jos, and Gemma for collaborating with me on the memorable faculty beautification project with aerospace-themed posters.

I must not forget the cheerful company at lunch breaks and at coffee stations - Nikhil, Gargi, Ivan, Ilias, Burhan, Arne, Abhas, Andres, Natalia, Xavier, Stefan, Guru, Sam, Shardul and Panos. I truly appreciate all my colleagues for the discussions, shared experiences and moments of levity that made this journey memorable. While the list of wonderful colleagues, friends and mentors who deserve mention is far longer than this page can hold, I look forward to expressing my thanks to each of you in person.

On a deeply personal note, I wish to thank my parents for their unwavering love and calming presence. Their belief in me has meant more than words can express. Finally, my profound gratitude goes to my wife whose immeasurable support has been the greatest pillar of my success here.

Research Dissemination

Journal publications

- *Predicting gaps and overlaps in automated fiber placement composites by measuring sources of manufacturing process variations.* Composites Part B: Engineering, 2025; Vol. 291.
- *Generating realistic estimates of AFP tow geometry for gap and overlap predictions.* Composites Part A: Applied Science and Manufacturing, 2026; In press.
- *Tow lateral movement at the compaction roller during Automated Fiber Placement composite layup under steering conditions.* Manuscript under review.

Conference proceedings

- *Measuring sources of manufacturing process variations in Automated Fiber Placement composites.* 23rd International Conference on Composite Materials, Belfast, United Kingdom. (ICCM, 2023)
- *Tape at the compaction roller while steering : Does it move laterally?* 6th International Symposium on Automated Composites Manufacturing, Columbia, South Carolina, USA. (ACM6, 2024)
- *Improving AFP process design using Markov Chain Monte Carlo simulations of laid tows.* 7th International Symposium on Automated Composites Manufacturing, Delft, The Netherlands. (ACM7, 2026)

Scientific posters

- *Gaps and overlaps in AFP composites : Why do they occur?*
  26th Engineering Mechanics Symposium, Papendal, The Netherlands. (2023)
- *Tow lateral movement on AFP compaction rollers : Does it get worse during steering?*
  27th Engineering Mechanics Symposium, Papendal, The Netherlands. (2024)
- *Compensating steered AFP layup paths by predicting tow lateral movement.*
  28th Engineering Mechanics Symposium, Papendal, The Netherlands. (2025)

Dataset

- *Experimental dataset about manufacturing process variations in Automated Fiber Placement composites.* 4TU.ResearchData, CC BY-NC 4.0, (2024).

Curriculum Vitae

Siddharth Pantoji was born in Maharashtra, India. His early interest in aerospace and mechanical engineering developed through building model aircraft, gliders, scalemodel dioramas and a variety of science projects such as hovercrafts, RC boats and electromagnetic launch systems. He completed his primary, secondary and higher secondary education in Pune.

He earned a Bachelor of Engineering in Mechanical Engineering from the Wadia College of Engineering, University of Pune, in 2014, graduating with First Class with Distinction. During his final year, he was recognized as Student of the Year for academic excellence and co-curricular achievement. His senior design project, developed in collaboration with the National Centre for Radio Astrophysics (NCRA-TIFR), was successfully commissioned for the Giant Metrewave Radio Telescope (GMRT).

In 2015, he pursued a Master of Science in Aeronautics and Astronautics at Purdue University, USA. Demonstrating strong performance in composites coursework, he joined Prof. R. Byron Pipes' laboratory - Composites Manufacturing and Simulation Center (CMSC) - as a Graduate Assistant. His research received the Best Research Poster Award at the SPE ACCE Conference.

He also gained valuable industry experience through internships focusing on manufacturing-informed design and simulation of aerospace structures and materials. His projects involved the manufacturing of superalloy aerospace components at Bharat Forge, welding studies on high-strength steel pressure vessels at Walchandnagar Industries, and CAE simulations for aerospace applications at Zeus Numerix.

From 2018 to 2022, he worked as a Product Manager in Research and Development at Hexagon Manufacturing Intelligence, California, where he focused on digital manufacturing technologies and cross-functional product development.

Since 2022, he has been pursuing a Doctor of Philosophy in Aerospace Engineering at Delft University of Technology. His doctoral research at the SAM XL field lab focuses on defects in Automated Fiber Placement (AFP) processes for composite manufacturing, combining experimental studies with various modeling approaches. In 2026, he has continued this work as a postdoctoral researcher in the same research group.

Outside of research, Siddharth actively participates in sports and academic community events. He has won the department badminton competition and was runner-up in a subsequent year. He has hosted and also twice won the annual aerospace trivia event. His personal interests include attending airshows, visiting aviation and military history museums and playing the Santoor.

Automated Fiber Placement (AFP) has become the process of choice for manufacturing large aerospace composites. As the industry moves towards a new era of high-rate production for single-aisle airliners and eVTOLs, AFP must evolve to become more productive and less dependent on post-layup rework and processing. Among the obstacles to this evolution are the inevitable and pervasive gap and overlap defects. Why do they occur? Can their occurrence be predicted or minimized? How do variable stiffness designs affect their formation? And how can AFP technology and process design be optimised using this knowledge? This dissertation addresses these questions through experimental measurements, probabilistic simulations and analytical modelling.

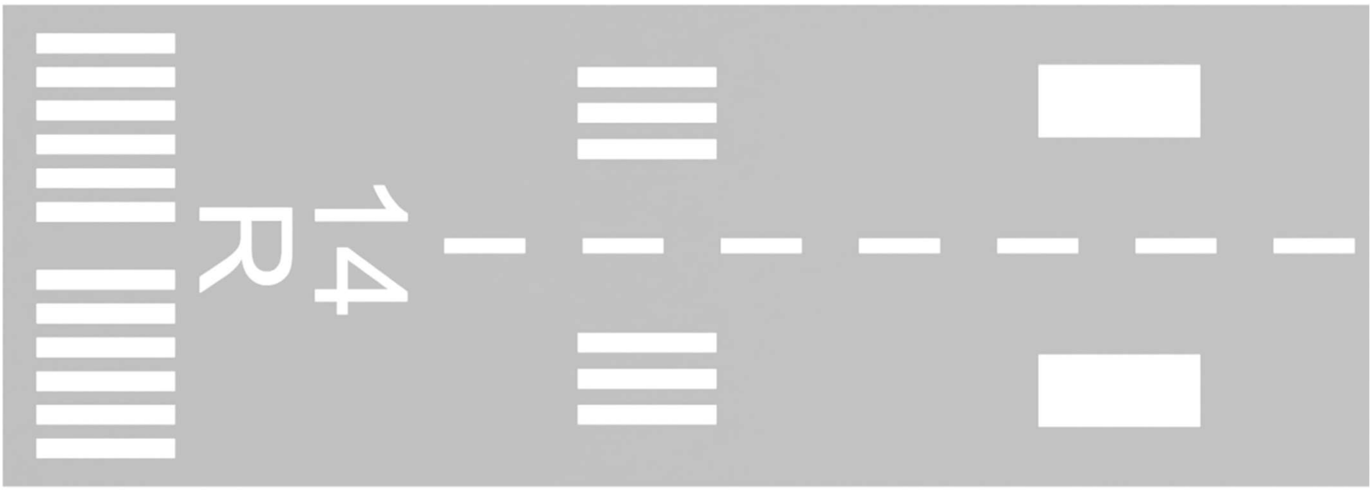

ISBN 978-94-6518-340-4

TU Delft